

INVESTIGATING EFFECTS OF INITIAL GRAIN SIZE DISTRIBUTION ON ROCK WEAR
RATE AND SHAPE CHANGE DUE TO ABRASION

A Thesis submitted to the faculty of
San Francisco State University
In partial fulfillment of
the requirements for
the Degree

Master of Science

In

Geoscience

by

Matthew Jovanny Cardona

San Francisco, California

December 2023

Copyright by
Matthew Jovanny Cardona
2023

Certification of Approval

I certify that I have read Title of Culminating Experience by Matthew Jovanny Cardona, and that in my opinion this work meets the criteria for approving a thesis submitted in partial fulfillment of the requirement for the degree Master of Science in Geosciences at San Francisco State University.

Erin Bray, Ph.D.
Assistant Professor,
Thesis Committee Chair

Kimberly Miller, Ph.D.
Adjunct Faculty

Leonard Sklar Ph.D.
Emeritus

Abstract

This study investigates how varying initial grain size distributions (GSD) of sediment transported along a river change in shape from angular to round and undergo a reduction in size as mass is lost. Two sets of experiments were done in order to examine how rocks change in shape, through the use of a laboratory rock tumbling mill which simulates rock abrasion and attrition in natural river environments, following methods based on previous related studies (Arabina & Sklar, 2016; Sklar et al. 2017). The first, consisted of an unsteady state rock tumbling experiment utilizing limestone rock selected according to 4 different initial grain size distributions and tumbled to a target mass loss of 10 percent. The second, involved conducting a longer unsteady state rock tumbling experiment where a single narrow grain size distribution was selected, with a target mass loss of 6 percent during each tumbling run. In the steady state experiment, the mass that was lost from the initial rocks during each tumbling run was subsequently replaced with the addition of fresh angular rocks before reintroduction to the rock tumbler. This approach was taken in order to see how a rock population in a river is affected by the addition of angular rock grains into a population that is progressively rounding. Methods used during both experimental approaches consisted of a combination of manual physical measurements in conjunction with digital measurements utilizing photo image analysis. For our first approach, results showed that initial grain size distribution has a small influence on the efficiency in which rocks erode, with some GSDs such as the narrow GSD traveling shorter distances to reach 10% mass loss compared to the very narrow GSD. This was also reflected in the variation in wear rate/alpha value range associated with each GSD, further supporting that initial GSD has a small influence in the percent of mass lost per km (1/km). Despite variation in wear rate, all GSDs experienced comparable levels of rounding and final mass allocation over the course of the experiment. Most of the initial mass was retained in the original rocks (over 1 g), followed by fine sediment which reflected most of the mass lost, and small fraction of the mass allocated in fragments (<1g). Fragments produced between each GSD varied indicating that initial grain size distribution may affect how rocks break down. For our steady state experiment, we found that wear rates were highest in the first 5 km of distance traveled, followed by a notable reduction in wear rate as travel distance increased. The highest wear rates were observed during the first few km of distance traveled, followed by a stabilized wear rate at further distance traveled such that the subsequent addition of new grains neither increased or decreased the wear rate, leaving it within the same order of magnitude. An increase in fragment production and circularity was observed for the duration of the experiment. This indicates that, despite the addition of new angular rock grains between each tumbling run, the rounding of grains persisted. Results also showed a steady exponential decline in average diameter as travel distance increased. Mass allocation was similar to the unsteady state experiment in which most of the mass distribution remained in original rock particles greater than 1g, followed by fine sediment, and the smallest fraction to fragments. Our results from our steady state experiment align with previous work showing two phase abrasion and the exponential fining of rock diameter with increased distance traveled. The third component of this study aimed to quantify how variations

in photo image processing affect shape parameter, in particular circularity, by using photo analysis methods in ImageJ and Photoshop that built off of previous studies (Miller et al., 2014). This involved taking high resolution images of our rock grains with the Lidar Camera of the iPhone 12 Pro and transposing them into binary images to extract rock shape parameters using Dr. Brays MATLAB application CobbleApp. Analysis of photo imaging methods shows that the resolution of rock photos will influence the outline of the rock perimeter and the resulting estimates of circularity.

Acknowledgements

First and foremost, I would like to acknowledge my parents for always pushing me and believing in me. I will never be able to repay their ultimate sacrifice of leaving their country and starting a new life here so that my brothers and I would not live what they lived through. I would also like to thank my advisor Dr. Erin Bray for being there through all the ups and downs throughout this process which included a global pandemic and dealing with my crazy schedule which at points included managing three jobs at a time. I would also like to thank my thesis committee for their time and patience throughout this process. As well as their expertise and willingness to meet on what could sometimes be a hectic schedule. I also would like to acknowledge and thank my friends and Outer Sunset community here in SF. You all are my rock. Lastly, I would like to thank and acknowledge all the cooks I shared a hot stove with over the last few years. You treated me like family while mine was so far away, and despite having some of the most complicated life stories and living situations, you would all always have the best attitude and outlook on life.

Table of Contents

List of Figures	xii
List of Appendices	xiv
Chapter 1: Unsteady State Experiment with Limestone	1
1.0 Introduction	1
1.1 Problem Statement	3
1.2 Research Gap	5
1.3 Research Objectives	7
1.4 Significance of Research	8
1.5 Scope and Limitations	10
2.0 Methods:	11
2.1 Unsteady State Experiment Design	11
2.2 Sample Collection and Preliminary Measurements for Experiments	12
2.3 Experimental Procedure	15
2.4 Post Experiment Procedure: Wear Product	18
3.0 Results	19
3.1 Mass Loss Over Travel Distance: Variations Based on Grain Size Distribution	20
3.2 Average Diameter Over Travel Distance	21
3.3 Wear Rate Over Travel Distance	23
3.4 Average Circularity Over Travel Distance	25
3.5 Wear Product: Fine Sediment	27
3.6 Wear Product: Fragmentation	28
3.7 Overall Mass Distribution	29

Discussion	30
Chapter 2: Steady State Experiment	33
1.0 Introduction	33
2.0 Methods: Steady State Experiment Design	35
3.0 Results	37
3.1 Particle Size Distribution Over Travel Distance	37
3.2 Average Diameter Over Cumulative Travel Distance	38
3.3 Alpha Rate Over Cumulative Travel Distance	39
3.4 Average Circularity Over Cumulative Travel Distance	40
3.5 Fragment Production Over Cumulative Travel Distance	41
3.6 Fine Sediment Production Over Cumulative Travel Distance	42
3.7 Overall Mass Distribution	43
4.0 Discussion	43
Chapter 3: Methods in Photo Processing	45
1.0 Introduction	45
Methods	46
2.1 Photo Analysis	46
2.2 Pre-Processing: Photo Grid	47
2.3 Pre-Processing: Photoshop	48
2.4 Pre-Processing: ImageJ	49
2.5 Data Extraction: CobbleApp	50
3.0 Results: Effects of Resolution on Circularity	53
4.0 Discussion	57
References/Bibliography/Works Cited	60

Appendix/Appendices

64

Auxiliary Figures

109

List of Tables

Figure 1. Map of the watershed where samples were collected. The collection point is denoted by the red triangle on map.....	67
Figure 2. Diagram of three different axes (Harrelson et al.,1994).....	68
Figure 3. Tools used in order to measure rock particle mass and axis dimensions.	69
Figure 4. Internal grooves of rock tumbling cylinder.....	70
Figure 5. Rock tumbling machine	71
Figure 6. Unsteady state initial grain size distribution.....	72
Figure 7. Unsteady state experiment mass loss over cumulative travel distance	73
Figure 8. Unsteady state experiment average diameter over cumulative travel distance	74
Figure 9. Unsteady state alpha rate over cumulative travel distance.....	75
Figure 10. Unsteady state experiment median circularity over cumulative travel distance	76
Figure 11. Unsteady state experiment wear product/fine sediment production over cumulative travel distance	77
Figure 12. Unsteady state experiment fragments observed over cumulative travel distance	78
Figure 13. ANOVA and Tukey HSD testing for fragments yields between GSDs	79
Figure 14. Unsteady state experiment final mass allocation for all GSDs	80
Figure 15. Steady state Experiment fraction less than graph representing particle size distribution.....	81
Figure 16. Unsteady steady state experiment average diameter over cumulative travel distance.....	82
Figure 17. Steady state experiment wear rate over travel distance.....	83
Figure 18. Steady state experiment circularity over cumulative travel distance	84
Figure 19. Steady state experiment number of fragments found over cumulative distance traveled	85
Figure 20. Steady state experiment fine sediment production over travel distance.....	86
Figure 21. Steady state experiment final mass allocation.....	87
Figure 22. Photo grid station for photo image analysis	88
Figure 23. Placement and marker for overhead installation of iPhone 12 Pro camera.....	89
Figure 24. Completed photo board with labeled axes and rock grains.....	90
Figure 25. Cropped image with rocks outlined with use of photoshops object detection tool	91
Figure 26. Inverted selection of the object detection tool, showing how everything outside of the rock grain edge is selected preserving edges in future pre processing	92
Figure 27. Use of Adobe Photoshop’s paintbrush tool to remove background from selected rock grains	93
Figure 28. Final high-resolution image exported from Adobe Photoshop.....	94
Figure 29. Snapshot of ImageJ’s edge detection functionality.....	95
Figure 30. Binary image conversion following use of edge detection tool.....	96
Figure 31. Use of the fill holes function. Note how it maintains crisp edges while filling in particles without the use of thresholding	97
Figure 32. Example of an incomplete filled in rock and use of paint tool for correction	98
Figure 33. Finalized 8-bit binary image ready for import into the CobbleApp	99
Figure 34. Example of binary photos to the CobbleApp showing use of centroid labelling system and append function	100
Figure 35. Example of pop-up box for images with less than 48 particles.....	101
Figure 36. Final database following the use of the merge function via CobbleApp.....	102
Figure 37. Comparing mean circularity values of the same photo of raw image. (Left) raw image processed in ImageJ only, (right) raw image preprocessed using photoshop and subsequently imported into ImageJ.	103
Figure 38. Boxplot of average circularity values from five random test images comparing Method 2 at 100% resolution	104

Figure 39. Boxplot of average circularity values from five random test images comparing Method 2 at 75 % resolution	105
Figure 40. Boxplot of average circularity values from all four grain size distributions in the unsteady state experiment using Method 2 at 100% resolution.....	106
Figure 41. ANOVA Test plot including P-value for statistical analysis of differences between photo processing methods	107
Figure 42. Tukey HSD statistical analysis for significant differences in mean circularity across all methods tested.....	108
Figure 43. Unsteady state experiment very narrow GSD.....	110
Figure 44. Unsteady state experiment narrow GSD	111
Figure 45. Unsteady state experiment wide GSD.....	112
Figure 46. Unsteady state very wide GSD	113
Figure 47. Steady state experiment inverse observed between circularity and alpha values with distance traveled.....	114

List of Figures

Figure 1. Map of the watershed where samples were collected. The collection point is denoted by the red triangle on map.	67
Figure 2. Diagram of three different axes (Harrelson et al.,1994).	68
Figure 3. Tools used in order to measure rock particle mass and axis dimensions.	69
Figure 4. Internal grooves of rock tumbling cylinder	70
Figure 5. Rock tumbling machine	71
Figure 6. Unsteady state initial grain size distribution	72
Figure 7. Unsteady state experiment mass loss over cumulative travel distance	73
Figure 8. Unsteady state experiment average diameter over cumulative travel distance	74
Figure 9. Unsteady state alpha rate over cumulative travel distance	75
Figure 10. Unsteady state experiment median circularity over cumulative travel distance	76
Figure 11. Unsteady state experiment wear product/fine sediment production over cumulative travel distance	77
Figure 12. Unsteady state experiment fragments observed over cumulative travel distance	78
Figure 13. ANOVA and Tukey HSD testing for fragments yields between GSDs	79
Figure 14. Unsteady state experiment final mass allocation for all GSDs	80
Figure 15. Steady state Experiment fraction less than graph representing particle size distribution	81
Figure 16. Unsteady steady state experiment average diameter over cumulative travel distance	82
Figure 17. Steady state experiment wear rate over travel distance	83
Figure 18. Steady state Experiment Circularity over cumulative travel distance	84
Figure 19. Steady state Experiment number of fragments found over cumulative distance traveled	85
Figure 20. Steady state Experiment fine sediment production over travel distance	86
Figure 21. Steady state experiment final mass allocation	87
Figure 22. Photo grid station for photo image analysis	88
Figure 23. Placement and marker for overhead installation of iPhone 12 Pro camera	89
Figure 24. Completed photo board with labeled axes and rock grains	90
Figure 25. Cropped image with rocks outlined with use of photoshops object detection tool	91
Figure 26. Inverted selection of the object detection tool, showing how everything outside of the rock grain edge is selected preserving edges in future pre processing	92
Figure 27. Use of Adobe Photoshop's paintbrush tool to remove background from selected rock grains	93
Figure 28. Final high-resolution image exported from Adobe Photoshop	94
Figure 29. Snapshot of ImageJ's edge detection functionality	95
Figure 30. Binary image conversion following use of edge detection tool	96
Figure 31. Use of the fill holes function. Note how it maintains crisp edges while filling in particles without the use of thresholding	97
Figure 32. Example of an incomplete filled in rock and use of paint tool for correction	98
Figure 33. Finalized 8-bit binary image ready for import into the CobbleApp	99
Figure 34. Example of binary photos to the CobbleApp showing use of centroid labelling system and append function	100
Figure 35. Example of pop-up box for images with less than 48 particles	101
Figure 36. Final database following the use of the merge function via CobbleApp	102
Figure 37. Comparing mean circularity values of the same photo of raw image. (Left) raw image processed in ImageJ only, (right) raw image preprocessed using photoshop and subsequently imported into ImageJ.	103
Figure 38. Boxplot of average circularity values from five random test images comparing Method 2 at 100% resolution	104
Figure 39. Boxplot of average circularity values from five random test images comparing Method 2 at 75 % resolution	105

Figure 40. Boxplot of average circularity values from all four grain size distributions in the unsteady state experiment using Method 2 at 100% resolution	106
Figure 41. ANOVA Test plot including P-value for statistical analysis of differences between photo processing methods	107
Figure 42. Tukey HSD statistical analysis for significant differences in mean circularity across all methods tested	108
Figure 43. Unsteady state experiment very narrow GSD	110
Figure 44. Unsteady state experiment narrow GSD	111
Figure 45. Unsteady state experiment wide GSD	112
Figure 46. Unsteady state very wide GSD	113
Figure 47. Steady state experiment inverse observed between circularity and alpha values with distance traveled	114

List of Appendices

Appendix A: List of California State University Campuses	64
Appendix B: Abbreviations of California State University Campuses	65

Chapter 1: Unsteady State Experiment with Limestone

1.0 Introduction

River sediment transport is important in the dynamic process of the morphology of landscapes. As rivers flow through the watershed, they carry sediment further downstream. Erosion from the landscape in steeper upstream regions supply sediment to the river channel alongstream, while downstream reaches tend to exhibit deposition of these transported particles as the channel slope decreases (Parker, 1991; Warrick, 2020). This supply and transport of sediment plays a transformative role in shaping riverbeds, floodplains, and adjacent terrains (Kondolf et al., 2002). The varying grain sizes and lithology of transported particles facilitate formation of habitats (Mason,2019; Kondolf and Wolman,1993). Furthermore, sediment dynamics influence the hydrological characteristics of river systems, dictating flow patterns, channel morphology, and water quality. This sediment transport – and changes in sediment size and shape as rocks wear down – underpins the suitability of riverine environments for specific species such as caddisflies (Mason et al., 2019) and deposition of smaller rounded gravel and sand sets the stage for the establishment and persistence of ecological communities (Wolman, 1993). Rivers also supply sediment to riparian areas that support a myriad of species and support vegetation (Hupp & Osterkamp, 1996).

The volume of sediment within rivers is also a critical factor that governs the incision of bedrock and exerts a profound influence on landscape evolution (Dietrich, 2001; Kondolf et al., 2002; Whipple & Tucker, 2002) Additionally, sediment concentration in rivers has far-reaching effects on various river parameters, including heat flux, albedo, and turbidity (McMahon &

Moore, 2017). Together these factors have significant implications for the habitat suitability of fish and the efficient transport of essential nutrients (McMahon and Moore, 2017; Tyrell, 2015).

Over the past century, geologists have consistently observed a notable phenomenon in river systems. This observation is the progressive reduction in rock size as rocks traverse from the headwaters to the river mouth, primarily due to erosive forces. However, despite this well-established trend, a significant knowledge gap remains concerning the influence of initial sediment grain size distribution on the rate of rocks wearing down due to attrition and abrasion. The term abrasion describes the process of rock being eroded away due to friction, whereas the term attrition refers to energetic collisions due from sediment transport during river transport (Litwin Miller & Jerolmack, 2021). As rock particles are subjected to abrasion they slowly start to change shape as their protruding areas are worn away (Domokos et al., 2014). This change in shape can be measured by the isoperimetric ratio (IR), also referred to as circularity (Miller et al., 2014). Rocks are observed to fine downstream, slowly reducing in diameter the longer they travel. This is described in Sternberg's law (1875):

$$D(x) = D_0 e^{-\gamma x}$$

Where D represents the rocks grains diameter also known as the b-axis following travelled distance while x represents distance downstream. D_0 represents the initial grain diameter and γ represents the wear rate also known as the alpha rate. The alpha term is measured in percent mass lost per kilometer or (1/km) and describes the mass lost from a particle or batch of particles. An assessment of changes in rock circularity as they travel along the length of a river can be used an indirect indicator of the distance traveled from its original source holds the potential to provide insights into the historical aspects of both contemporary and ancient

streambeds (Szabo et al., 2015). An improved understanding of rock shape change over distance traveled becomes especially intriguing with the discovery of rounded rocks by the Curiosity rover on Mars, resembling river rocks and suggesting the presence of ancient streambeds (Szabo et al., 2015).

1.1 Problem Statement

The resulting round rocks that are generated by abrasion, and the byproduct of abrasion in the form of both fragments and finer silt, has both positive and negative implications for natural river systems. On the one hand, the deposition of smaller grains, particularly at the mouth or delta of rivers, plays a critical role in the preservation and health of beaches. These finer sediment particles contribute to the replenishment of sand and mitigate issues related to sand starvation (Dingle et al., 2021; Warrick, 2020). On the other hand, it is important to note that an excessive abundance of small and fine sediment grains generated through these same attrition and abrasion processes can lead to detrimental effects on fish habitats via turbidity which reduces water clarity, inhibiting visual predation, and interfering with photosynthesis leading to lower food availability (Cohen et al., 1993; McMahon & Moore, 2017). When the production of fine sediment surpasses the capacity of the ecosystem to handle and assimilate it, there are negative consequences. An additional example of this can be seen in the macroinvertebrate community in mountain streams (Bylak & Kukuła, 2022).

Moreover, the accumulation of excessive fine sediment can contribute to increased turbidity in water bodies. This turbidity, characterized by reduced water clarity, obstructs the penetration of light, and impedes photosynthesis. Consequently, the growth of submerged

aquatic vegetation may be hampered, resulting in decreased primary productivity and diminished habitat complexity for a wide range of organisms (McMahon & Moore, 2017). Reduced vegetation cover can lead to anoxic conditions, further exacerbating the negative impacts on stream organisms vital to the ecological balance and health of the ecosystem. Therefore, while the natural deposition of smaller sediment grains can be beneficial in certain contexts, careful consideration and management of sediment loads are crucial to avoid the overproduction of finer sediment and the subsequent adverse effects on fish habitats, biodiversity, and overall ecosystem functioning.

This situation is particularly relevant today for salmonoids, given the alteration of natural river morphology and sediment distribution caused by dam construction. Dams block the normal distribution of sediment traveling from the headwaters of a watershed to the river mouth/delta downstream. Sediment trapped behind the dam wall sinks to the bottom leaving only the suspended sediment within the water column. When dams release water downstream, only the fine particles make their way past the dam wall in concentrated amounts, contributing to the clogging of salmon spawning riffles, increasing turbidity, reducing photosynthesis, and increased likelihood of impacts to water quality due to excess fine sediment in the water column. Not only does this affect water quality, but it also affects the morphology of the river downstream of the dam. Water with high amounts of fine suspended sediment is referred to as “hungry water” which lives up to its name as it eats away at riverbanks and causes increased channel incision due to increased streamflow without enough supplied sediment (Kondolf, 1997).

1.2 Research Gap

Laboratory rock tumblers have been used in the past to recreate rock wear induced in fluvial river environments with an aim to understand particle wear in the natural world. Arabnia & Sklar (2016) conducted laboratory-based experiments using three rotating drums with varying diameters that ranged from 0.2 m to 4.0 meters. These drums, similar to the drum that was used in this experiment, were engineered to simulate attrition and abrasion experienced in a fluvial environment where they observed the effect of travel distance along a river with particle size distribution, mass loss rates, and fragmentation (Arabnia & Sklar, 2016). Their experiments consisted of well-sorted angular coarse particles which were taken out and analyzed after every 0.25 km of travel distance. The authors showed that the creation of fragments and fine particle sediment were influenced by the rate of energy expenditure per unit area, or what can also be described as the rotational speed of the rock tumbling drum. They used this to estimate the particle wear rates in a field site located in Inyo Creek, CA. Results showed that particle size distributions became finer over the increased cumulative travel distance through attrition and abrasion within the rock tumbler, resulting in fragments and fine sediment as wear product. These results also varied based on the diameter of their rock-tumbling drums, with the larger drums resulting in increased fragmentation (Arabina & Sklar, 2016). However, authors explained that more complex particle wear models with varying grain size distributions were needed to account for factors such as angularity, and fine sediment in the water columns' influence on abrasion.

Earlier investigations on the process of rock shape change involved the experimental setup of placing limestone blocks within a rotating flume machine to simulate transport-induced

abrasion (Domokos et al., 2014). The study was conducted in multiple intervals, during which the blocks were systematically photographed. These photographs, correlated with the distance traveled, were used to characterize how rocks changed shape from transport-induced abrasion. The combination of these experiments, along with numerical modeling, enabled the researchers to quantitatively analyze how change in shape from angular to round (Domokos et al., 2014). The authors showed that the process of rock rounding occurs in two distinct phases. In the initial phase, “Phase 1”, the protruding areas of the rock undergo gradual wear due to the abrasive forces encountered during transportation. Remarkably, this attrition process leads to a reduction in overall mass of rock clasts without accompanying changes in diameter until it attains complete roundness (Domokos et al., 2014). Subsequently, in the second phase, “Phase 2”, the rounded rock diameter decreases, resulting in a shift towards a more oblong shape/circular shape where axis ratio approaches 1. The observation of this notable decrease in diameter signifies a significant alteration in the rock shape, further contributing to its overall evolution (Domokos et al., 2014). By employing a combination of experimental and quantitative approaches, Domokos et al. (2014) provided comprehensive insights into the step-by-step process of rock rounding and shape evolution, specifically in the context of river transport-induced abrasion. Subsequent experiments were done to observe two phase abrasion in the natural environment by measuring rocks in the field with both physical and digital measurements (Miller et al., 2014). Their use of photo image analysis in conjunction with physical measurements provided evidence that two phase abrasion does occur in natural settings with abrasion controlling overall mass loss and sorting influencing decrease in diameter (Miller et al., 2014). While the mentioned previous experiments utilized photo processing methods to investigate changes in rock shape in a natural

setting, a controlled laboratory experiment specifically examining wear rate and rock shape change has not yet been done using varying initial grain size distributions coupled with photo image analysis. There is currently a gap in research regarding how initial grain size distribution affects wear rates, and whether or not sediment interactions during transport have an impact on abrasion factors.

1.3 Research Objectives

The objective of our research is to investigate the specific impact of the initial sediment grain size distribution on the rate at which riverbed rocks (1) wear down and (2) undergo the transition from angular to round shapes, primarily as a result of particle attrition and abrasion in both a steady-state and an unsteady-state laboratory rock tumbling experiment. Furthermore, we aim to measure the wear rate of sediment during transport while also tracking how the original mass of rocks changes – with some mass breaking off as fragments and other mass being worn off as very fine sediment. The research question we aim to answer is: *How do variations in the initial grain size distribution of rocks supplied to channels influence the wear rate and shape changes as sediments tumble downstream?*

To answer this question, we use a combination of laboratory rock tumbling and photo image analysis to quantify the changes in rock mass, size, and shape that occur due to river transport. In Chapter 1, we present an unsteady state experiment, where 4 different rock batches of varying grain size distributions are worn until they lose 10% of their total mass. In Chapter 2, we present a steady state experiment, where one batch of rocks are introduced into the tumbling mill and the amount of mass lost during each tumble is replaced, keeping a steady total mass for

the duration of the experiment. The results of these experiments hope to improve our understanding of the role of grain size distribution on rock wear rates in river channels, while simultaneously providing insights into the ways that rocks change shape as they are transported to a given distance downstream. In addition to examining whether wear rate is influenced by initial grain size distribution, we also measure where the lost mass goes to from our initial batch of limestone rocks and subsequent mass distribution to smaller rocks generated from collisions, fragments generated from the original particles, and finer silt.

Through laboratory observations and analysis, we aim to observe the allocation of mass in the form of fragments and fine sediment as well as the mass and shape changes to rock grains that occur as a result of sediment transport. Analysis of our laboratory measurements can contribute to a deeper understanding of how rocks wear down.

1.4 Significance of Research

Understanding rock shape change requires tracing their journey from the moment they enter a river to their eventual downstream destination such as a delta or beach. One way to do this is by using talus slopes as a control for the initial grain size of rock particles supplied to river channels, as fracture spaces observed on the cliff face tend to mirror the size distribution of the material collected in the talus slopes beneath (Verdian et al., 2021). Thus, the talus slopes provide a useful reference point for studying the grain size distribution of rocks and their change in shape over time.

Rocks commonly make their way into the river channel either through gravity-driven movement from the adjacent talus slopes or by being picked up by a current with enough energy

to move rock grains into the river. Once they enter the river system, they undergo constant tumbling along the riverbed causing frequent collisions with other rocks and the riverbed. These collisions result in fragmentation from impact with the bed floor and other rock grains. As a consequence of collisions, rocks begin to lose their protruding areas, mass, and overall angularity as defined elsewhere in the literature (Litwin Miller & Jerolmack, 2021).

The process of rock shape change in rivers is a complex phenomenon influenced by multiple factors. Previous studies have shown that water velocity is one factor that determines the intensity of rock collisions and the extent of fragmentation, however it is important to note that this is weakly dependent on particle size (Attal & Lavé, 2009). Increased flow velocities typically facilitate higher energy dissipation during collisions, resulting in enhanced rock fragmentation and can lead towards accelerated loss in angularity and increase in circularity (Attal & Lavé, 2009; Bodek & Jerolmack, 2021; Litwin Miller & Jerolmack, 2021).

Additionally, the availability of sediment supply in the river system can influence the shape evolution of rocks. A higher sediment load can enhance the frequency of collisions between rocks, promoting more rapid changes in shape. Conversely, a lower sediment supply may result in reduced collisions and slower shape evolution (Attal & Lavé, 2009). Lithology is also a control on how rocks change in shape over time as well as the rate at which they wear (Attal & Lavé, 2009). Lithology plays a large role in tensile strength of rock particles which leads to variation in particle breakdown when exposed to the same experimental conditions (Attal & Lavé, 2009). The roughness of a riverbed also influences the rate at which rocks wear. Bed roughness can increase or decrease the abrasiveness to other rocks and during impact with the riverbed (Attal & Lavé, 2009). These spatial variations in riverbed roughness in conjunction with

flow rates, sediment supply, and lithology can lead to a diverse array of spatially distributed shapes and wear rates. By trying to recreate rock shape change induced by rivers in a laboratory setting in conjunction with photo image analysis we hope to get a snapshot of rock shape change in a controlled environment and how initial grain size distribution overlaps with these controls on abrasion.

1.5 Scope and Limitations

This study aims to quantify wear rates of rocks along the length of rivers, their wear rate and mass allocation via attrition and abrasion, and changes in overall shape as a batch of rocks transition from angular to round. This study is limited in scope in a few different realms. First, this study uses a single type of lithology, limestone, and does not consider how wear rates may be influenced by a variety of rock types. Second, our study uses a constant velocity for all experiments, rather than considering a range of velocities observed along the length of rivers. Third, our study analyzes rocks as a batch, and quantifies changes in rock characteristics (i.e., mass, shape, roundness) for the whole batch rather than by tracking each individual rock clast from one tumbling run to the next. We are unable to fully track each individual rock over the course of the experiment, at least for the moment, and as a result our analysis is focused on changes to the batch of rocks as a whole, rather than individual particles. Analysis in this study relies on summary statistical batch data and photo image analysis. Although this research represents progress compared to previous studies, it is still limited in its ability to comprehensively track individual rock grains throughout the entire duration of the experiment.

2.0 Methods:

2.1 Unsteady State Experiment Design

We conducted a series of laboratory experiments in which four different batches of rocks were tumbled in a laboratory rock tumbler until the total mass of the batch of rocks achieved a target of 10% mass lost. Our aim of the 4 different experiments is to understand how the initial grain size distribution of rocks influences the wear rate at which particle mass is lost and to understand how different initial grain size distributions influence various shape parameters: circularity/isoperimetric ratio, diameter, and the extent of fragmentation arising from attrition and abrasion. In this study, we used limestone sampled from a quarry located in the North Fork American River watershed. The limestone particles collected for this experiment were separated into four batches of rocks each with distinct grain size distributions as seen in **Figure 6** and **Table 1**: (1) a very narrow grain size distribution (GSD), (2) a narrow GSD, (3) a wide GSD, and a very wide GSD. While all experiments used a constant starting mass of 1850g and were tumbled repeatedly until achieving a target of 10% mass lost, they each exhibited distinct quantities of particles, mass ranges, and average masses. These experiments were then subjected to identical rotational velocities within a laboratory rock tumbler, measured in rotations per minute (RPM), for a total of 5-7 tumbling runs across the 4 different experiments, until an overall mass reduction of 10% was achieved. Through this approach, we aimed to discern how varying initial grain size distributions might influence wear rate, wear product, circularity, diameter, and the distribution of mass.

Our initial analysis of the results of our tumbling experiments are focused on the mass lost, or wear rate per unit distance traveled. Simultaneously, we quantify changes in circularity of the worn particles, a shape parameter calculated from image analysis, offering insights into the alterations in shape experienced by the limestone particles during abrasion. By comparing the circularity of the initial limestone particles with that of the worn particles, we aim to quantify the degree of rounding induced by abrasion, with an eye toward uncovering any discernible trends linked to initial grain size distribution.

Further, we also investigate the total mass of wear product generated during each laboratory experiments, which consists of both rock fragments that are less than 1g, and fine sediment or silt that is suspended in the water of the laboratory tumbler after each tumbling run.

Lastly, we turn our attention to the grain size diameter of rocks before, during, and after reaching 10 percent mass lost, a critical parameter signifying the relationship between travel distance and the overall shape alteration observed in our sample particles. This metric provides valuable insights into the evolving shape characteristics influenced by abrasion and grain size distribution according to two phase abrasion theory (Domokos et al., 2014).

2.2 Sample Collection and Preliminary Measurements for Experiments

The experiment utilized limestone rock samples obtained from a nearby rock quarry situated adjacent to the North Fork American River in Cool, CA (**Figure 1**). Dr. Erin Bray and Dr. Sklar personally collected the rocks, which were then transported to San Francisco State University. The rock samples selected for use in the experiment were then categorized into four subgroups based on their respective rock mass ranges.

Following the mass-based sorting process into 4 distinct batches, rocks were soaked in water by immersion, replicating the conditions experienced by river rocks during their transportation in a fluvial environment. To achieve this, the rocks were collectively weighed and then placed in water-filled buckets for soaking. Throughout a span of several hours, the rocks were periodically removed from the buckets and weighed multiple times to verify saturation. Saturation was determined by ensuring that the rocks no longer exhibited an increase in mass after the soaking period.

Following the confirmation that rocks had reached saturation, rock particles were sorted into four distinct batches of rocks according to different grain size distributions (GSD) for our unsteady-state experiment. The design of these grain size distributions was the result of the expertise of committee member Dr. Leonard Sklar. The four GSDs were categorized based on their mass spread, namely: very narrow GSD, narrow GSD, wide GSD, and very wide GSD. Although each GSD possessed varying clast quantities, average mass, and distribution characteristics, they all share an identical initial batch mass of 1850g (**Table 1**). This design allowed us to examine how these initial GSDs would respond differently to a total mass reduction of 10% across several iterative tumbling runs. This experiment design of overall 10% mass reduction was broken down into target runs of about 3% mass lost for every tumble run. This was done in order to track the small changes in rock shape throughout the course of the experiment. While our target was a 3% mass loss per tumble run, most experiments took an about 4 to 6 tumble runs to reach the 10% mass loss threshold.

To accurately track the evolving characteristics of our rock particles over the course of these experiments, it was imperative to measure each individual rock within their respective grain size distributions (GSD) before introducing them into the rock tumbler, and after each tumbling run. To ensure methodological consistency, we employed established techniques documented in relevant scientific literature, which we extensively consulted and adopted for our study (Domokos et al., 2014; Szabó et al., 2013). These methods involved precise measurements of the mass of each rock in grams (g), as well as the measurements of their A, B, and C axes' in (mm) through the use of a digital caliper (**Figure 2 & Figure 3**). The number of equilibrium points for each rock were also recorded. Equilibrium points are the number of planes a rock particle has that can support its full weight on a level surface. These established procedures ensured the collection of comprehensive and robust data, facilitating a thorough examination of the physical properties of the rock particles throughout the study.

In addition to employing established techniques, we undertook a novel approach by refining our own methodology, which entails utilizing advanced photo image analysis of rock grains prior to their introduction into the rock tumbler. This initial set of physical and digital data is collectively referred to as the "Pre-Tumble" dataset (PT) which was used for a base reference to compare with subsequent observations (**Figure 24**).

Determining the optimal tumbling mill runtime is the final step prior to the experiment. Our target, for the purposes of this experiment, was a mass loss of 3% per tumble run until an overall mass loss of 10% was reached. To accomplish this, we employed the Design Calculator developed by Dr. Leonard Sklar, which has been utilized in previous studies. This tool allowed us to input key variables, including the initial batch mass, desired percentage loss, and an

estimated alpha rate. Using these inputs, the calculator generated a precise runtime estimation for each specific tumble run.

2.3 Experimental Procedure

Experiments took place in San Francisco State University's Earth and Climate Sciences Rock Lab and in the Bray Rivers Lab. Each of the four experiments were conducted individually, focusing on a complete grain size distribution. The rock tumbling mill, featuring a diameter of 0.22 meters, served as the containment vessel for the samples and medium for rotating fluvial transport simulation (**Figure 4**). The rock tumbler was engineered to best simulate rock wear by using the internal grooves within the tumbler to create a shear layer when rotated. To maintain consistency throughout all experiments, the tumbler was consistently filled with fresh water, leaving a one-inch gap between the water level and the rim. The rock tumbling mill was sealed by placing a rubber gasket against the rim, followed by a metal lid using screws and brackets to apply a secure compressional seal. Subsequently, the rock-tumbling steel cylinder was carefully positioned onto the rotating device which is powered by gears that were turned via chain and motor. The rotational speed of the cylinder was then calibrated using the attached speed control device to achieve a rotational speed of 15 rotations per minute/(RPM) (**Figure 5**). The tumble was initiated and terminated manually for the duration of the estimated runtime.

Following each tumbling run, the cylindrical rock tumbler was moved from the rotational device and set aside while the extraction process was prepared. The extraction procedure involved using a cleaned 5-gallon bucket with a steel sieve placed above it while pouring out the

tumbling mill over the sieve, designed to exclusively permit the passage of fine sediment. To maintain the optimal condition of the rock grains, those collected on the sieve were then stored in a separate bucket, ensuring their continued saturation with the addition of fresh water. Both the wear product and the rock samples were labeled with pertinent information, including the corresponding grain size distribution (GSD), the run number, the date of the experiment, and the initials of the operator.

Rocks and wear products were physically measured by hand, photographed, and returned to the soaking tumbler for subsequent tumble runs, iteratively until reaching the target 10% mass lost. To ensure accurate data, the rocks were maintained in a soaking bath to retain their saturation during the time between photographs and hand measurements. Subsequently, each rock was taken out individually from the bath to facilitate measurement.

Prior to the measurements, the rocks were gently patted with a towel to eliminate any excess water that could interfere with mass measurements which were taken with a lab scale. In addition to mass (g), the rocks were measured along their A, B, and C axes in mm with the use of a caliper as pictured in **Figure 3**, and examined for equilibrium points. Methods and units for each rock particle measurements are described below:

Manual measurements:

- **Mass:** Measured in grams using a laboratory scale (g)
- **A,B,C Axis:** Measured in millimeters using a digital caliper (mm)
- **Equilibrium points:** Physical measurements counting the number of planes a rock can hold its weight on (unitless)

- **Rock count:** Was recorded by manually counting rock grains over 1 g as well as taking photo images for a digital record (unitless)
- **Fragment count:** Was recorded by manually counting rock grains under 1 g (unitless)

Digital Measurements using Dr. Brays Cobble App

- **Isoperimetric Ratio/Circularity:** A unitless metric - $4\pi A/P$
- **Area:** Measured in pixels via photo image analysis (px)
 - *Actual number of pixels in the region, returned as a scalar. This value might differ slightly from the value returned by `bwarea`, which weights different patterns of pixels differently.*
- **Major axis length:** Measured in pixels via photo image analysis (px)
 - *Length (in pixels) of the major axis of the ellipse that has the same normalized second central moments as the region, returned as a scalar.*
- **Minor axis length:** Measured in pixels via photo image analysis (px)
 - *Length (in pixels) of the minor axis of the ellipse that has the same normalized second central moments as the region, returned as a scalar.*
- **Eccentricity:** Measured in pixels via photo image analysis (px) –
 - *Eccentricity of the ellipse that has the same second-moments as the region, returned as a scalar. The eccentricity is the ratio of the distance between the foci of the ellipse and its major axis length. The value is between 0 and 1. (0 and 1 are degenerate cases. An ellipse whose eccentricity is 0 is actually a circle, while an ellipse whose eccentricity is 1 is a line segment.)*
- **Perimeter:** Measured in pixels via photo image analysis (px)

- **Alpha rate:** % mass lost per km (1/km)
- **Pixel to mm ratio:** Measured in Image J with use of scale bar (px/mm)

To streamline the data organization and analysis process, each rock was allocated to an individual cell within a photo grid. This arrangement allowed for the systematic association of each rock's physical measurement data with its respective locations in the photo grid (**Figure 24**). An overhead photo of rocks A-1 through H-6 was taken including a ruler for scale for pixel-to-mm analysis. This photo was then processed through Adobe Photoshop, ImageJ, and uploaded to the Cobble App for photo image analysis. A more detailed account of this process is included in Chapter 3 of this paper.

2.4 Post Experiment Procedure: Wear Product

Following the rock tumbling process, the contents of the rock tumbling cylinder were poured over a sieve which would collect the rock particles and rock fragments while allowing fine suspended sediment to be collected in a clean 5 gallon bucket situated below the sieve. Fragments and rock particles were then moved into a separate clean bucket and filled with fresh water to keep saturation during transport, the measurement process, and up until being reintroduced into the rock tumbler for the subsequent experiment. Once the fine sediment had visibly settled in the 5 gallon bucket, the upper layer of water was meticulously decanted to prevent any loss of settled sediment. The remaining sediment was gently mixed with any residual water and transferred into a numbered laboratory glass vessel or cylinder. Following this step, the wear product underwent a drying process within an isotemp oven, alongside other samples

within the same category at a controlled temperature of 105°C. This step aimed to facilitate the evaporation of all moisture, leaving behind only the fine sediment for precise measurement of the dry fine sediment weight. This thermal treatment typically spanned a duration of five days, during which samples were periodically monitored. Upon completion of the drying process, the glass vessel containing the sediment was allowed to cool before extraction from the isotherm oven. The sediment was promptly weighed using a laboratory scale, and this mass was then subtracted from the known weight of the numbered laboratory glass vessel or cylinder. Dried sediment was then scraped the out of glass cylinder and saved into a labeled glass sample jar labeled with the amount of mass recorded as well as the tumble run from which it was sourced.

3.0 Results

In this section, we present the outcomes of our unsteady-state experiment investigating the effects of grain size distributions on various parameters related to rock abrasion and shape evolution. The experiment was designed to simulate fluvial transport-induced abrasion, allowing us to track the evolving characteristics of limestone rock particles across different grain size distributions (GSDs). Each GSD was categorized based on its mass spread, ranging from very narrow to very wide, while maintaining a constant total batch mass of 1850 g (**Table 1**). Despite the same initial mass, each GSD was composed of a varying amount of rocks and average grain size. Our methodology integrated established techniques, incorporating photo image analysis of rock grains before introduction into the rock tumbler. This "Pre-Tumble" photo and dataset extracted via photo image analysis served as a base reference for future observations (**Figure 24**).

3.1 Mass Loss Over Travel Distance: Variations Based on Grain Size Distribution

Figure 7, illustrates the mass lost across travel distance for each grain size distribution. Each line in **Figure 7** represents one of the four experiments in the unsteady state experiment. Each of these lines are colored to represent a specific grain size distribution; this color will remain consistent across figures for this chapter. The green line represents the narrow GSD, the blue line represents the very narrow GSD, followed by the orange line which represents the wide GSD, and finally the red line which represents the very wide GSD. Each data point along the plot lines represents measurements obtained following each tumble run. While all four distributions exhibit anticipated trends in mass loss, subtle variations emerge in the amount of distance traveled to reach the 10% mass loss threshold.

As seen in **Figure 7**, the narrow GSD (green line) achieved the 10 % mass lost within a cumulative distance of 4.17 km, making it the quickest GSD out of all four experiments to reach 10% mass loss. The wide GSD (orange) traveled a cumulative distance of 4.66 km to reach the 10% threshold making it the second fastest eroding GSD. The very wide GSD (red) traveled a cumulative distance of 4.94 km. The very narrow GSD (blue) traveled a cumulative distance of 5.59 km. These longer cumulative distances for the very wide GSD and very narrow GSD mark them as the slowest GSD to reach 10% mass loss.

When comparing the narrow and very narrow GSDs, we see that the very narrow GSD had a lower mass loss per km compared to the narrow GSD. This indicates that the very narrow GSD was slower to reach 10% mass loss, represented by its further travel distance of 5.59 km compared to the narrow GSD which managed to reach 10% mass loss at a shorter distance of 4.17 km. This implies that the very narrow GSD, with its finer and more concentrated grain size

distribution, demonstrated greater resistance to abrasion, requiring a more prolonged transport distance to incur the same level of mass loss as the less conservative narrow GSD.

Both the wide GSD and very wide GSD experiments exhibit relatively similar cumulative travel distances to reach 10% mass loss of approximately 4.66 km and 4.94 km, respectively. It is important to note that the very wide GSD exceeded its 10% target mass lost by 0.29% which resulted in a higher overall travel distance. Overall, all unsteady state experiments achieved the target 10% mass loss within 4-6 km of distance traveled. Cumulative mass loss along distance is summarized in **Table 3** through **Table 6**.

3.2 Average Diameter Over Travel Distance

Changes in particle diameter over a cumulative travel distance for each of the four distinct grain size distributions (GSDs) is shown in **Figure 8**. **Figure 8** provides a comprehensive view of the change in average diameter for all four GSDs as they undergo abrasion over the course of our experiment. The initial data points, positioned directly over the x axis, signifies the initial average diameter for all four GSDs. The initial average diameter was similar between the very narrow and narrow distributions starting at just below 26.0 mm marking the narrow and very narrow GSDs the two experiments with the highest initial average diameter. Initial average diameters between the wide and very wide distributions were also fairly similar. The wide GSD had an initial average diameter of 21.55 mm. The very wide GSD had an initial average diameter of 20.85 mm.

Both the narrow and very narrow GSD had an initial identical average diameters of 25.3 mm. However, subtle variations emerged as the tumbling experiment progressed. The narrow

GSD exhibited an average reduction in diameter of 2.14 mm. The very narrow GSD experienced an average reduction in diameter of 1.68 mm. For the wide GSD the average reduction in diameter was that of 0.45 mm and the very wide GSD had an average reduction in diameter of 2.05 mm. Overall the largest reduction in average grain size diameter across all GSD is that of the narrow GSD.

From these results, it is clear that the narrow GSD exhibited the most significant reduction in average diameter during its 10% mass reduction compared to all other GSDs. This indicates that the narrow GSD eroded more noticeably than the very narrow, wide, and very wide GSDs, despite the surprising fact that it traveled the shortest distance. This suggests that while the narrow GSD underwent a more noticeable reduction in diameter, it did so more efficiently over a shorter travel distance. In contrast, the very narrow GSD exhibited a slower reduction in diameter, covering a greater distance to achieve its 10% target mass loss. For the wide and very wide GSDs, the wide GSD experienced a more modest average reduction in diameter (0.45 mm) compared to the very wide GSD (2.05 mm). Interestingly, the wide GSD showcased a higher mass loss per kilometer and reached the 10% target mass loss within a shorter distance (4.66 km) compared to the very wide GSD, which covered (4.94 km). This means that the wide GSD exhibited a lower reduction in diameter but reduced its diameter more efficiently over a shorter distance, whereas the very wide GSD, with a more significant diameter reduction, covered a slightly longer distance. However, it is essential to note that the distance traveled for the very wide GSD slightly surpassed the 10% threshold by 0.29%. Despite this discrepancy, the difference between the average reduction in diameter remains on the same order of magnitude.

3.3 Wear Rate Over Travel Distance

In this subsection, we delve into the observations on wear rate, also known as alpha, of our experimental study, which focused on four distinct GSDs: very narrow, narrow, wide, and very wide. By looking at the variations in alpha rates as a function of the percentage mass lost per kilometer, we aim to understand how varying initial GSD affects the rate of percent mass loss over each GSD cumulative travel distance. Alpha rates recorded for each individual tumble run can be found in **Table 3** through **Table 6**.

Figure 9 illustrates the wear rate (1/km) as each GSD achieves its 10% mass lost target. As one can see in **Figure 9**, the alpha rate decreases with increasing cumulative travel distance traveled for all GSDs. This suggests that, as the distance traveled increases, the rate of wear decreases. Upon close examination, the narrow GSD shown by the green line in **Figure 9**, has alpha values that range from 0.0108-0.0302 1/km, indicating a wide spectrum of wear rates that decline as it reaches its 10% mass lost target. The very narrow GSD exhibits a narrower range of alpha values, spanning from 0.0159 to 0.0227 1/km. This suggests a more consistent wear rate observed of the very narrow GSD, with particles experiencing a relatively steady reduction as these particles travel to reach their target 10% mass lost. This is illustrated by the blue line in **Figure 9**. This was observed to be the most steady and uniform decline between all GSDs.

As shown in **Figure 9** the wide GSD represented by the yellow line has alpha values ranging from 0.0166 to 0.0310 1/km. Similar to the narrow GSD, this range demonstrates considerable variability in wear rates over its cumulative travel distance. This is represented by the yellow line in **Figure 9**, where one can see a steady decline of wear rate values for the wide GSD. The very wide GSD displays the widest range of alpha values, extending from (0.0048 to

0.0274 1/km). This distribution exhibits the highest degree of variability in wear rate of any GSD over its distance traveled to reach its 10% mass lost target. This is visualized by the red line in **Figure 9** and is especially apparent in the final two data points/final tumbles of the very wide GSD which showcase both a large decrease in alpha values followed by a large increase during its final tumble run. I would like to note the final spike in % mass loss per km that can be seen by the red line between Run 5 and Run 6 in **Figure 9**. This higher alpha value can be associated with the increased distance traveled of final run that surpassed the 10% batch mass loss target by 0.29% compared to the previous run which resulted in a lower alpha value.

Overall, all four GSD were observed to have decreasing alpha rates as they traveled to reach their 10% mass lost target. However, distinct ranges of alpha values were observed for each GSD over the course of the experiment. The very wide GSD has the highest variability in alpha rates of all GSD, followed by the wide GSD. The narrow and very narrow GSDs were observed to have comparatively narrower ranges in alpha values as they reached their mass lost target, suggesting more consistent wear. The narrow GSD (green line) was also observed to have higher alpha rates within its range compared to the very narrow GSD (blue line), indicating a more efficient reduction in mass per kilometer despite traveling a shorter distance. Similarly, the wide GSD (yellow line) also was observed to have higher alpha rates within its range than the very wide GSD, (red line) suggesting more efficient wear over a shorter distance.

3.4 Average Circularity Over Travel Distance

Change in particles from angular to round can be quantified by the shape parameter “circularity”. In this subsection, changes in circularity over cumulative travel distance as these four distinct grain size distributions (GSDs) reach their 10% mass lost target.

Circularity, a dimensionless metric, quantifies the resemblance of particle shape to that of a perfect circle. As particles undergo abrasion, their edges and protrusions wear away, influencing their circularity values. Values range from 0 to 1 and are calculated by $4\pi A/P^2$. Rocks with a circularity value approaching 1 signify a higher degree of roundness, indicating the reduction or absence of protruding areas. By examining circularity trends within each GSD over distance traveled to reach 10% mass loss, we seek to gain a better understanding of how initial grain size distribution influences the circular evolution of particles.

Figure 10 showcases the average circularity of each GSD over cumulative distance in order to reach their 10% mass loss threshold. **Figure 10** visualizes a common trend of increasing circularity with increased distance traveled across all GSDs. In **Figure 10** each GSD can be seen to have a large initial increase in circularity, followed by a more consistent gradual increase thereafter, this represents the initial erosion of protruding areas in accordance with the first phase of two phase abrasion theory (Domokos, et al .2014).

While most of the GSDs shared this trend of heightened values early in the experiment, the very narrow GSD as noted by the blue line in **Figure 10**, was observed to be an outlier. The very narrow GSD had the largest increase in circularity compared to all other GSDs within the first two tumble runs. This distinction from the other GSD circularity trends suggests that the

very narrow GSD experienced more erosion compared to other GSDs, characterized by a more rapid increase in circularity in the early stages of the experiment. The narrow GSD, as noted by the green line, was observed to have a relatively high degree of roundness, with average circularity values ranging from 0.8261 to 0.9007 over the course of the experiment. While the very narrow GSD was observed to have a lower range of average circularity values compared to the narrow GSD, ranging from 0.7976 to 0.8731. It was also noted that the particles in the very narrow GSD have a slightly more varied population as noted by the range of average circularity values. Particles in the wide GSD, as noted by the yellow line, were observed to have average circularity values ranging from 0.8226 to 0.8892. The wide GSD also exhibits a relatively high degree of roundness, with the average circularity value range similar to that of the narrow GSD (green line). The very wide GSD, as noted by the red line, had circularity values ranging from 0.8073 to 0.8778. This GSD shows a similar degree of roundness to the other GSDs. Overall, the trend in average circularity values across the different GSDs indicates that circularity increases over distance. However, despite all GSDs reaching the same 10% mass target, each GSD showcases a unique range of different average circularity values. This is especially apparent in **Figure 40**, where one can see the varying ranges of circularity between each grain size distribution. While there are variations in circularity ranges for each GSD, these ranges are relatively close and on the same order of magnitude. This indicates that despite varying GSD for each experiment, each GSD experiences comparable levels of rounding over the course of the experiment.

3.5 Wear Product: Fine Sediment

This subsection investigates the production of fine sediment as an outcome of the abrasion and fragmentation processes undergone by rock particles, which we refer to as wear product. The analysis focuses on four distinct grain size distributions: very narrow, narrow, wide, and very wide. A comprehensive examination of wear product accumulation across cumulative travel distances sheds light on how varying grain size distributions influence erosional processes.

Figure 11 visually encapsulates the production of fine sediment for each grain size distribution as they experience abrasion over cumulative travel distances. This plot illustrates how dynamic this process can be and the potential influence of the initial GSD. Overall, each grain size distribution exhibits similar trends, characterized by increases in fine sediment production, followed by a decline in the amount of fine sediment produced as distance increased. Interestingly, both the narrow GSD, noted by the green line, and the very narrow GSD, noted by the blue line, demonstrate a heightened initial production of fine sediment in comparison to the wide GSD (yellow line) and very wide GSD (red line). This indicates that both the narrow GSD and very narrow GSD experienced heightened fine sediment yields in the early stages of the experiment. However, the wide GSD (yellow line) and very wide GSD (red line) were observed to have lower initial increases in fine sediment yields, followed by more increased sediment yields at later stages of wear. Despite slight variation in fine sediment produced over distance traveled, the amount of fine sediment produced from all experiments was seen to be on the same order of magnitude.

3.6 Wear Product: Fragmentation

This subsection investigates fragmentation production resulting from rock tumbling over the course of this experiment. This analysis focuses on our four distinct grain size distributions: very narrow, narrow, wide, and very wide. **Figure 12** shows the amount of fragments found for each GSD over the cumulative distance traveled to reach their 10% mass lost target. **Table 3** through **Table 6** contain the number of fragments found for each run of all four GSDs. For the narrow GSD (green line), we observed the most heightened and consistent fragment production compared to all other GSDs over the course of the experiment.

In the very narrow GSD, as noted by the blue line in **Figure 12**, we observe a sustained increase in fragment production for the duration of the experiment, however the amount of fragments produced by this GSD was observed to generate the lowest fragment yields of all GSDs. For the wide GSD, as noted by the yellow line in **Figure 12**, fragmentation follows a similar trend to the very narrow GSD, steadily producing fragments during the course of the experiment with low overall fragment yields over the course of the experiment. In the very wide GSD, as noted by the red line, we observed a heightened and consistent fragment yield over the course of the experiment. Overall, each GSD demonstrated an overall rise in fragment yields, showing variations in the number of fragments produced as they approached their 10% mass loss target. When performing an ANOVA and Tukey HSD to test the statistical significance between the fragments produced between each GSD, a p-value of 0.00001 was returned signifying that there is a large difference in fragment production based on initial grain size distribution. This was further supported by testing difference in mean fragment production between all GSDs (**Figure 13**).

3.7 Overall Mass Distribution

This subsection investigates the distribution of mass between rocks, fragments, and wear product in the form of fine sediment across four distinct grain size distributions: very narrow, narrow, wide, and very wide. In order to do this, we calculated the combined final mass of the remaining rock particles, the final fragment yield, and amalgamation of dried wear product/fine sediment which was collected for each GSD over the course of the experiment.

Figure 14 showcases the final distribution of mass for all four experiments in the form of a bar graph. The y-axis of this graph is capped at 1850g, which is representative of the starting mass for all four GSDs. This bar graph is a visual representation of the final distribution of mass with the blue section of the bar representing the amount of mass from the remaining rocks in the experiment, the orange section of the bar representing the remaining mass of the remaining fragments, and the grey section of the bar representing the dry weight of wear product/fine sediment. Ideally, the amalgamation of these should equal to 1850g as this experiment is meant to be a closed system. As seen in

Figure 14, fragments make up a very minute fraction of the final allocated mass across all GSDs. When looking at all GSDs, one can see that, despite the variation in initial grain size distribution between all four experiments, all GSDs were observed to have a very similar final allocation of mass after reaching the 10% mass lost target with the only variation in the form of fragment production however this difference can be considered negligible. These observations suggest that, over time and under continuous abrasion, these four distributions to exhibit consistent patterns of mass allocation.

Discussion

The results from these laboratory experiments give us an opportunity to look at our research question of how variations in the initial grain size distribution of rocks supplied to channels influence the wear rate and shape changes as sediments tumble downstream.

The data revealed a variation in initial GSD led to small differences in distance traveled in order to reach their target 10% mass loss. The narrow GSD was observed to erode the most efficiently, achieving 10% mass loss in the shortest cumulative distance. This suggests that a higher number of rocks within a more concentrated population, as represented by the narrow and wide GSDs, loses more mass over shorter distances.

Data related to the influence of initial grain size distribution allowed us to observe slight variations in the reduction of average diameter between all four experiments. The variations in the reduction of average diameter across all GSDs can be attributed to their initial grain size distributions. Some GSDs such as the narrow GSD, contained on average larger particles, resulting in higher reduction in diameter compared to the very narrow GSD, which had a more concentrated distribution of smaller particles. Similarly, the wide and very wide GSDs, despite having very similar low initial average mass for each population, both had variations in reduction of diameter over their cumulative distance traveled. While the reduction of average diameter over distance traveled varied across all four experiments, the extent of reduction in diameter for each GSD as they reached their 10% target mass loss is comparable.

Circularity data from this experiment allowed the quantification of how rocks went from angular to round over the course of this experiment. While initial GSD varied between all four

experiments, all rocks shared a similar trend of increasing circularity with increased travel distance as they reached the target mass loss. Despite slight variations between all GSDs in circularity values, all GSDs experienced comparable levels of rounding.

The influence of initial grain size distribution on wear product in the form of fine sediment and fragmentation provided an interesting insight into what happens to material eroded away from rocks due to attrition and abrasion. Initial GSD seemed to have no real influence on the amount of fine sediment produced across all four experiments, despite variations in amounts of fine sediment yielded at different distances, all GSDs yielded comparable amounts of fine sediment. However initial GSD seems to influence fragment yields as confirmed by the ANOVA and Tukey HSD which confirmed the statistical differences in fragment production across all GSDs. Initial grain size distribution on overall mass allocation did not seem to have an influence across all four experiments. Despite variations in initial GSD, all four experiments held most of their mass within the rock grains themselves, followed by similar yields in fine sediment, and a small fraction of their overall mass lost in the form of fragments.

These findings emphasize that initial grain size distribution must be considered in understanding how rocks change from angular to round as they travel in a river channel. While these experiments did provide valuable insights into how initial GSD affects a variety of factors as rocks experience attrition and abrasion, these rocks did not travel an extended distance. Future unsteady state experiments that go beyond a 10% overall mass lost target may be worth looking into in order to see how initial GSD could possibly play a role in two phase abrasion. Additionally conducting future unsteady-state experiments involving diverse initial grain size distributions and exploring the transformation of different lithologies from angular to round

would offer valuable insights. These experiments could enhance our understanding of particle breakdown processes in river channels, especially in geologically distinct regions

Chapter 2: Steady State Experiment

1.0 Introduction

Differing from the unsteady experiments, which focused on achieving a target mass loss, this chapter introduces a steady-state rock tumbling approach. This approach is done to better recreate what occurs in natural river environments, where rocks are continually introduced into the river from adjacent sources such as talus slopes and tributaries. This experiment mirrors the natural process of particle abrasion over an extended duration, allowing us to observe cumulative effects arising from an evolving steady state grain size distribution. What we aim to answer through this experiment is how steady state conditions affect mass and change in shape over distance travelled, as well as how the addition of fresh angular rocks throughout a single experiment affects wear product yields and mass allocation. Before going further, I would like to delve into what a steady state condition means in the context of rock tumbling. "Steady state" refers to a condition where the system reaches a point of equilibrium or stability. Specifically, in the case of this rock tumbling experiment, it implies that the experiment is designed so that the input (addition of new rocks) and output (mass loss in the form of wear product) are balanced, leading to a constant overall mass within the tumbler.

This steady state experiment allows us a unique opportunity to see how a rock population changes over a longer travel distance, something we were unable to observe in the unsteady state experiment due to the 10% mass loss target. In our steady-state rock tumbling experiment, additional rock particles are continuously introduced into the system to replace mass lost, better-

representing processes in natural river channels, as well as giving us the opportunity to observe the long-term effects of abrasion on rock particles and possibly two phase abrasion (Domokos et al., 2014). For example, in a river, new sediment is constantly being transported downstream from upland sources that can be in the form of talus slopes adjacent to the river channel, sediment input from tributaries, or rock falls to name a few. In this rock tumbling laboratory experiment, our objective is to observe the interaction of rock grains subjected to attrition and abrasion while simulating the ongoing addition of fresh sediment. The experiment involves introducing angular rocks into a population that may consist mainly of rounded rocks, allowing us to explore how these interactions influence rock particle breakdown and change in shape over time.

Another reason we are conducting this experiment is to see how the changes in rock shape from our particles tumbled in the lab compare with Domokos et al. (2014) two-phase abrasion theory, something that we were not fully able to compare during the unsteady state experiment due to the short overall travel time of rock grains. The constraint from those experiments is that a 10% overall mass loss does not allow for enough travel distance to witness the change from Phase 1 to Phase 2. Through the use of photo image analysis, we will have visual snapshots of how this dynamic new addition of angular rocks into the existing tumbled batch of rocks changes the shape parameters of the rock population.

Furthermore, we are able better understand the production of wear product in the form of fine sediment and fragments over longer distances. Across the span of 25 tumble runs, we track the accumulation of rock fragments and fine sediment generated through attrition and abrasion. Steady-state rock tumbling conditions facilitate the capture of cumulative abrasion effects over

extended travel distances, allowing for the observation of how the introduction of angular grains to an existing grain size distribution grain size and shape, as well as how it contributes to the composition and quantity of wear products. Specifically, we observe how fragmentation and fine sediment production changes as the experiment progresses from an initial population of angular rocks to predominantly rounded rocks over 25 tumble runs, covering a distance of 122.08 kilometers.

2.0 Methods: Steady State Experiment Design

The methodology employed in this experiment closely mirrors that of the unsteady state experiment, with minor adjustments. Physical measurements of rock particles continue to be conducted using a scale and caliper, and the photo processing methods remain consistent, with a single additional step. In the steady state experiment, we initiated with a grain size distribution similar to the narrow GSD in the unsteady state experiment. This steady state narrow GSD started off with a batch mass of 1850g, but unlike the randomized picks within a specified mass range in the previous experiment, it was divided into three subpopulations. Each subpopulation was associated with a specific mass range: (9.0-15.1g), (15.2-25.4g), and (25.5-25.48g).

The initial distribution, outlined in **Table 8**, was characterized by a ratio where 3/6ths of the population originated from the range (9.0-15.1g), 2/6ths from the (15.2-25.4g) mass range, and 1/6th from the mass range (25.5-42.8g). With the setup for the steady state narrow GSD established, the experiment progressed to the tumbling stage, following the pre-tumble methods described previously in Chapter 1. After pre-tumble measurements were taken, rock particles

underwent tumbling with the aim of achieving a target mass loss of 111.0 g per tumble run, equivalent to 6% of the overall batch mass of the steady state narrow GSD. Following this, the same post tumble rock measurement methods described in Chapter 1 of this thesis were conducted to record data.

Wear product methods for this experiment closely resembled those described in Chapter 1 of the unsteady state experiment. Fragments were tallied after each tumble and reintroduced to the rock tumbler, while fine sediment/wear product was extracted, dried, and weighed for its dry weight. Although the targeted mass loss for each run was set at 6%, occasional deviations occurred, with some tumbles falling slightly above or below this threshold. In one instance, there was almost double the mass loss target due to a power outage on campus attributed to inclement weather. Any changes in target mass loss were noted replacement rock grains were added to the experiment, and the same ratio of mass distribution within the specified ranges for the replacement population was maintained.

To substitute the targeted 6% mass loss per run, a set of "buffer rocks" were submerged in water to be readily available for replacing the mass lost during the previous tumble, thereby maintaining the overall batch mass consistent for each subsequent rock tumble. Typically, six rocks were introduced following each rock tumble, adhering to the same 3/6th, 2/6ths, 1/6th ratio. These replacement rocks were photographed separately. Following the physical and digital measurements of these replacement rock grains, they were introduced into the rock population of the previous tumble with a now combined mass that equaled the mass lost during the previous tumble run. This process was repeated a total of 25 time resulting in an overall distance travelled of 112.08 km.

3.0 Results

Within regards to the steady state experiment, this results section investigates how the initial narrow GSD rock population changes in shape from angular to round and measures the overall mass distribution with the addition of angular rocks following each tumble run. Focused on the cumulative impact of shape change over travel distance, we tracked alterations in rock diameter, wear rate over time in a steady state environment, changes in circularity for the rock population, as well as fragment and fine sediment generation. These observations are particularly interesting in steady-state conditions, where the continuous addition of new angular grains mimics the sustained introduction of rocks observed in river environments. Our results aim to form a deeper understanding of how our rock population changes over prolonged distances, as well as the byproducts of abrasion in a controlled laboratory setting which can act as a proxy for natural river processes.

3.1 Particle Size Distribution Over Travel Distance

Figure 15 shows the particle size distribution (PSD) in g of the steady state narrow GSD over the course of the experiment. This plot helps in visualizing the distribution of particles from the initial pre-tumble measurements up until our final measurements following the 25th tumble run. Mass is represented along the x axis increases as you move to the right. The y-axis represents the percentage of mass less than or equal to the corresponding point on the on the x axis. The blue line in Error! Reference source not found. represents our initial pre-tumble measurements and acts as a base reference point to the initial particle size distribution of our experiment. Note that the lower tail of the curve denotes the smallest grain within the initial

distribution. As the experiment progressed, our PSD exhibited a leftward shift of the tail end in each subsequent PSD curve, indicative of an evolving particle size distribution becoming progressively finer-grained. This discernible trend persisted consistently across all tumbling iterations, demonstrating an overall predominantly smaller-grained population. It is noteworthy that, while both the central body and tail of the particle size distribution exhibited this migration towards lower mass, the "head" of the distribution displayed comparatively less pronounced alterations. This can be indicative of the constant addition of larger angular grains into the population to replace mass lost over the course of the experiment, resulting in a less pronounced leftward leaning shift of small grains. Following run 10 of our steady state experiment a more pronounced gap in our PSD curves is noted, this is the result of the mentioned tumble run that exceeded our target mass loss for said tumble run as a result of a power outage on campus due to inclement weather.

3.2 Average Diameter Over Cumulative Travel Distance

Over the course of the steady-state experiment, the analysis of average diameter data reveals a decrease in rock diameters as the distance traveled increases. The provided diameter data, ranging from 2.88 mm to 122.08 mm, illustrates a clear trend of diminishing diameters over the duration of the experiment. **Figure 16** plot of diameter against distance demonstrates a discernible negative correlation, where smaller rock diameters are observed at greater distances.

This observed decrease in diameter aligns with Sternberg's Law of exponential fining. According to Sternberg's law, rocks and sediments tend to undergo a continuous reduction in size as they travel downstream. This phenomenon is attributed to the cumulative effects of attrition

and abrasion during transport, resulting in an exponential decrease in diameter as the travel distance increases. The steady-state tumbling results are consistent with Sternberg's Law, as the rock diameters decrease exponentially over the 122.08 km of distance traveled. This finding visualizes the change in rock shape undergone over large-scale distances. What was surprising was that despite adding angular grains to the experiment following every tumble run, average particle diameter reduction was still prominent over the course of the experiment, rarely increasing in average diameter. The decrease in diameter not only validates theoretical expectations but also provides valuable empirical evidence supporting the applicability of Sternberg's law to the specific conditions of the experimental setup. It is important to note however that while these tumbling experiments can be used to simulate a proxy for particle diameter reduction over distance traveled in a river channel, these are not truly indicative of what is experienced in the natural environment (Miller et al., 2014).

3.3 Alpha Rate Over Cumulative Travel Distance

Figure 17 illustrates alpha rates over the cumulative distance traveled in the steady state experiment. The observed alpha rates span a range from 0.0080 to 0.0210 1/km, indicating a significant variability in the wear intensity experienced by the rocks during the experiment. As seen in **Figure 17**, alpha rates decrease as travel distance increases over the course of the experiment. Despite this trend, variations were observed in between tumble runs where alpha rates would slightly increase, perhaps due to the addition of new angular rock grain particles used to replace mass lost during the previous tumble run. The fluctuations in alpha rates suggest that the wear rates observed during this steady state rock tumbling experiment are possibly

influenced by changing conditions, such as the evolving size distribution of the rock population, and the transition of this population from angular to rounded shapes. As the cumulative travel distance increased, the rocks experience varying degrees of wear, resulting in the observed alpha rate fluctuations as seen in **Figure 17**. This suggest that as the rock population becomes generally rounder, it is more susceptible to fluctuate in wear rate when new angular rocks are introduced into the population. Despite these fluctuations, the wear rate continues to steadily decline over its cumulative travel distance. It was also noted that even during the height of variation of alpha rates, the reduction in diameter remained consistent **Figure 16**. This is not surprising increased wear rates generally mean a higher reduction of mass per km and therefore increased reduction in diameter. During the later stages the alpha rate was seen to stabilize around the same order of magnitude, this indicates that the steady state narrow GSD is neither increasing or decreasing in wear rate as distance continues to increase; resulting in relatively consistent erosion despite the continued addition of rock grains.

3.4 Average Circularity Over Cumulative Travel Distance

The analysis of circularity data over the cumulative travel distance in the steady-state experiment allows us to see how the population of this GSD experiences change in shape from angular to round over a prolonged travel distance compared to the unsteady state experiment. Furthermore, it gives us insight on how a population experiences rounding with the added element of the introduction of angular rock grains continually supplied to the GSD to replace the mass lost from previous tumble runs. As seen in **Figure 18**, average circularity values increased as travel distance increased with values ranging from 0.8126 to 0.9273. Lower average

circularity values may be associated with a population that consists of more angular and irregular rock fragments, while higher values closer to one reflect a population of more rounded rock particles. As seen in **Figure 18**, average circularity values exhibited the most significant increase during the initial tumble runs with some slight variability for the remainder of the experiments. This increase in the initial phase may be attributed to the rapid abrasion-induced rounding of angular rocks as they undergo the early stages of the tumbling process (Domokos et al., 2014; Miller et al., 2014). Towards the later stages of the experiment, a stabilization or plateauing of circularity was observed, this indicates that the population is neither increasing or decreasing out of the current order of magnitude; resulting in relatively consistent rounding.

3.5 Fragment Production Over Cumulative Travel Distance

Figure 19. shows the number of fragments found over the course of the steady state rock tumbling experiment. A consistent upward trend in the number of fragments found following each tumble run over the cumulative distance traveled. This indicates while other variables such as alpha rate and circularity tend to stabilize as the experiment progresses, the production of fragments remains consistent with the exception of the second to last tumble run where fragment count notably dropped. Despite consistent fragment yields fragmentation production was also subject to slight variability. A notable peak in fragment production can be seen in **Figure 19**, between the 42 and 58 km mark. This was due to a tumble run that went beyond the targeted mass loss of 111 g due to a campus power outage related to inclement weather. There is a moderate correlation seen between increases in circularity of the overall rock population and fragment yields. A correlation coefficient of 0.5999 was found between these two parameters

indicating a moderate correlation. This observation suggests a potential link between the increasing circularity, or rounding, of the steady-state narrow GSD rock population and the corresponding rise in the number of fragments found following each tumble run. This phenomenon may be attributed to the rounding process, wherein protruding areas of the rocks undergo erosion or chipping as a consequence of collisions with other grains, ultimately yielding fragments (Domokos et al., 2014; Litwin Miller & Jerolmack, 2021).

3.6 Fine Sediment Production Over Cumulative Travel Distance

Figure 20 illustrates the dry weight of fine sediment in grams (g) collected after each of the 25 tumble runs conducted in the steady state rock tumbling experiment, spanning a cumulative distance of 122.08 kilometers. Fine sediment production was fairly consistent over the course of the experiment due to the nature of the steady state experiment design. Fine sediment produced closely resembled the mass lost for each experiment. Since each tumble run had mass loss target of 6% or 111.0 g, the resulting wear product in the form of fine sediment was within the same order of magnitude. Fine sediment production would vary when tumble runs either went slightly over or under their target mass loss. Overall this was an expected outcome for this experiment. One outlier that can be seen in **Figure 20** at the 58 km mark that can be attributed to Run 11, where a tumble run exceeded its target mass loss due to campus power outage related to inclement weather. This results in the large spike in sediment production seen in **Figure 20**. Subsequent tumbles following this isolated event were similar to fine sediment production trends tied to target mass loss for the remainder of the experiment.

3.7 Overall Mass Distribution

Figure 21 shows the final mass allocation of each individual tumble run over the course of the experiment. Similar to the unsteady state experiment, most of the mass of the rock population remained within the rock grains that were over 1g, as noted by the orange section of the bar graph. This was followed by the fine sediment mass, represented by the red section of the bar graph. This left the remaining allocated mass in the form of fragments, represented by the blue section of the bar graph. While these allocations remained the same over the course of the experiments, more and more mass became allocated in the form of fragments later in the experiment as cumulative travel distance increased. This is visualized in **Figure 21** where the blue section of the bar graph towards the base becomes more prominent as distance increases.

4.0 Discussion

The steady-state rock tumbling experiment aimed to replicate the dynamic conditions of natural river downstream transport by having a continued supply of fresh sediment into our rock tumble. The resulting data gave us the chance to observe rock shape change over a prolonged distance while maintaining a consistent overall batch mass for the steady state narrow GSD. Our observations are reflected in our particle size distribution (PSD) for our steady state experiment.

We created this distribution by plotting a mass by fraction less than plot. Using this type of analysis we observed a consistent leftward shift in our rock populations PSD, indicating an evolving distribution towards smaller particle sizes with overall lower mass with increased distance traveled. This was reflected in exponential reduction of the overall average diameter/b-axis as travel distance increased, despite the addition of new rocks. These findings aligned with

Sternberg's Law (Sternberg, 1875). Alpha, representing the percent of mass lost per km (1/km), exhibited significant variability but showcased an overall decreasing trend as travel distance increased. Circularity increased over travel distance, signifying a transition from angular to rounded rock particles with increased travel. The initial rapid increase of circularity stabilized later in the experiment, indicating a balanced state in the rounding process. Despite the addition of new sediment, circularity neither increased or decreased significantly. Fragment production displayed a consistent upward trend, with a notable outlier linked to a tumble run exceeding the targeted mass loss. A moderate correlation coefficient of 0.599 between circularity increases and fragment yields suggests a possible connection between rounding and fragment generation. Fine sediment production remained fairly consistent, following the expected amount produced similar to the amount of mass lost per tumble, an outlier event emphasized the influence of external factors. Mass allocation maintained a consistent pattern, with an increasing portion allocated to fragments as cumulative travel distance increased. Compared to the unsteady state experiment, the steady-state approach provided a better understanding of long-term rock changes, closely resembling natural processes and offering insights into wear product yields and shape changes over prolonged distances. However, the final allocation of mass generally resembled that of the unsteady state experiment, where most of the mass was retained in rock grains over 1 g, followed by fine sediment, and the remaining mass in the form of fragments produced. Overall, the findings contribute valuable information to the understanding of how a rock population changes in shape over long travel distances (**Table 9 & Table 10**). While these rock tumbling experiments can be used as a proxy for how rocks behave over certain travel distances, it is not a perfect reflection of what happens in natural river environments.

Chapter 3:Methods in Photo Processing

1.0 Introduction

Photo image analysis allows for extracting shape parameters from our rock grains, which is fundamental to understanding change in shape over time. The photos taken of our rock grains between and throughout each tumbling experiment offer a glimpse of small changes in rock grains that are part of a larger geomorphic process. Using photo image analysis techniques in conjunction with rock tumbling, we are better able to track how a batch of river rocks changes shape over time as it is exposed to abrasion in a laboratory setting, which can improve understanding of how a rock particle changes in natural river environments.

One important aspect of photo image analysis is understanding the shape parameters that characterize objects within an image. In our case, the objects within the images are rocks that have undergone varying degrees of abrasion. Shape parameter characteristics have far reaching implications and are even used in fields such as medical imaging, object recognition, and industrial quality control. This chapter is focused entirely on the description and evaluation of methods of photo image analysis, using a combination of MATLAB, the MATLAB Computer Vision Toolbox, ImageJ, Adobe Photoshop, and photo image processing techniques to extract shape parameters via photos taken of rock grains that were used in our experiments, as previously described in Chapter 1 and Chapter 2.

MATLAB's Computer Vision Toolbox provides great functionality for analyzing and manipulating images. It offers a comprehensive set of functions, algorithms, and tools

specifically designed to manipulate and extract data from images via the region props functionality. For our analysis, Dr. Bray developed and wrote the script for a MATLAB-based tool named the “Cobble App”, which includes a Graphical User Interface that allows the student user to enumerate and analyze photos of pre- and post- tumbled rocks. The calculation of shape parameters from images of rocks builds upon previous processing techniques used by Dr. Kim Miller in the paper (Miller et al., 2014). The Cobble App allows us to import and categorize binary versions of our rock images for subsequent photo image analysis.

Methods

2.1 Photo Analysis

In the pursuit of robust rock particle analysis using MATLAB's Computer Vision photo image analysis tools, an image pre-processing protocol was determined to be an important step in accurately calculating the perimeter and shape of rocks. To initiate this process, we started with the acquisition of photos taken on the photo grid with an iPhone 12 Pro during our rock tumbling experiments, which were subsequently migrated to the cloud and then imported into Adobe Photoshop to separate the rock grains from the background. The goal was to produce detailed photos of our rock grains following each tumble run for both the unsteady state and steady state experiments. These photos were then imported into the program ImageJ in order to be converted into a binary format, necessary for importation into various photo processing toolboxes within the MATLAB repository. Binary images were then imported into Dr. Bray’s CobbleApp and shape parameter data was then extracted and merged with our hand-measured data (i.e., mass, diameter) for both the steady and unsteady state experiments.

2.2 Pre-Processing: Photo Grid

As mentioned in previous chapters, part of the measurements of rocks for the tumbling experiment involved the use of the photo grid. This photo grid was made by stapling a black fabric sheet to a large piece of plywood and screwing in an overhead photo rig situated above the fabric covered plywood (**Figure 22**). This fabric sheet was chosen to create the maximum contrast between the background and the rock particle. The camera we used was that of an iPhone 12 Pro which was situated overhead so that there was a birds eye view angle of 48 rock grains placed on the photo board. The camera was positioned so that all aspects needed for subsequent photo analysis were within frame, with a ruler for scale. This was insured by having a marker built in so that the camera would always have the same aspect ratio, height from rock particles, and frame boundaries **Figure 23**. What makes this photo setup unique is its three-camera system in conjunction with the small built-in Lidar sensor that is used in every photo taken in order to maximize resolution and precise focus of rock grains. The photo board also incorporated an X and Y axis that allowed for successful recording of rock grains and the ability to associate both physical and digital data taken for this experiment. This was done by using a table cell structure that employed the use of the two axes on the photo board. The X axis consisted of an ascending alphabetical order (labeled on tape A-H) while the Y axis consisted of a descending numerical order. As seen in **Figure 24**, this system allowed us to create 48 individual locations on our photo board where a rock would then be placed. While we could not track each individual rock from one tumbling run to the next, the enumerated photo grid allowed us to always correlate the hand measurement of a particle's mass to the data record of particle shape from photos. Our photo board also incorporated a yellow meter stick in order to provide a

scale, which is necessary to convert length units in the photo from pixels to mm. Last, our photo board had two overhead lights which were clamped to the overhead photo rig in order to remove the presence of shadows and provide consistent direct overhead lighting across all images (**Figure 22**). The combined functionality of this photo board allowed us to take high resolution images of our rock grains which is crucial for the photo image analysis of how rocks change in shape over a cumulative travel distance as well as attaining precise shape parameters from our images.

2.3 Pre-Processing: Photoshop

The step for photo image pre-processing involves the cropping of our rock grains so that the only thing in frame are the grains themselves. This includes omitting the ruler and the axis of the photo board so that only the rocks are present against the black fabric background. This is followed by carefully outlining each individual rock grain within the photo grid image. This guarantees that each grain is comprehensively enveloped and precisely demarcated, thereby setting the stage for precise calculation of shape characteristics such as the perimeter (**Figure 25**). Following this step, we inverted the object selection outline so that everything outside of the edges of the rock grains is selected. This tool within Photoshop effectively delineates each rock particle from the black fabric background, and distinguishes rocks from the axis labels, ruler, dust on black fabric board, etc. (**Figure 26**). Following this we used the Adobe Photoshop's brush tool, using the black paintbrush to paint over all extraneous elements in the background so that the MATLAB Cobble App can easily identify and enumerate rocks only without additional noise (**Figure 27**). This photo processing step produces an image where only the rock particles

remain, against a black canvas (**Figure 28**). Upon the completion of these steps, the image is archived, bearing its unique photo ID while also noting that it is the “photoshopped” version.

2.4 Pre-Processing: ImageJ

In the next phase, we import the image into a photo processing software called ImageJ, where the image is converted into binary format. This binary format is the format needed for later importation into the CobbleApp for the extraction of shape parameter data. Once one of our photos that was preprocessed in Photoshop enters this environment **Figure 28**, it is ready for manipulation. In ImageJ, the photo is initially converted into greyscale and is then interpolated into 8-bit format, an important first step that sets the stage for subsequent analysis. This conversion ensures optimal compatibility with the MATLAB application curated for this experiment. With our image now primed in greyscale 8-bit format, the next stride involved is the application of the edge detection tool. This tool adeptly traces the contours and ridges of the rock particles, providing a great foundation for the conversion into binary format as seen in **Figure 29**. This was a pivot from methods done in the past. Previously, images would be thresholded until the rock particles present in the photo were filled in.

Following the edge detection process, the image is now ready for conversion into binary using ImageJ’s binary conversion tool this effectively pixelates the image into a black and white render as seen in **Figure 30**. To further refine its integrity, we employed the 'fill holes' function, which diligently tends to any voids within the boundaries of the detected edges (**Figure 31**). This methodology was found to eliminate points of potential error compared to using the thresholding approach where rock grains dimensions could be potentially distorted while undergoing

thresholding. This new methodology makes it so that rock grains are edges are preserved first and foremost, and then subsequently filled in. It is noteworthy that, while this step is highly effective, occasional imperfections may persist.

In instances where the edge detection tool fails to connect the outline of a particle resulting in unfilled spaces within the rock grain, a personal touch is required. Here, the ImageJ paintbrush tool can be used for quality control. By zooming in until the particle occupies the entire screen, and delicately applying the paintbrush tool, voids are filled to mitigate the risk of inadvertently incorporating pixels beyond the rock particle's edge boundary. Surpassing a particle's edge boundary is one of the most important parts of quality control, even a small change to a rock's perimeter can affect the circularity value attained later on. This approach ensured the fidelity of our later analysis (**Figure 32**). The final step conducted in this process was to invert the image so that the filled-in particles were perfectly contrasted against a black background. With our now finalized image (**Figure 33**), the binary rock particles were ready for analysis using our MATLAB application, CobbleApp.

2.5 Data Extraction: CobbleApp

During the course of our experiment, Dr. Bray curated a MATLAB application that consisted of a script that integrated MATLAB computer vision toolbox, image processing toolbox, as well as statistical and machine learning toolbox. The MATLAB Computer Vision Toolbox, Image Processing Toolbox, and Statistical and Machine Learning Toolbox are powerful resources that collectively offer a suite of tools for analyzing visual data. These toolboxes are invaluable in extracting meaningful information from images, making them

particularly useful for applications ranging from object recognition to image enhancement and statistical modeling.

The Computer Vision Toolbox is specialized for tasks involving image and video processing, offering a wide range of functions for tasks like feature detection, image segmentation, object recognition, and geometric transformations. This toolbox provides a robust foundation for processing visual data, enabling the extraction of pertinent features and attributes from the binary images of our rock particles.

The Image Processing Toolbox, on the other hand, is designed for fundamental image processing tasks, such as filtering, noise reduction, image enhancement, and morphological operations. It equips users with a versatile set of algorithms to manipulate and refine images, allowing for a detailed analysis of visual data. Complementing these, the Statistical and Machine Learning Toolbox empowers users to apply statistical methods and machine learning techniques to extract meaningful insights from data. This includes tasks like classification, regression, clustering, and dimensionality reduction, all of which can be applied to image data for various analytical purposes. When applied collectively, these toolboxes were a valuable resource as they were used in the core of the CobbleApps functionality.

The main functionality of our MATLAB script came from the `'regionprops'` function, a useful tool for extracting quantitative attributes from our binary images fed into the CobbleApp. This function facilitated the extraction of key metrics, including circularity, area (representing the pixel count within a rock particle) and perimeter (measuring the boundary length in pixels), major axis, minor axis, and eccentricity. Additionally, it computed centroid coordinates and bounding box dimensions, enabling precise localization and orientation of our rock particles

(**Figure 34**). This was pivotal for associating each rock in the image with physical data later on using photo ID. Further outputs encompassed eccentricity, orientation, as well as major and minor axis lengths, which aligned with our physical measurements taken using a caliper. The major axis corresponded to the A-axis, while the minor axis represented the B-axis.

Binary images pre-processed via Image J were subsequently imported into the CobbleApp for comprehensive data tabulation. Most photographs encompassed 48 rock particles, adhering to the maximum capacity of the photo grid outline. The CobbleApp seamlessly labeled rocks from their centroid in the order of their physical measurements, yielding a data table for each identified rock particle tied to its unique photo ID (**Figure 34**). However, numerous runs exceeded 48 rocks, at times filling only half the photo grid when measuring rocks towards the tail end. To address this, a custom function was devised. In instances where 48 rock particles weren't automatically detected, the user was prompted to input the number of rock particles present in each column of the binary image (**Figure 35**). This instructed the CobbleApp on where to allocate the extracted data. As highlighted in Chapter 1, most runs entailed more than 48 rocks, thus each run usually contained 2-5 photos per run. To compile a comprehensive dataset encompassing all measured rock particles, an append function was incorporated into CobbleApp's functionality and user interface. This feature facilitated the seamless stitching of multiple photos, all belonging to the same run, resulting in a more comprehensive dataset for streamlined variable retrieval during subsequent analyses.

At this juncture, we possessed two sets of data for every rock particle: one from our physical measurements and another from digital measurements. Our goal was to merge these two datasets for statistical analysis down the line. The final functionality embedded into the CobbleApp was

the merge function. This capability enabled the amalgamation of digital data with physical data, yielding a unified dataset for each run within every grain size distribution. Since both physical and digital measurements were acquired in a consistent order, the CobbleApp intuitively paired the digital and physical measurements based on their unique photo ID, resulting in our final condensed dataset for that specific tumble run (**Figure 36**).

3.0 Results: Effects of Resolution on Circularity

Upon observing the circularity values of our pre-tumble photos, a notable deviation from previous studies in the field came to light (Miller et al., 2014; Szabo et al., 2015). Typically, prior experiments recorded initial circularity values ranging from 0.6 to 0.7. In contrast, our circularity experiment yielded initial values within a higher range, specifically between 0.78 to 0.825 (Szabo et al., 2015). This discrepancy prompted a closer examination, leading to the realization that circularity values from previous experiments were intentionally downgraded to match the resolution of images captured on Mars (Szabo et al., 2015). This adjustment ensured an identical DPI/scale, enabling a precise comparative analysis between rocks on Mars and higher-resolution photos of rocks taken here on Earth. To achieve this, a specialized bicubic interpolation MATLAB script was employed to resize the entire image while preserving its scale. The outcome revealed a direct correlation between resolution and circularity, where an increase in resolution led to a decrease in circularity (Miller et al., 2014; Szabo et al., 2015). The proxy for resolution used in their study was the number of pixels per contour, ultimately culminating in a final resolution of 70 pixels per contour, mirroring that of the Mars rock image (Szabo et al., 2015).

Our objective was to replicate this experiment; however, we encountered a limitation as we lacked access to the specialized MATLAB bicubic interpolation script (Szabo et al., 2015). To closely emulate the process of reducing resolution while maintaining scale, we turned to Photoshop's bicubic interpolation. This method was applied to the meticulously cleaned versions of the raw rock particle photos.

In our experiment, we selected five random photos from our earlier unsteady-state experiment. These images underwent circularity measurements using two distinct methods. The initial approach, denoted as “Method 1”, involved circularity calculations based solely on the raw cropped images imported into ImageJ. Conversely, “Method 2” entailed a preliminary step where images were refined in Photoshop to isolate rock grains against a clean black background before being transformed into binary images (**Figure 28**). The outcomes of these experiments are summarized in (**Table 7**). Notably, “Method 2” yielded superior results characterized by higher image quality with well-defined edges and more precise circularity values. As seen in **Table 7**, each test photo returned a lower circularity value with the use of “Method 2” compared to circularity values calculated via “Method 1” (**Figure 37**). Based on these findings, we elected to adopt “Method 2” for subsequent photo analysis, ensuring a more accurate representation of how resolution impacts the circularity of rock grains.

For the second part of our experiment, our aim was to systematically lower the resolution of each photo from its original 100% state, progressively employing Photoshop's bicubic interpolation. In the downgraded resolution experiment, we opted for three distinct resolution levels. Initially, we retained 100% resolution to serve as our control, representing the baseline original resolution. We then proceeded to downgrade the resolution to 75% of the original, followed by a further

reduction to 25% of the original resolution. To achieve this, we employed Photoshop's bicubic image interpolation method, ensuring that the scale was preserved during the downsizing process. Subsequently, these modified images were processed through the CobbleApp to extract circularity values, allowing for a comprehensive analysis of how circularity is influenced by resolution.

It's interesting to note that the decrease in resolution to 75% resulted in lower values for circularity. This decrease was observed across all tested photos, with circularity values averaging 2% lower compared to those at 100% resolution. This suggests a consistent signal of lower circularity values with reduced to 75% resolution.

However, this lowered circularity return did not stay consistent when the resolution was further lowered to 25% resolution. Here, we observed an increase in circularity values, bringing them into the same order of magnitude as those observed in Method 2 at 100% resolution (**Table 7**). Notably, these values also surpassed those obtained at 75% resolution. This intriguing finding suggests that the relationship between resolution and circularity may not be straightforward, and further investigation may be warranted to understand the underlying mechanisms at play. While these values did not seem too far off from each other we wanted to run a statistical analysis to see if there was a significant difference between these three methods. In order to note whether there is any significant difference between methods we ran an ANOVA statistical analysis with a H0 that stated that these values were inherently equal and that the method/resolution had no impactful effect on circularity. As seen in **Figure 41**, our results yielded a relatively low P-Value of $9.8634e-05$, indicating that there is strong evidence to reject the null hypothesis. In this

context, it suggests that there are significant differences in circularity results between the methods/resolution used and its effects on circularity values yielded.

To delve further we ran a Tukey-HSD statistical test in order to see if there was any significant difference in mean circularity between methods tested. **Figure 42** showcases that there were no significant differences in means between methods tested. If a Tukey Honestly Significant Difference (HSD) test shows no significant difference of means between the methods tested, it indicates that, based on the available data, there is not enough evidence to conclude that any specific method significantly outperforms the others. In other words, the means of the circularity values obtained from the different methods are statistically similar (**Figure 42**).

While a low p-value in an ANOVA test indicates that there is a significant difference in at least one pair of means among the methods being compared. The results of our Tukey HSD test suggests that there is little difference in mean circularity values between all methods/ resolution as a whole. When conducting post-hoc tests like the Tukey HSD test, the goal is to determine which specific pairs of means are significantly different from each other. In this case, the Tukey HSD test did not find any significant differences, this means that while there may be an overall difference (as indicated by the low p-value from the ANOVA test), when you look at specific pairs of methods, the differences in their means are not statistically significant. For the purposes of our experiment, the ANOVA test is giving a broad view that there is some difference in means among the methods, but the Tukey HSD test examines the specific pairs and found that despite the overall difference, all pairs of methods/resolution tested are not significantly different from each other. This suggests that, for this dataset, the choice of method for circularity measurement may not have a substantial impact on the overall results. This is apparent as results from all

methods used were within the same order of magnitude. Future users can potentially select the method that is most convenient or practical for their specific experimental setup, without a significant concern for circularity bias. However, it's crucial to remember that this interpretation is specific to the dataset and conditions under which the experiments were conducted, the camera used for the experiment, and the user's preprocessing methodology. This thesis chapter does not address possible variations in circularity that arise from two different users. For the purposes of our experiment, the ANOVA test is giving a broad view that there is some difference in means among the methods, but the Tukey HSD test examines the specific pairs and found that despite the overall difference, all pairs of methods/resolution tested are not significantly different from each other. This suggests that, for this dataset, the choice of method for circularity measurement may not have a substantial impact on the overall results. This is apparent as results from all methods used were within the same order of magnitude. Future users can potentially select the method that is most convenient or practical for their specific experimental setup, without a significant concern for circularity bias. However, it's crucial to remember that this interpretation is specific to the dataset and conditions under which the experiments were conducted, the camera used for the experiment, and the user's preprocessing methodology. This thesis chapter does not address possible variations in circularity that arise from two different users.

4.0 Discussion

These results gave us an idea of how methods employed in photo processing for the analysis of rock grain shape parameters, particularly focusing on the effects of resolution on circularity values can be used for quantifying how rocks change in shape as they erode. The use

of MATLAB's Computer Vision Toolbox, Image Processing Toolbox, and Statistical and Machine Learning Toolbox into the CobbleApp has proven to be a powerful combination of tools, enabling the extraction of meaningful data from high-resolution images captured during rock tumbling experiments.

The experiment design, starting from the acquisition of photos using our photo grid and culminating in the extraction of shape parameters through the CobbleApp, represents an approach that yields high resolution images for accurate binary representation of rock grains. The utilization of a lidar sensor enabled three-camera system, and a carefully designed photo board ensures image integrity and quality control. The detailed procedures outlined in this chapter serve as a guide for future researchers seeking to employ similar methodologies in the study of rock shape evolution.

The testing of the effects of resolution on circularity values has revealed interesting results. The statistical analyses, including ANOVA and Tukey HSD tests, have provided insights into the significance of method and resolution choices in circularity measurement. While the ANOVA test suggests an overall difference, the Tukey HSD test indicates that specific pairs of methods mentioned in this chapter are statistically similar, suggesting that researchers may have flexibility in choosing a method based on convenience without substantial impact on results. This reasoning is exclusive to methods used in these experiments. The extraction of shape parameters from images provides valuable insights into object characterization, and the presented methodology offers a framework for researchers to adapt and apply in various visual data analysis scenarios.

In summary, this chapter has provided a detailed account of the methods employed in photo processing for rock grain analysis, shedding light on the intricate process of shape parameter extraction. This approach outlined here not only contributes to the understanding of how rocks change in shape over distance traveled but also serves as a valuable resource for researchers navigating the complexities of image analysis and shape parameter extraction. This was something that I found hard to find resources for when setting up a methodology for our rock grain analysis.

References/Bibliography/Works Cited

- Arabnia, L. S. (2016). Experimental Study of Particle Size Reduction in Geophysical Granular Flows.
- Attal, M., & Lavé, J. (2009). Pebble abrasion during fluvial transport: Experimental results and implications for the evolution of the sediment load along rivers. *Journal of Geophysical Research: Earth Surface*, 114(F4).
<https://doi.org/10.1029/2009jf001328>
- Bodek, S., & Jerolmack, D. J. (2021). Breaking down chipping and fragmentation in sediment transport: the control of material strength.
<https://doi.org/10.5194/esurf-2021-17>
- Bylak, A., & Kukuła, K. (2022). Impact of fine-grained sediment on mountain stream macroinvertebrate communities: Forestry activities and beaver-induced sediment management. *The Science of the total environment*, 832, 155079-155079.
<https://doi.org/10.1016/j.scitotenv.2022.155079>
- Cassel, M., Lave, J., Recking, A., Malavoi, J. R., & Piegay, H. (2021). Bedload transport in rivers, size matters but so does shape. *Sci Rep*, 11(1), 508.
<https://doi.org/10.1038/s41598-020-79930-7>
- Cohen, A. S., Bills, R., Cocquyt, C. Z., & Caljon, A. G. (1993). The Impact of Sediment Pollution on Biodiversity in Lake Tanganyika. *Conservation Biology*, 7(3), 667-677. <http://www.jstor.org/stable/2386698>
- Dietrich, L. S. S. W. E. (2001). Sediment and rock strength controls on river incision into bedrock.
- Dingle, E. H., Attal, M., & Sinclair, H. D. (2017). Abrasion-set limits on Himalayan gravel flux. *Nature*, 544(7651), 471-474.
<https://doi.org/10.1038/nature22039>
- Dingle, E. H., Kusack, K. M., & Venditti, J. G. (2021). The gravel-sand transition and grain size gap in river bed sediments. *Earth-Science Reviews*, 222.
<https://doi.org/10.1016/j.earscirev.2021.103838>
- Domokos, G., Jerolmack, D. J., Sipos, A. A., & Torok, A. (2014). How river rocks round: resolving the shape-size paradox. *PLoS One*, 9(2), e88657.
<https://doi.org/10.1371/journal.pone.0088657>
- Hupp, C. R., & Osterkamp, W. R. (1996). Riparian vegetation and fluvial geomorphic processes. *Geomorphology (Amsterdam)*, 14(4), 277-295.
[https://doi.org/10.1016/0169-555X\(95\)00042-4](https://doi.org/10.1016/0169-555X(95)00042-4)

- Kondolf, G. M. (1997). PROFILE: Hungry Water: Effects of Dams and Gravel Mining on River Channels. *Environ Manage*, 21(4), 533-551.
<https://doi.org/10.1007/s002679900048>
- Kondolf, G. M., Piegay, H., & Landon, N. (2002). Channel response to increased and decreased bedload supply from land use change; contrasts between two catchments. *Geomorphology (Amsterdam)*, 45(1-2), 35-51.
[https://doi.org/10.1016/S0169-555X\(01\)00188-X](https://doi.org/10.1016/S0169-555X(01)00188-X)
- Kondolf, G. M., & Wolman, M. G. (1993). The sizes of salmonid spawning gravels. *Water Resources Research*, 29(7), 2275-2285.
<https://doi.org/10.1029/93WR00402>
- Lisle, T. E., & Hilton, S. (1999). Fine bed material in pools of natural gravel bed channels. *Water Resources Research*, 35(4), 1291-1304.
<https://doi.org/10.1029/1998wr900088>
- Litwin Miller, K., & Jerolmack, D. (2021). Controls on the rates and products of particle attrition by bed-load collisions. *Earth Surface Dynamics*, 9(4), 755-770.
<https://doi.org/10.5194/esurf-9-755-2021>
- Luetzenburg, G., Kroon, A., & Bjork, A. A. (2021). Evaluation of the Apple iPhone 12 Pro LiDAR for an Application in Geosciences. *Sci Rep*, 11(1), 22221.
<https://doi.org/10.1038/s41598-021-01763-9>
- Mason, R. J., Rice, S. P., Wood, P. J., & Johnson, M. F. (2019). The zoogeomorphology of case-building caddisfly: Quantifying sediment use. *Earth Surface Processes and Landforms*, 44(12), 2510-2525.
<https://doi.org/10.1002/esp.4670>
- McMahon, A., & Moore, R. D. (2017). Influence of turbidity and aeration on the albedo of mountain streams. *Hydrological processes*, 31(25), 4477-4491.
<https://doi.org/10.1002/hyp.11370>
- Miller, K. L., Szabó, T., Jerolmack, D. J., & Domokos, G. (2014). Quantifying the significance of abrasion and selective transport for downstream fluvial grain size evolution. *Journal of Geophysical Research: Earth Surface*, 119(11), 2412-2429.
<https://doi.org/10.1002/2014jf003156>
- Park, J.-Y., Gayes, P. T., & Wells, J. T. (2009). Monitoring Beach Renourishment along the Sediment-Starved Shoreline of Grand Strand, South Carolina. *Journal of Coastal Research*, 25(2), 336-394. <http://www.jstor.org/stable/27698326>
- Parker, G. (1991). Selective sorting and abrasion of river gravel, Theory.
- Parker, G. (1991). Selective sorting and abrasion of rivergravel, Application.
- Sipos, A. A., Domokos, G., & Török, J. (2021). Particle size dynamics in abrading pebble populations. *Earth Surface Dynamics*, 9(2), 235-251.
<https://doi.org/10.5194/esurf-9-235-2021>

- Sklar, L. S., Dietrich, W. E., Fournoula-Georgiou, E., Lashermes, B., & Bellugi, D. (2006). Do gravel bed river size distributions record channel network structure? *Water Resources Research*, 42(6). <https://doi.org/10.1029/2006wr005035>
- Sklar, L. S., Riebe, C. S., Marshall, J. A., Genetti, J., Leclere, S., Lukens, C. L., & Mercus, V. (2017). The problem of predicting the size distribution of sediment supplied by hillslopes to rivers. *Geomorphology*, 277, 31-49. <https://doi.org/10.1016/j.geomorph.2016.05.005>
- Sternberg, H. (1875). *Untersuchungen über längen- und querprofil geschiebeführender Flüsse*. [publisher not identified] [Place of publication not identified].
- Szabo, T. (2015). Supplemental.
- Szabo, T., Domokos, G., Grotzinger, J. P., & Jerolmack, D. J. (2015). Reconstructing the transport history of pebbles on Mars. *Nat Commun*, 6, 8366. <https://doi.org/10.1038/ncomms9366>
- Szabó, T., Fityus, S., & Domokos, G. (2013). Abrasion model of downstream changes in grain shape and size along the Williams River, Australia. *Journal of Geophysical Research: Earth Surface*, 118(4), 2059-2071. <https://doi.org/10.1002/jgrf.20142>
- Szabó, T. m. (2013). A MECHANICS-BASED PEBBLE SHAPE CLASSIFICATION SYSTEM AND THE NUMERICAL SIMULATION OF THE COLLECTIVE SHAPE EVOLUTION OF PEBBLES.
- Thornbury, W. D. (1954). *Principles in Geomorphology*. New York, John Wiley & Sons, 618 pp.
- Tímea Novák-Szabó, 2 András Árpád Sipos,2,3 Sam Shaw,1 Duccio Bertoni,4,5 Alessandro Pozzebon,6 Edoardo Grottoli,5 Giovanni Sarti,4 Paolo Ciavola,5 Gábor Domokos,2,3 Douglas J. Jerolmack1,7*. (2018). Universal characteristics of particle shape evolution by bed-load chipping.
- Turowski, J. M., Wyss, C. R., & Beer, A. R. (2015). Grain size effects on energy delivery to the streambed and links to bedrock erosion. *Geophysical Research Letters*, 42(6), 1775-1780. <https://doi.org/10.1002/2015gl063159>
- Tyrrell, J. (2015). THE EFFECT OF WATER TEMPERATURE ON IN-STREAM SEDIMENT CONCENTRATION AND TRANSPORT RATE.
- Verdian, J. P., Sklar, L. S., Riebe, C. S., & Moore, J. R. (2021). Sediment size on talus slopes correlates with fracture spacing on bedrock cliffs: implications for predicting initial sediment size distributions on hillslopes. *Earth Surface Dynamics*, 9(4), 1073-1090. <https://doi.org/10.5194/esurf-9-1073-2021>
- Warrick, J. A. (2020). Littoral Sediment From Rivers: Patterns, Rates and Processes of River Mouth Morphodynamics [Original Research]. *Frontiers in Earth Science*, 8. <https://doi.org/10.3389/feart.2020.00355>

- Warrick, J. A. (2020). Littoral Sediment From Rivers: Patterns, Rates and Processes of River Mouth Morphodynamics [Original Research]. *Frontiers in Earth Science*, 8. <https://doi.org/10.3389/feart.2020.00355>
- Whipple, K. X. (2000). River incision into bedrock: Mechanics and relative efficacy of plucking, abrasion and cavitation.
- Whipple, K. X., & Tucker, G. E. (2002). Implications of sediment-flux-dependent river incision models for landscape evolution. *Journal of Geophysical Research: Solid Earth*, 107(B2), ETG 3-1-ETG 3-20. <https://doi.org/https://doi.org/10.1029/2000JB000044>
- Wickert, A. D., & Schildgen, T. F. (2019). Long-profile evolution of transport-limited gravel-bed rivers. *Earth Surface Dynamics*, 7(1), 17-43. <https://doi.org/10.5194/esurf-7-17-2019>
- Wolman, G. M. K. M. G. (1993). The Sizes of Salmonid Spawning Gravels. *Water Resources Research*, Vol.7.

Appendix/Appendices

Appendix A: List of California State University Campuses

California State University, Bakersfield
California State University Channel Islands
California State University, Chico
California State University, Dominguez Hills
California State University, East Bay
California State University, Fresno
California State University, Fullerton
Humboldt State University
California State University, Long Beach
California State University, Los Angeles
California State University Maritime Academy
California State University, Monterey Bay
California State University, Northridge
California State Polytechnic University, Pomona
California State University, Sacramento
California State University, San Bernardino
San Diego State University
San Francisco State University
San José State University
California Polytechnic State University, San Luis Obispo
California State University San Marcos
Sonoma State University
California State University, Stanislaus

Appendix B: Abbreviations of California State University Campuses

CSU Bakersfield
CSU Channel Islands
Chico State
CSU Dominguez Hills
Cal State East Bay
Fresno State
Cal State Fullerton
Humboldt State
Cal State Long Beach
Cal State LA
Cal Maritime
CSU Monterey Bay
CSUN
Cal Poly Pomona
Sacramento State
Cal State San Bernardino
San Diego State
San Francisco State
San José State
Cal Poly San Luis Obispo
CSU San Marcos
Sonoma State
Stanislaus State

Figures

Figure 1. Map of the watershed where samples were collected. The collection point is denoted by the red triangle on map.

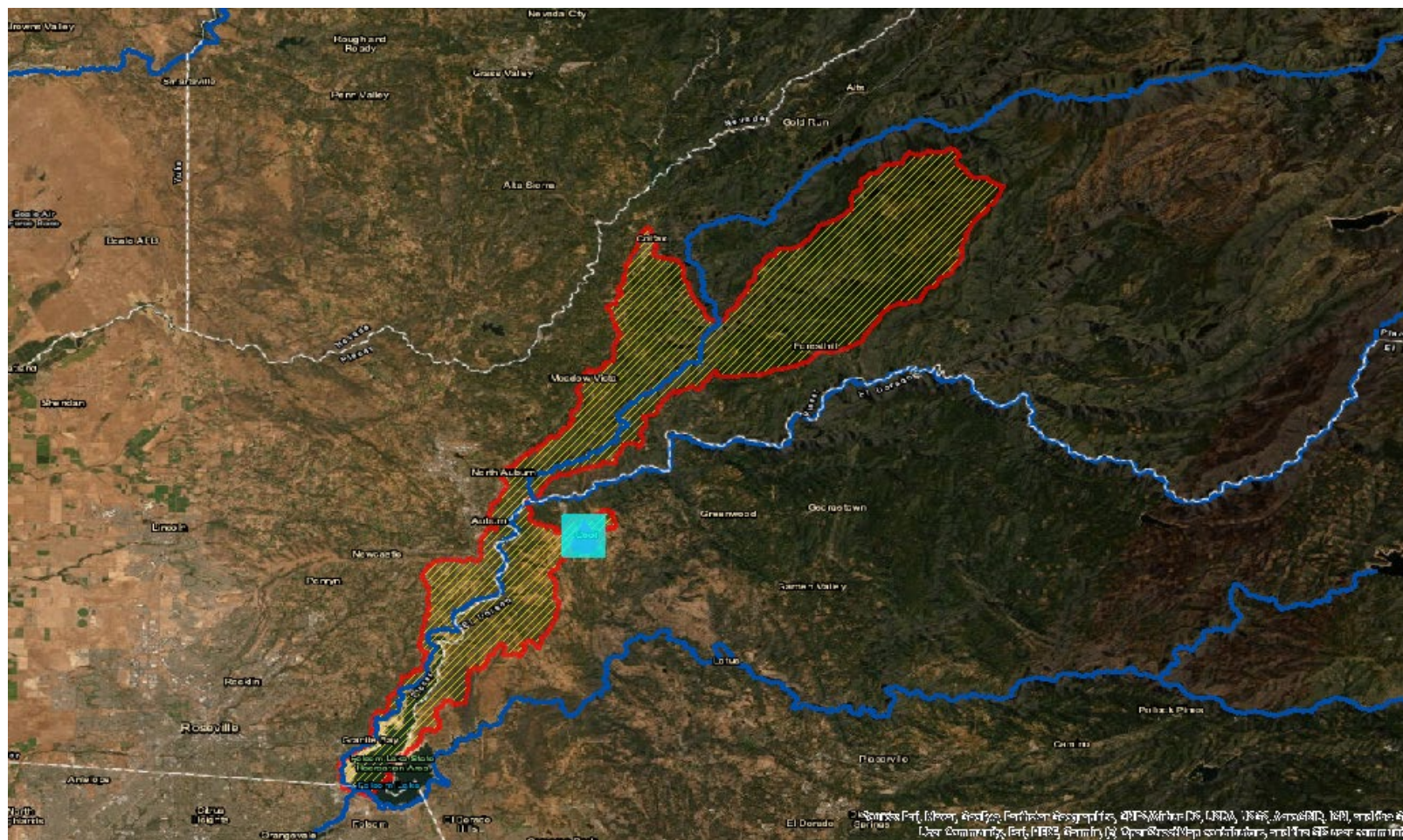
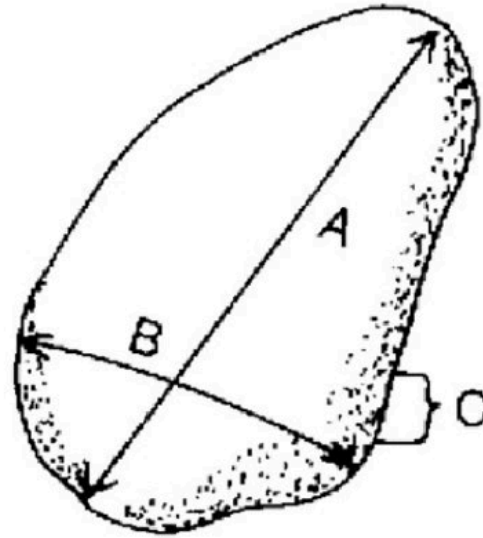


Figure 2. Diagram of three different axes (Harrelson et al.,1994).



A = LONGEST AXIS (LENGTH)

B = INTERMEDIATE AXIS (WIDTH)

C = SHORTEST AXIS (THICKNESS)

Figure 3. Tools used in order to measure rock particle mass and axis dimensions.



Figure 4. Internal grooves of rock tumbling cylinder



Figure 5. Rock tumbling machine



Figure 6. Unsteady state initial grain size distribution

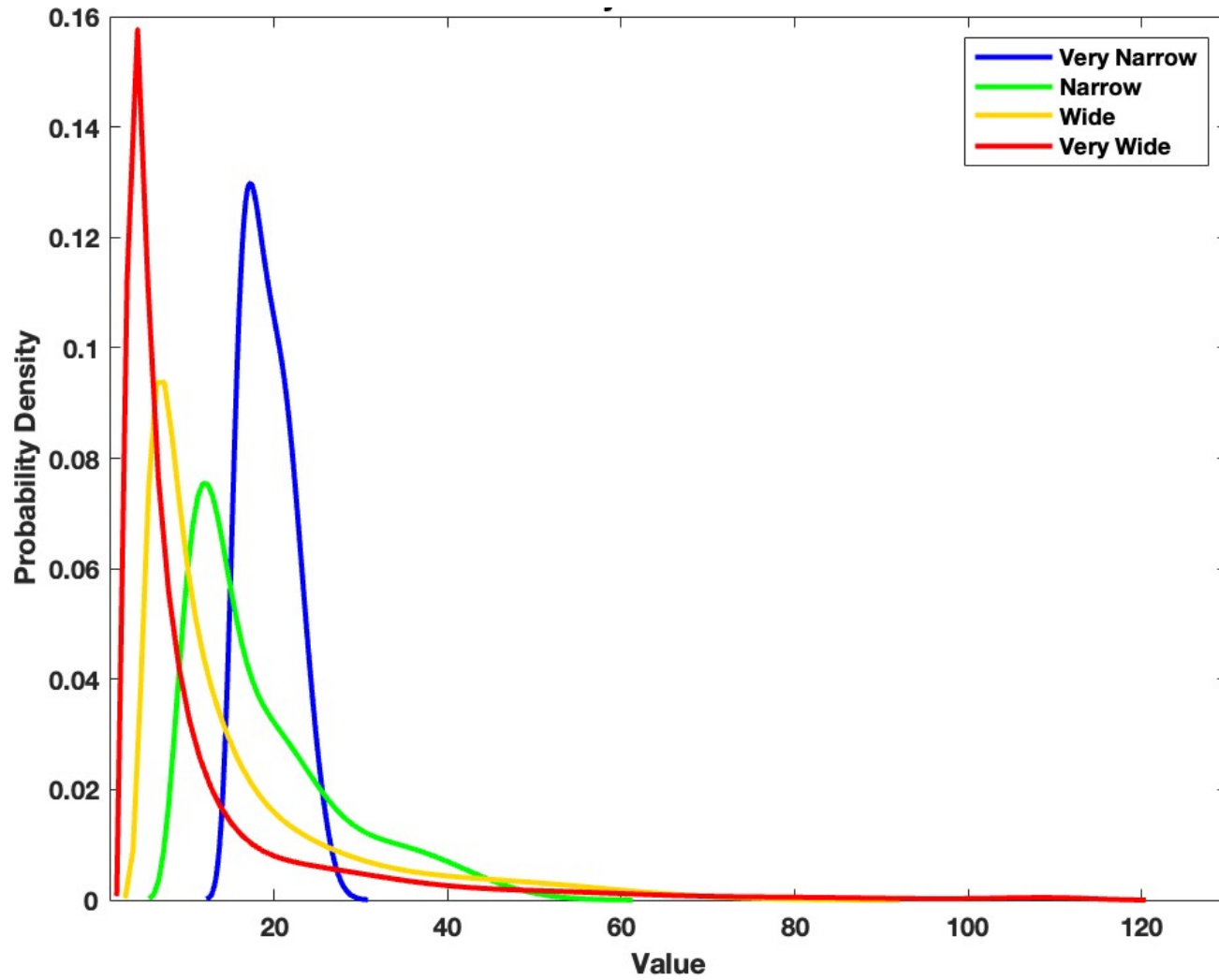


Figure 7. Unsteady state experiment mass loss over cumulative travel distance

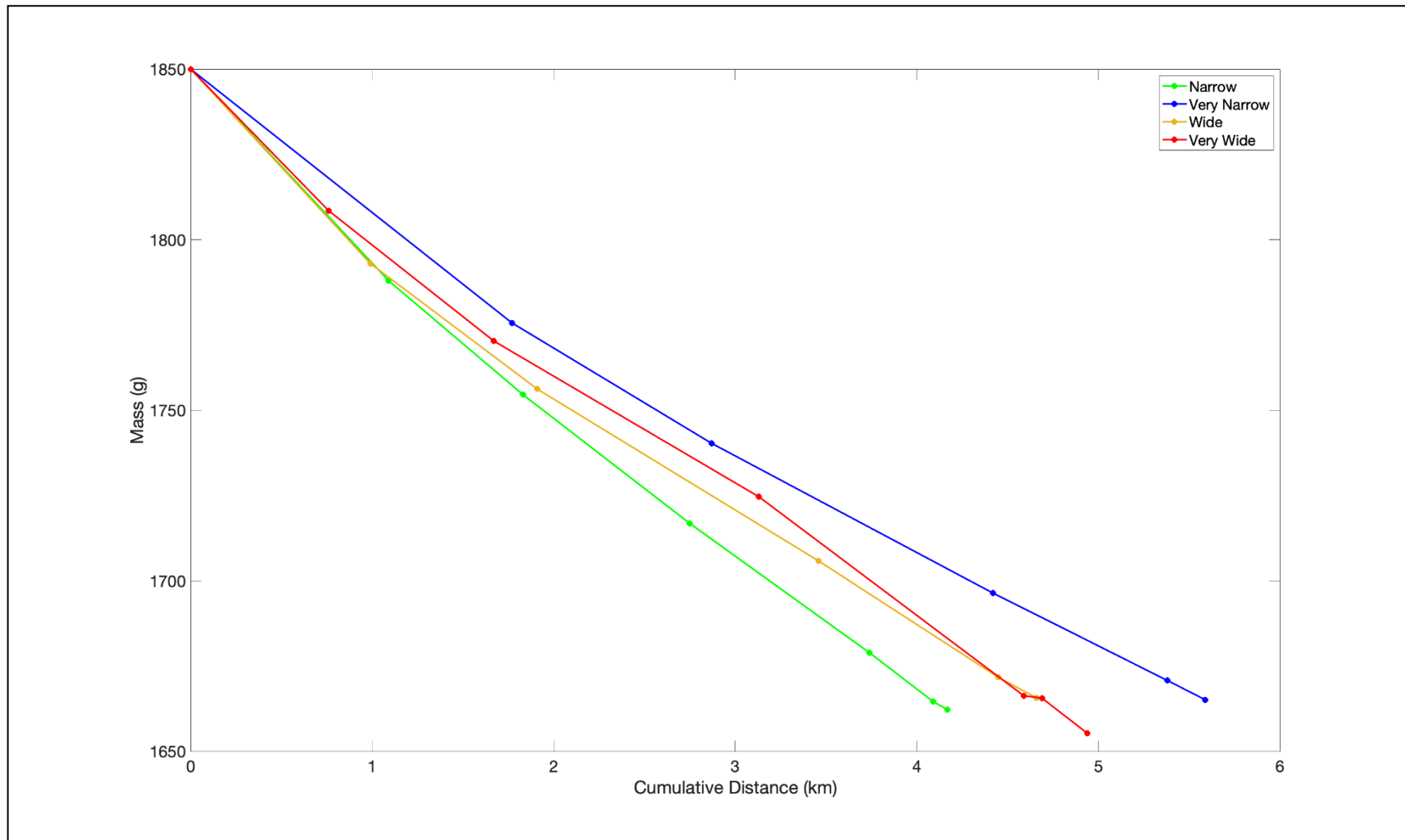


Figure 8. Unsteady state experiment average diameter over cumulative travel distance

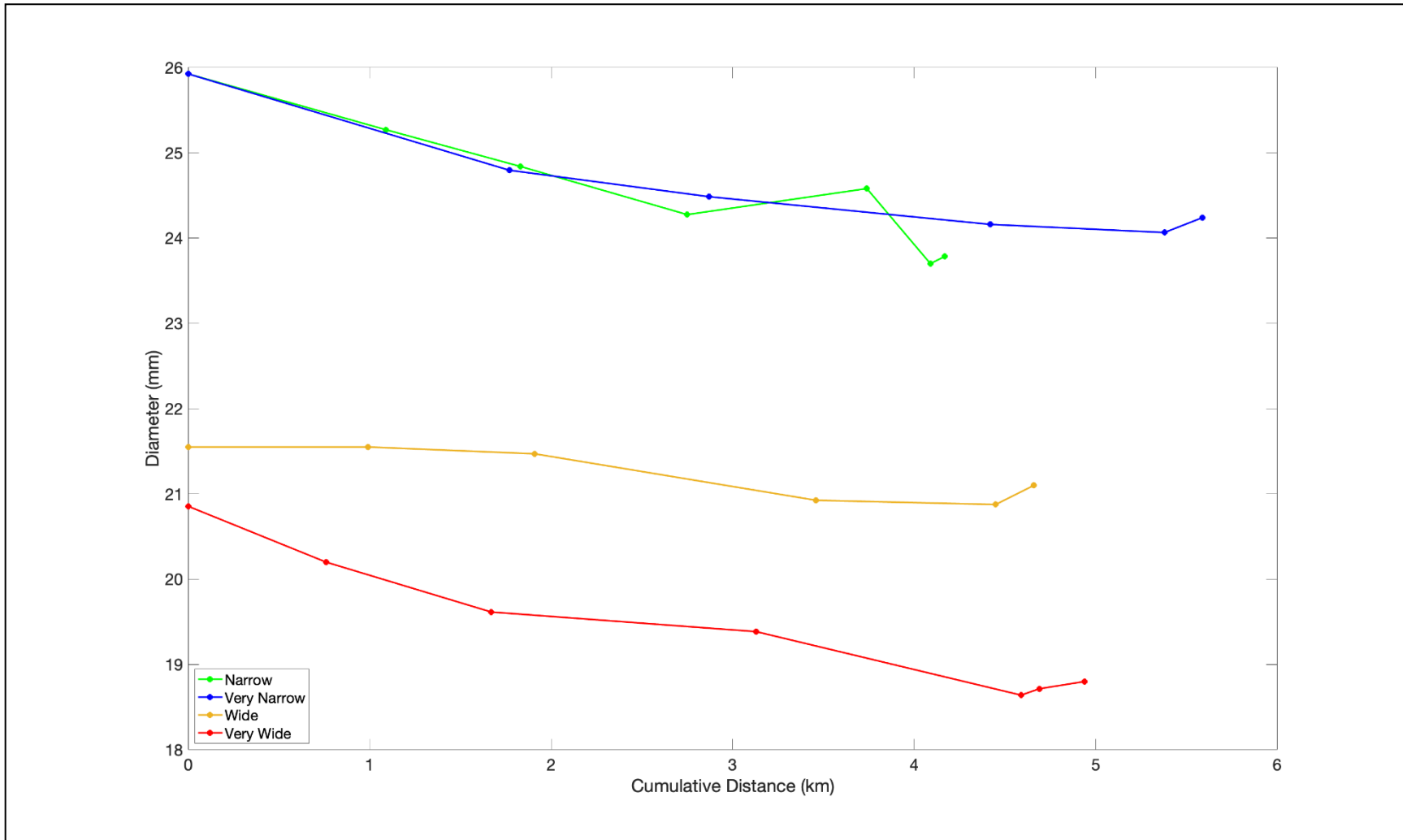


Figure 9. Unsteady state alpha rate over cumulative travel distance

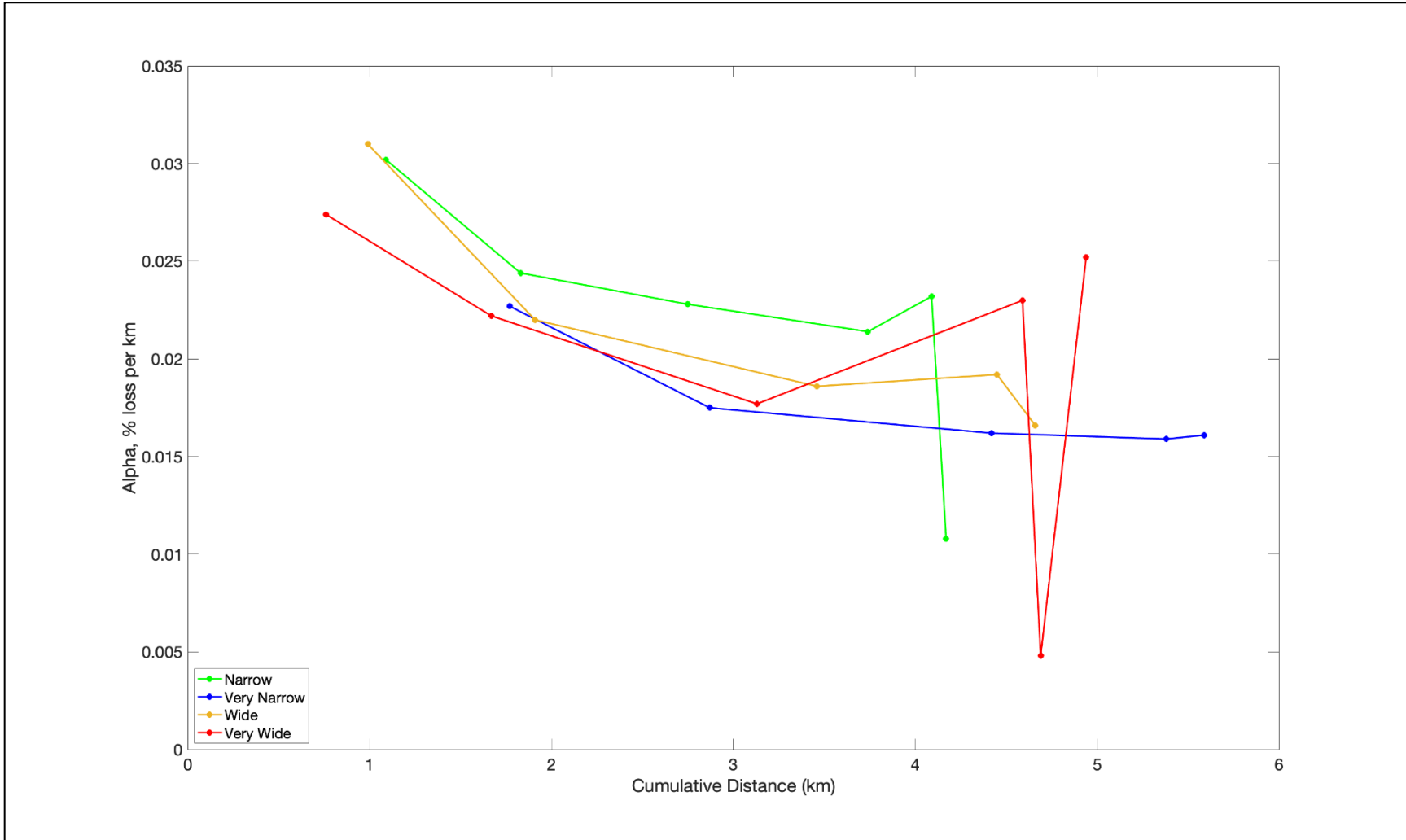


Figure 10. Unsteady state experiment median circularity over cumulative travel distance

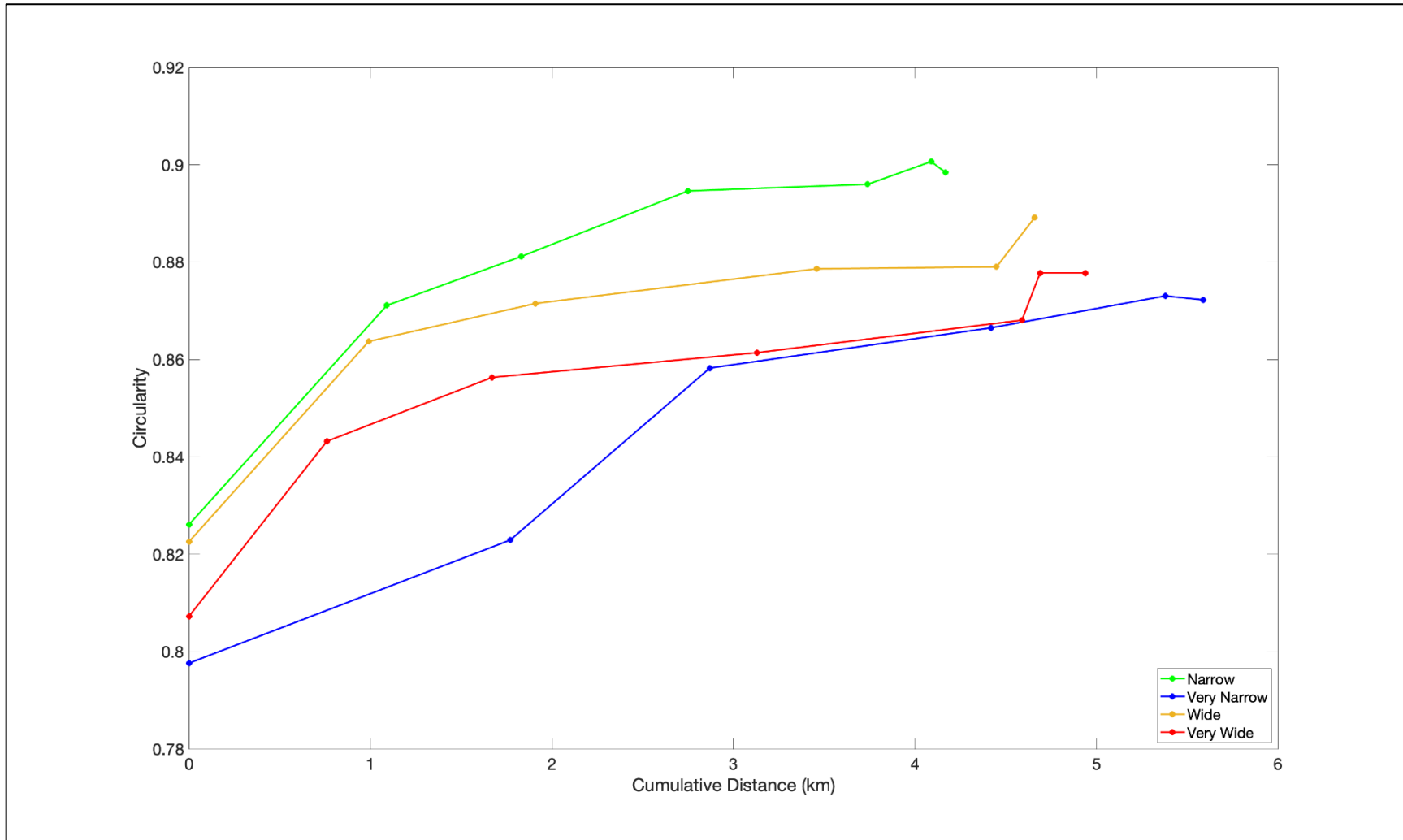


Figure 11. Unsteady state experiment wear product/fine sediment production over cumulative travel distance

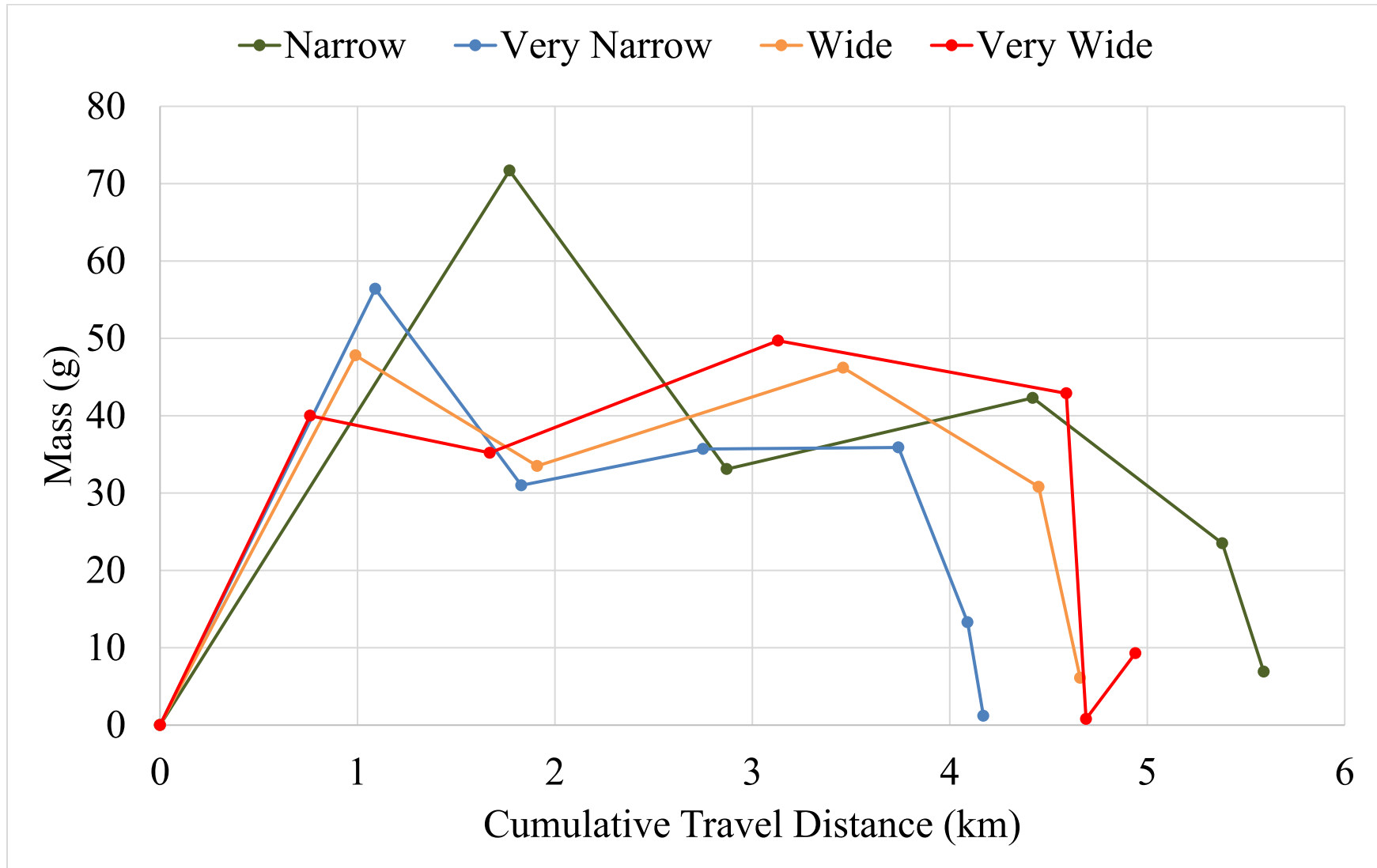


Figure 12. Unsteady state experiment fragments observed over cumulative travel distance

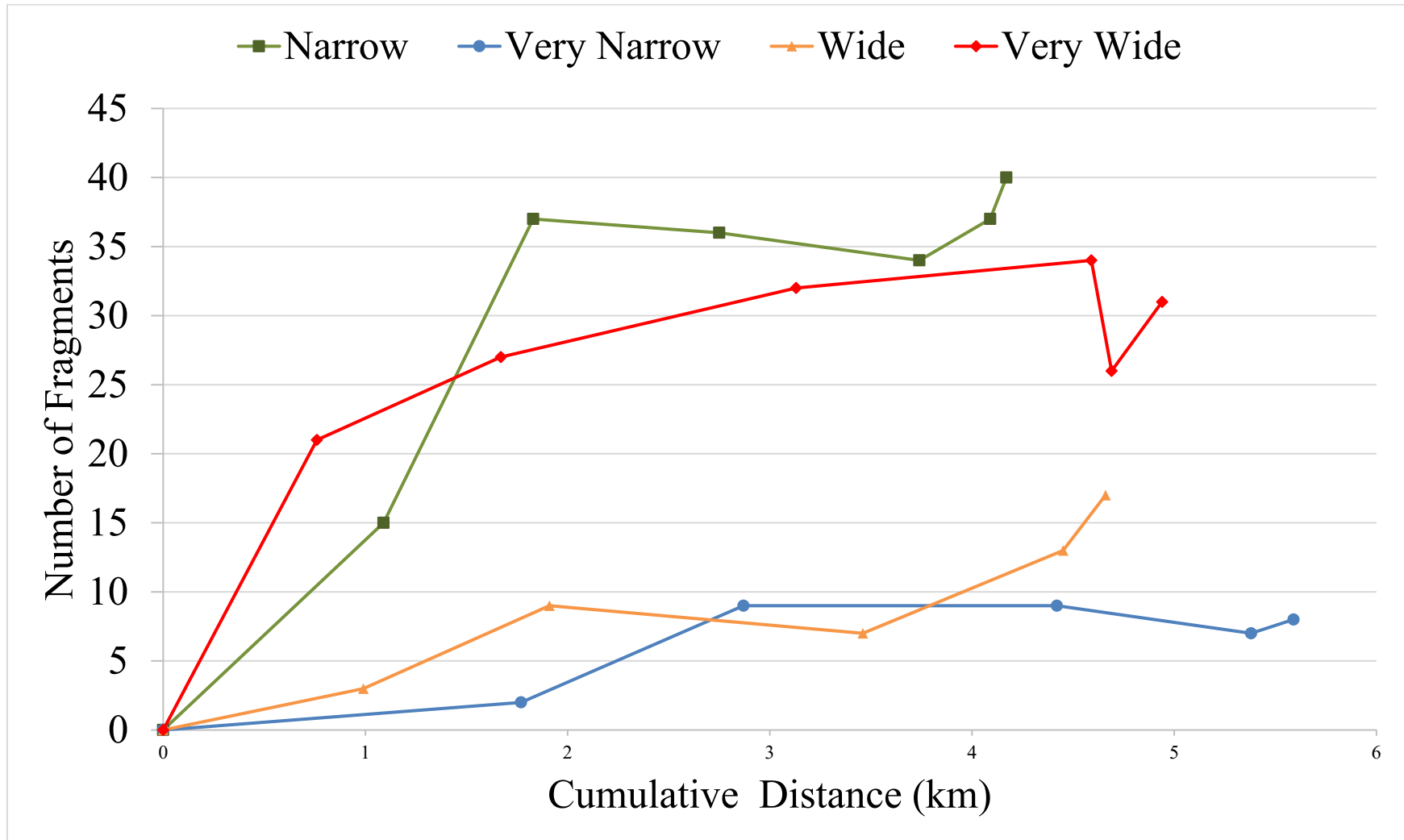


Figure 13. ANOVA and Tukey HSD testing for fragments yields between GSDs

P-Value: 0.000001

There is significant evidence to reject the null hypothesis.

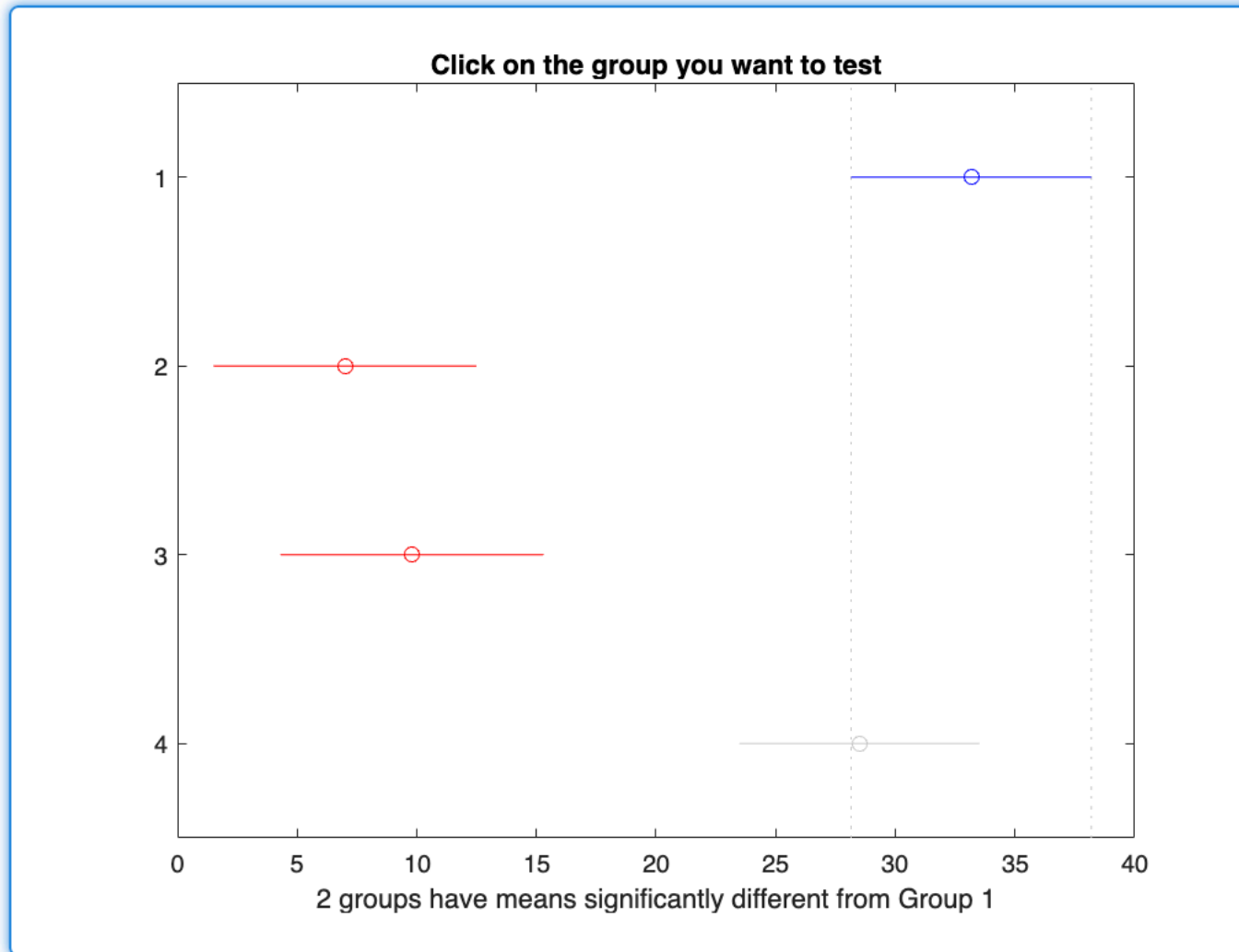


Figure 14. Unsteady state experiment final mass allocation for all GSDs

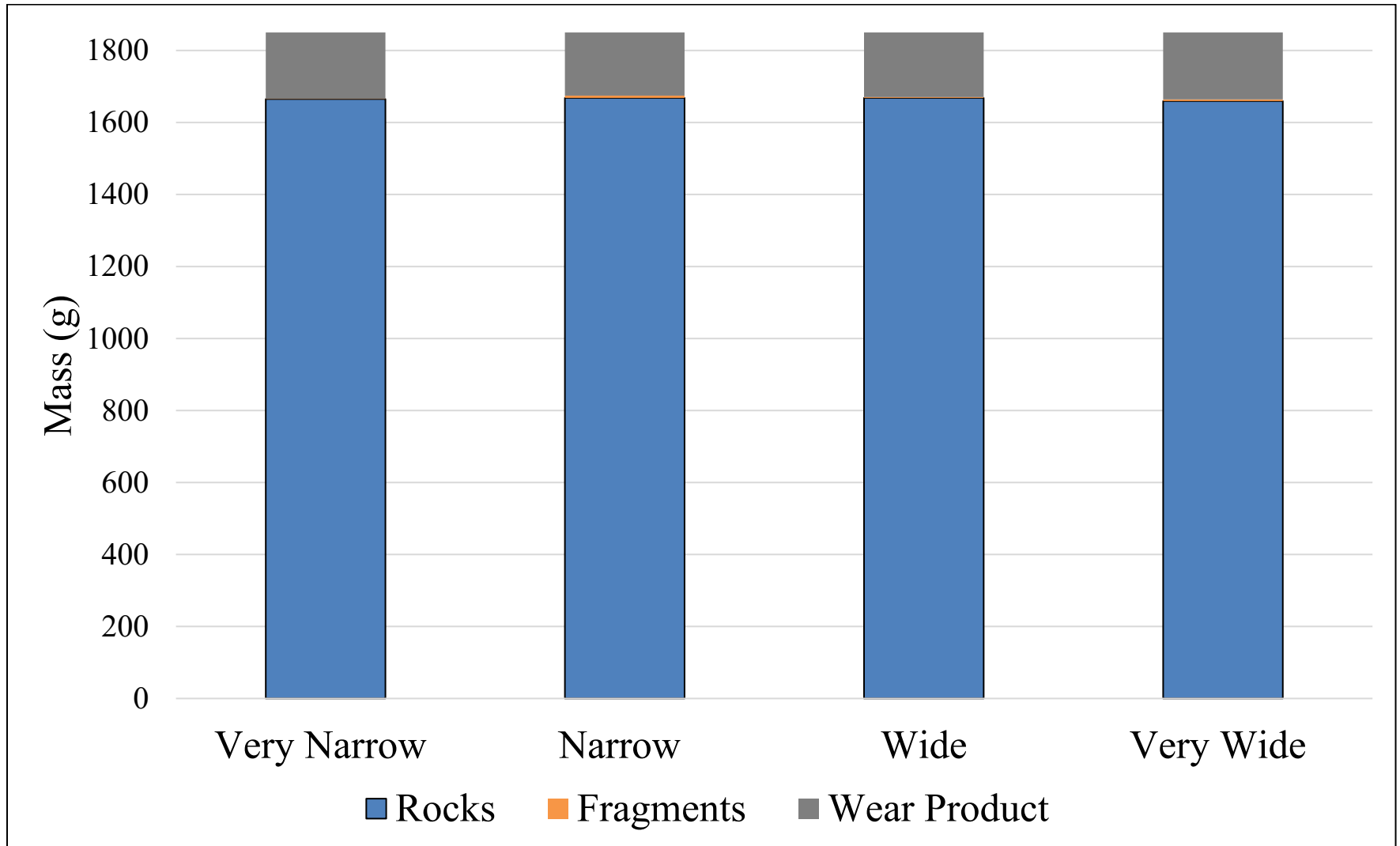


Figure 15. Steady state Experiment fraction less than graph representing particle size distribution

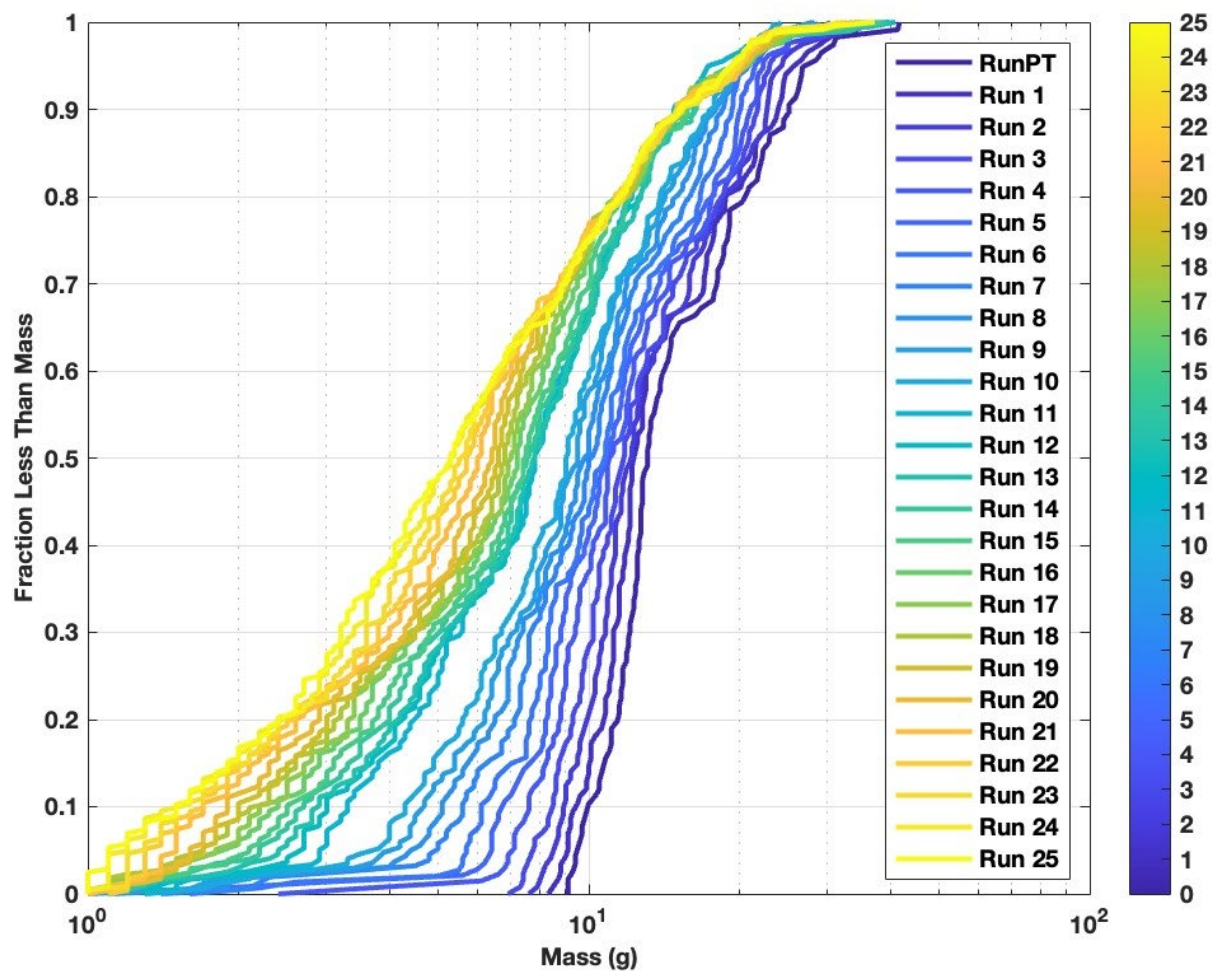


Figure 16. Unsteady steady state experiment average diameter over cumulative travel distance

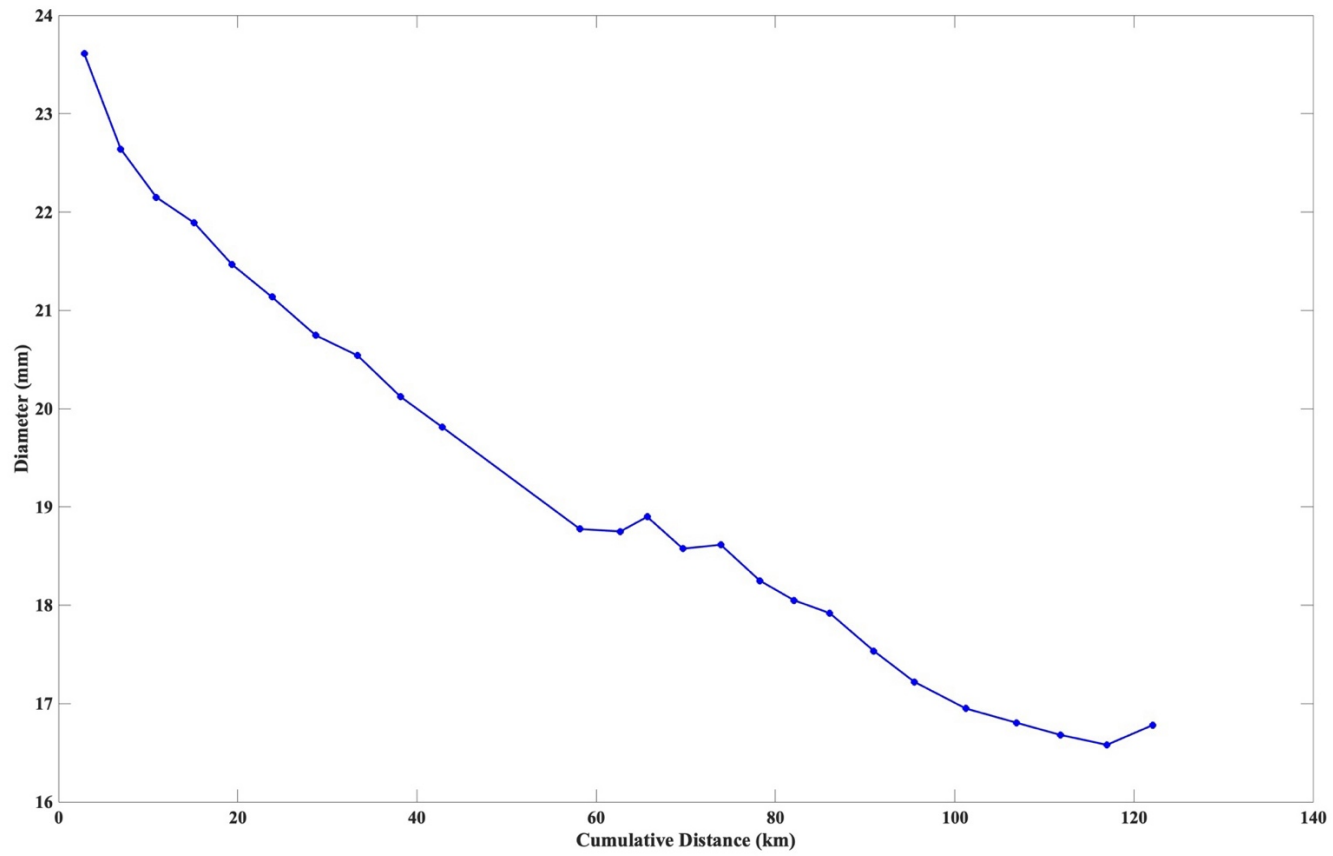


Figure 17. Steady state experiment wear rate over travel distance

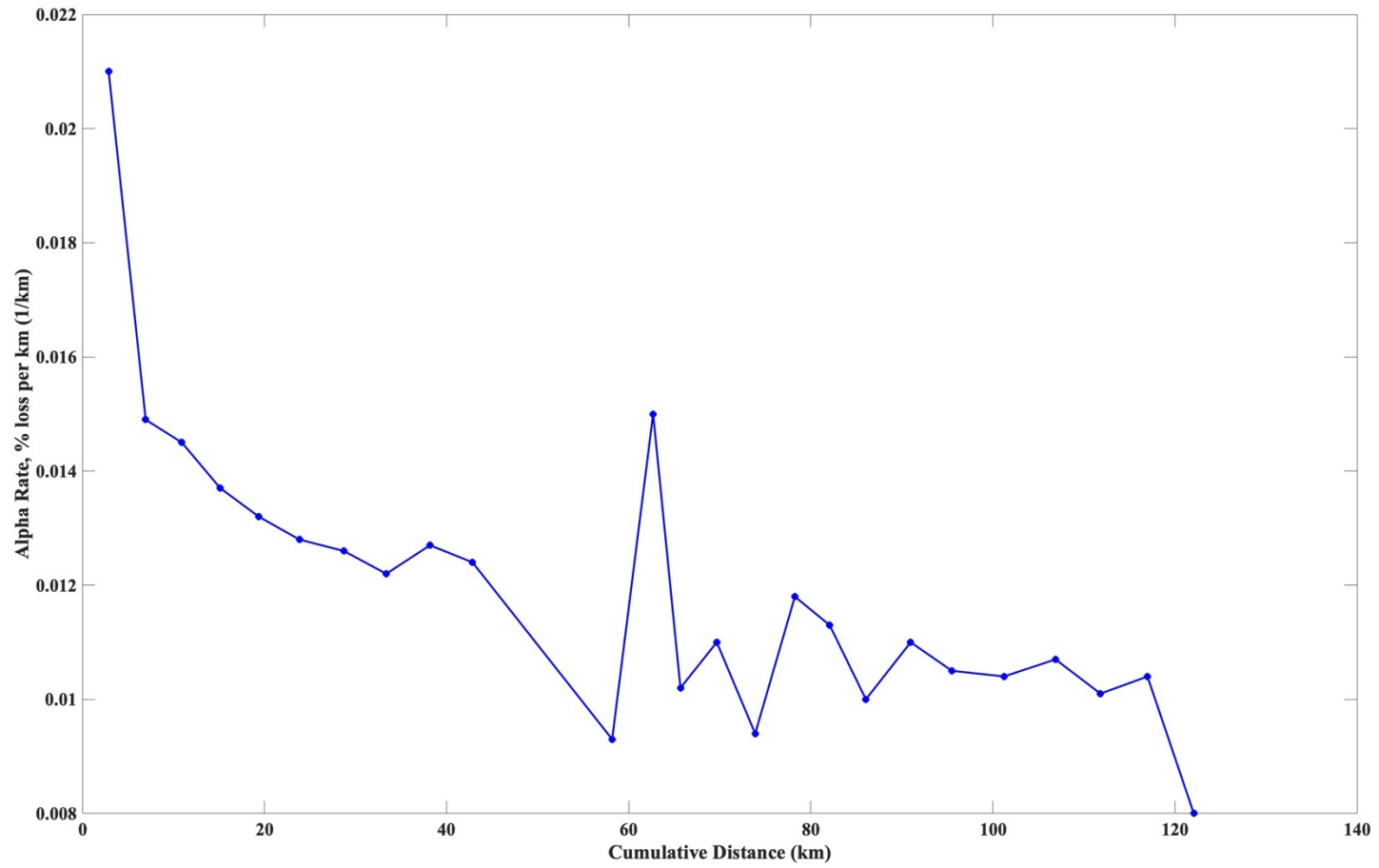


Figure 18. Steady state experiment circularity over cumulative travel distance

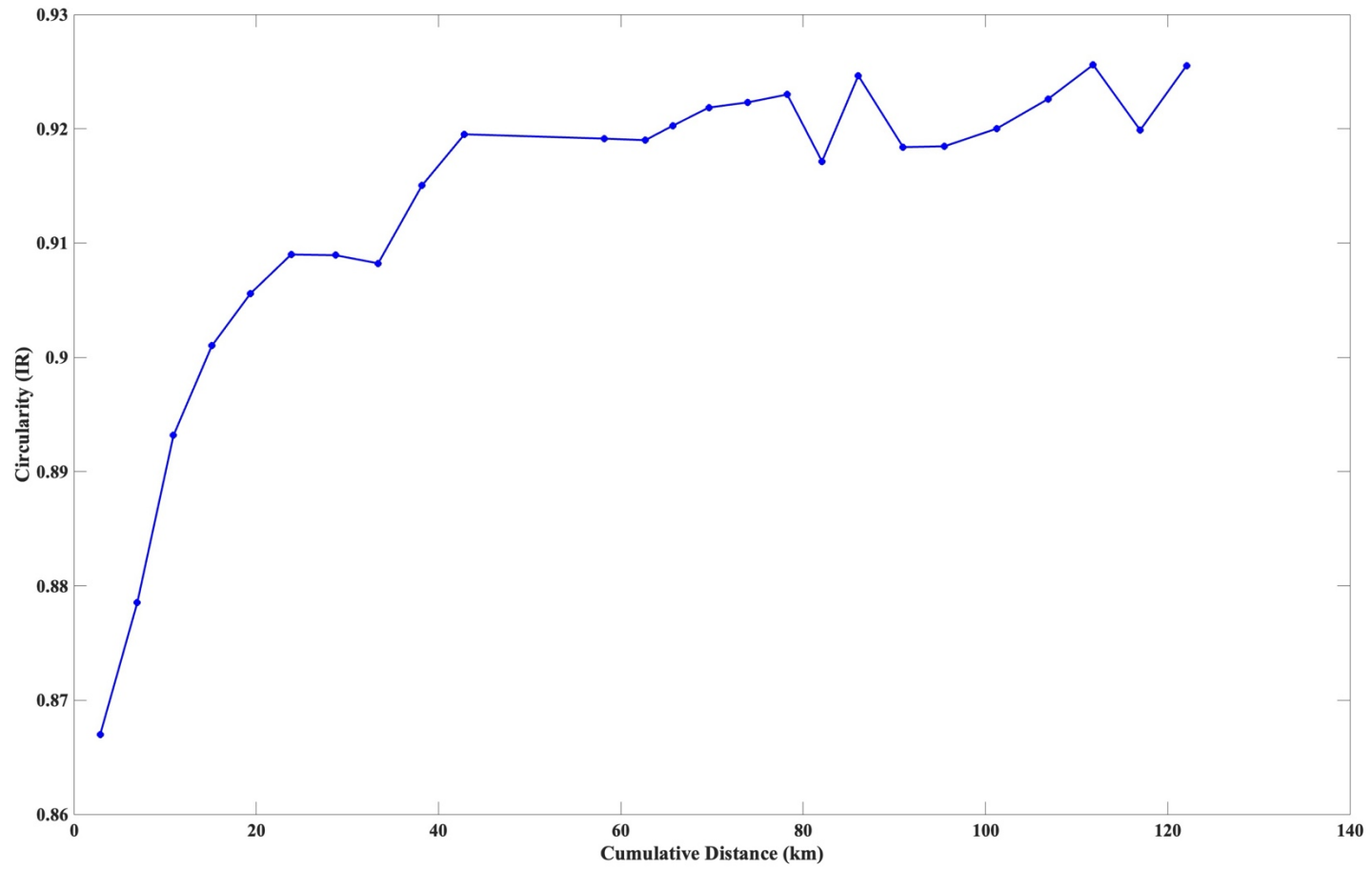


Figure 19. Steady state experiment number of fragments found over cumulative distance traveled

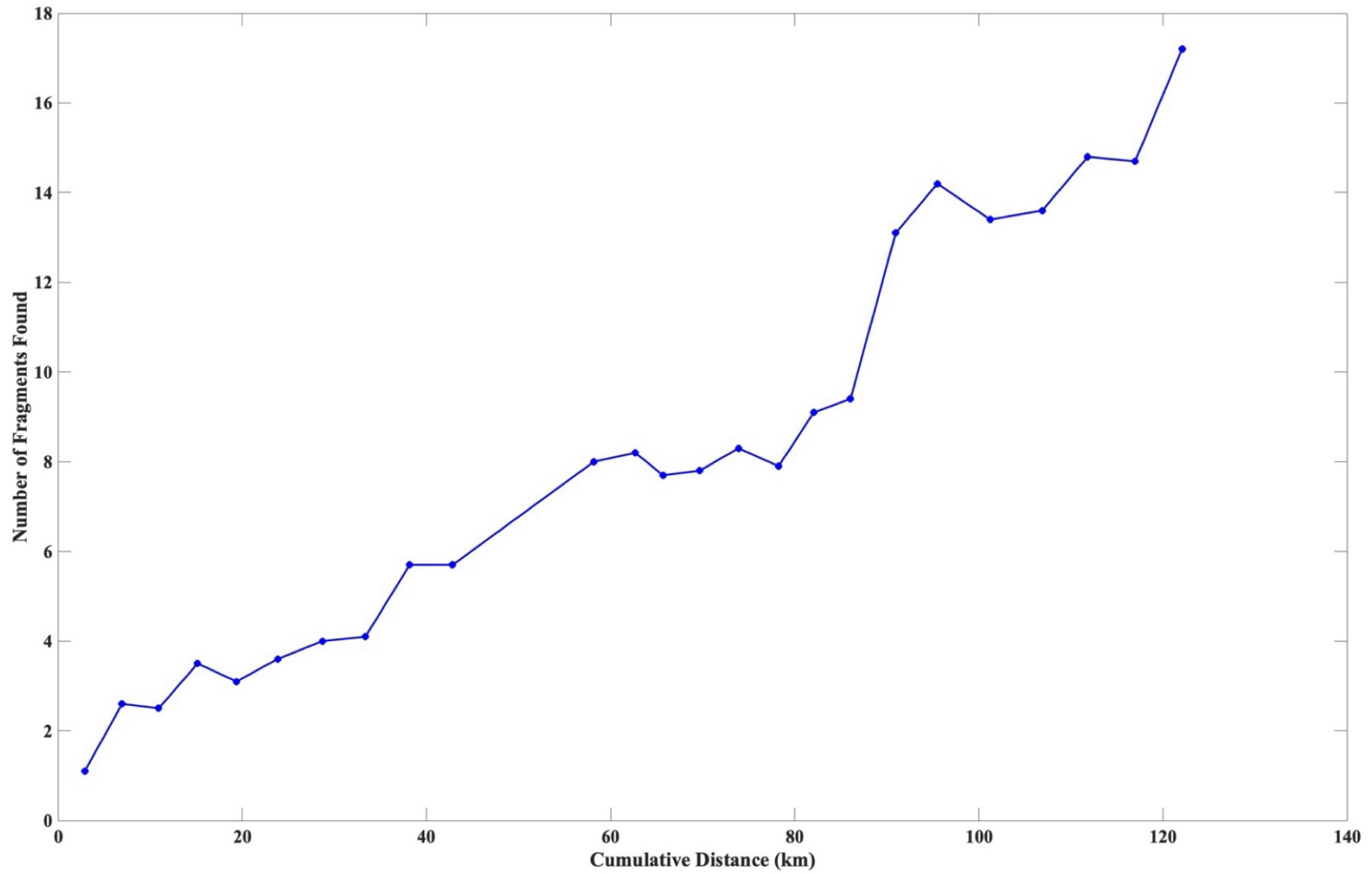


Figure 20. Steady state experiment fine sediment production over travel distance

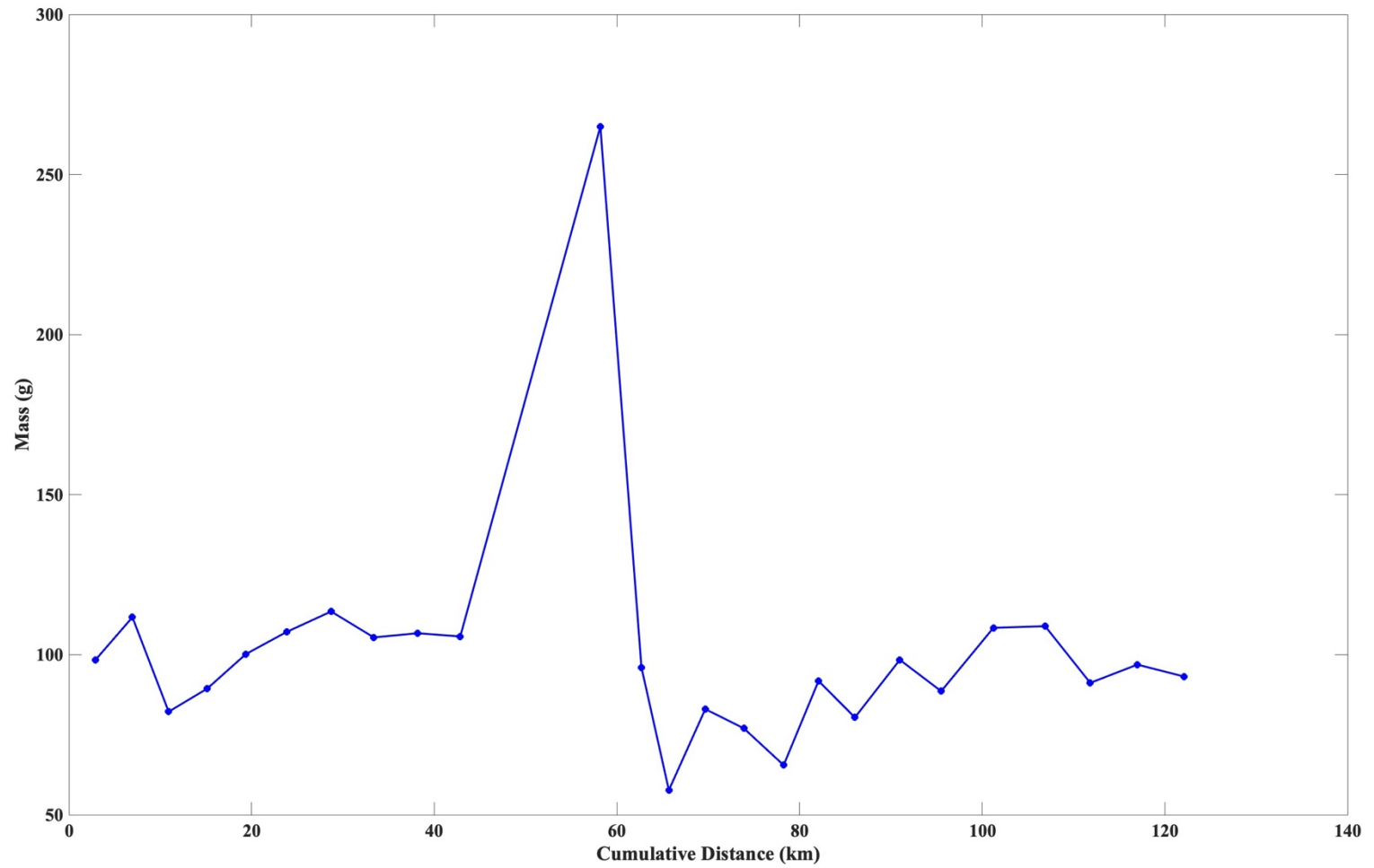


Figure 21. Steady state experiment final mass allocation

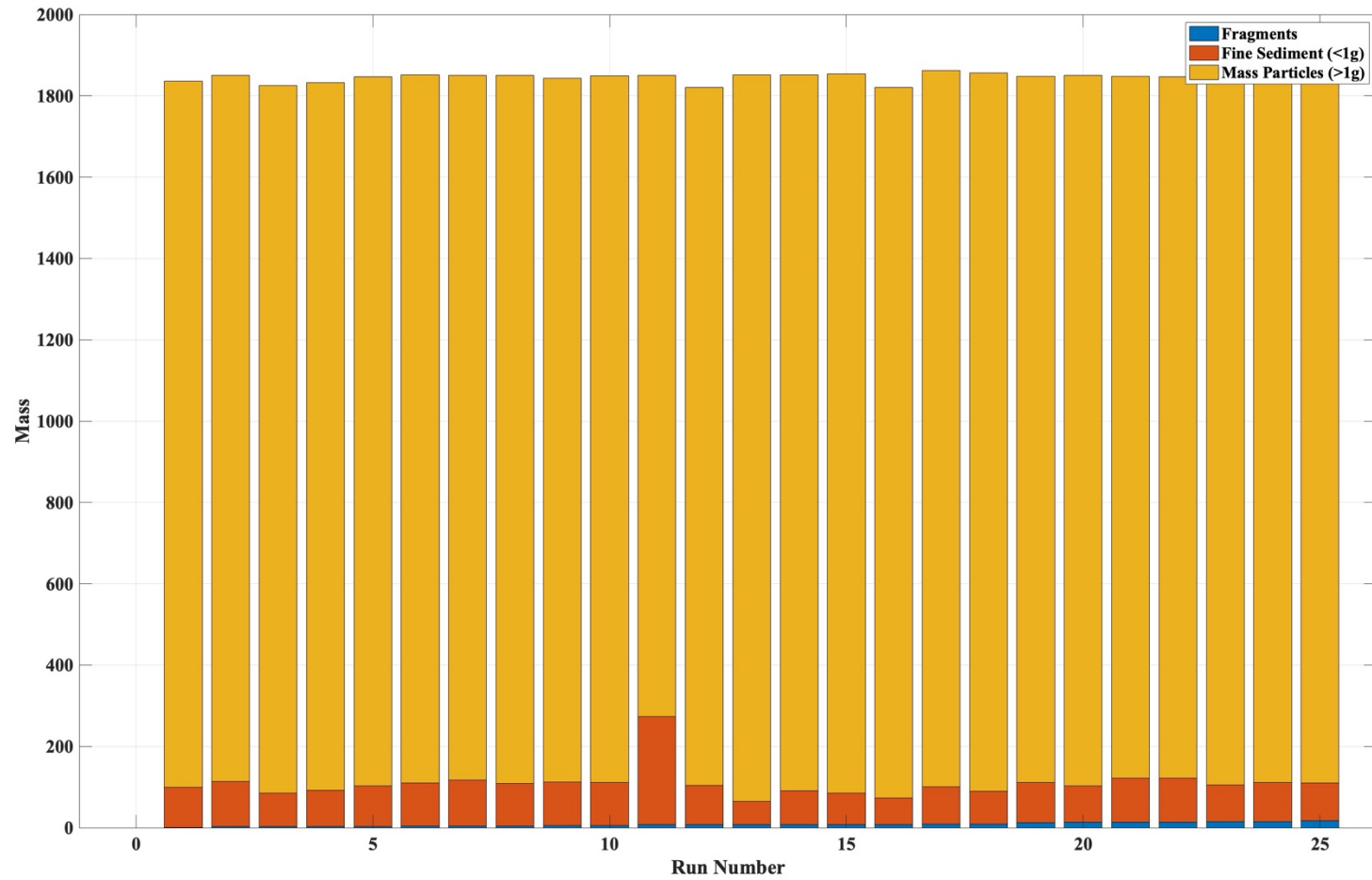


Figure 22. Photo grid station for photo image analysis

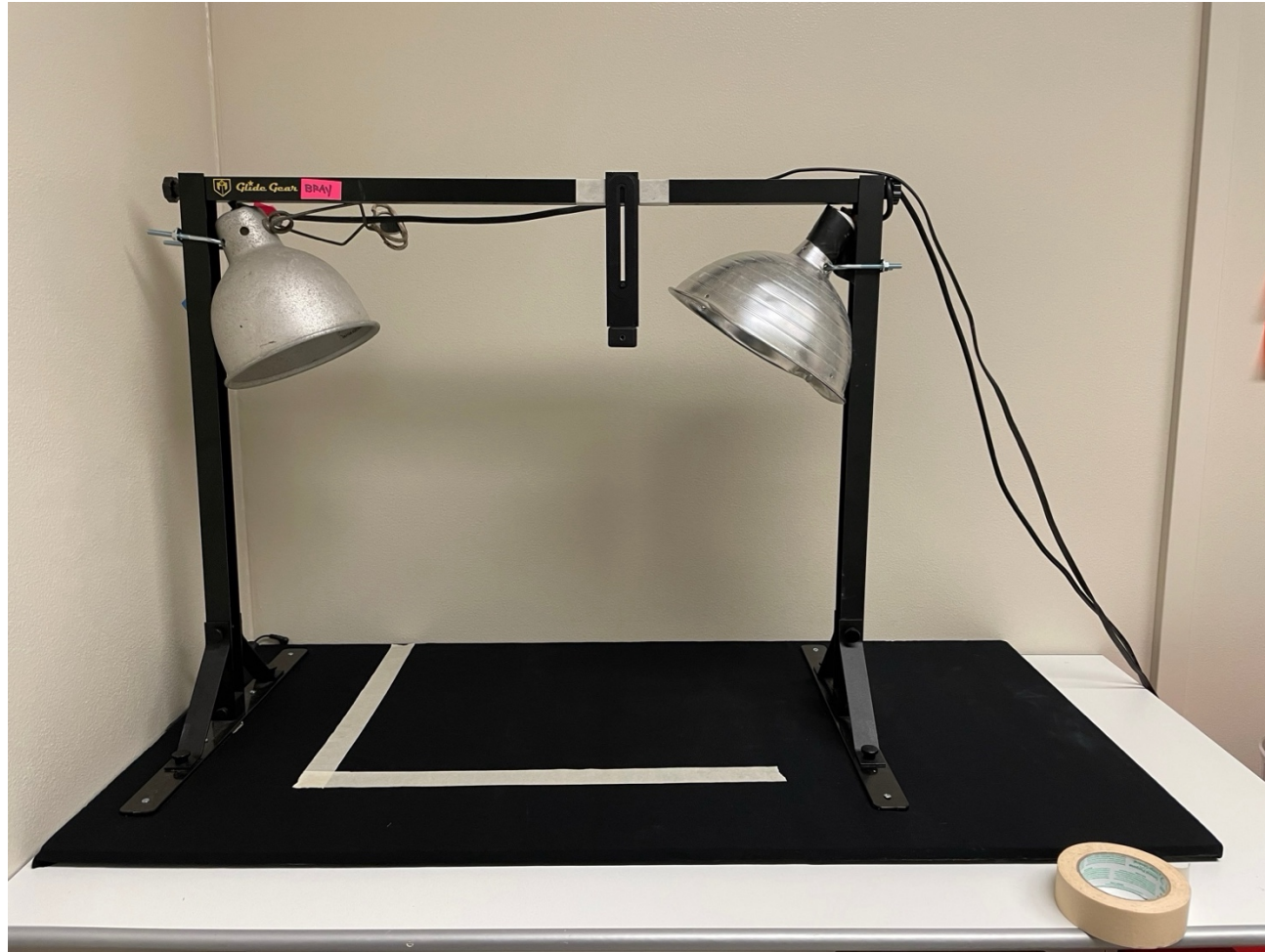


Figure 23. Placement and marker for overhead installation of iPhone 12 Pro camera



Figure 24. Completed photo board with labeled axes and rock grains

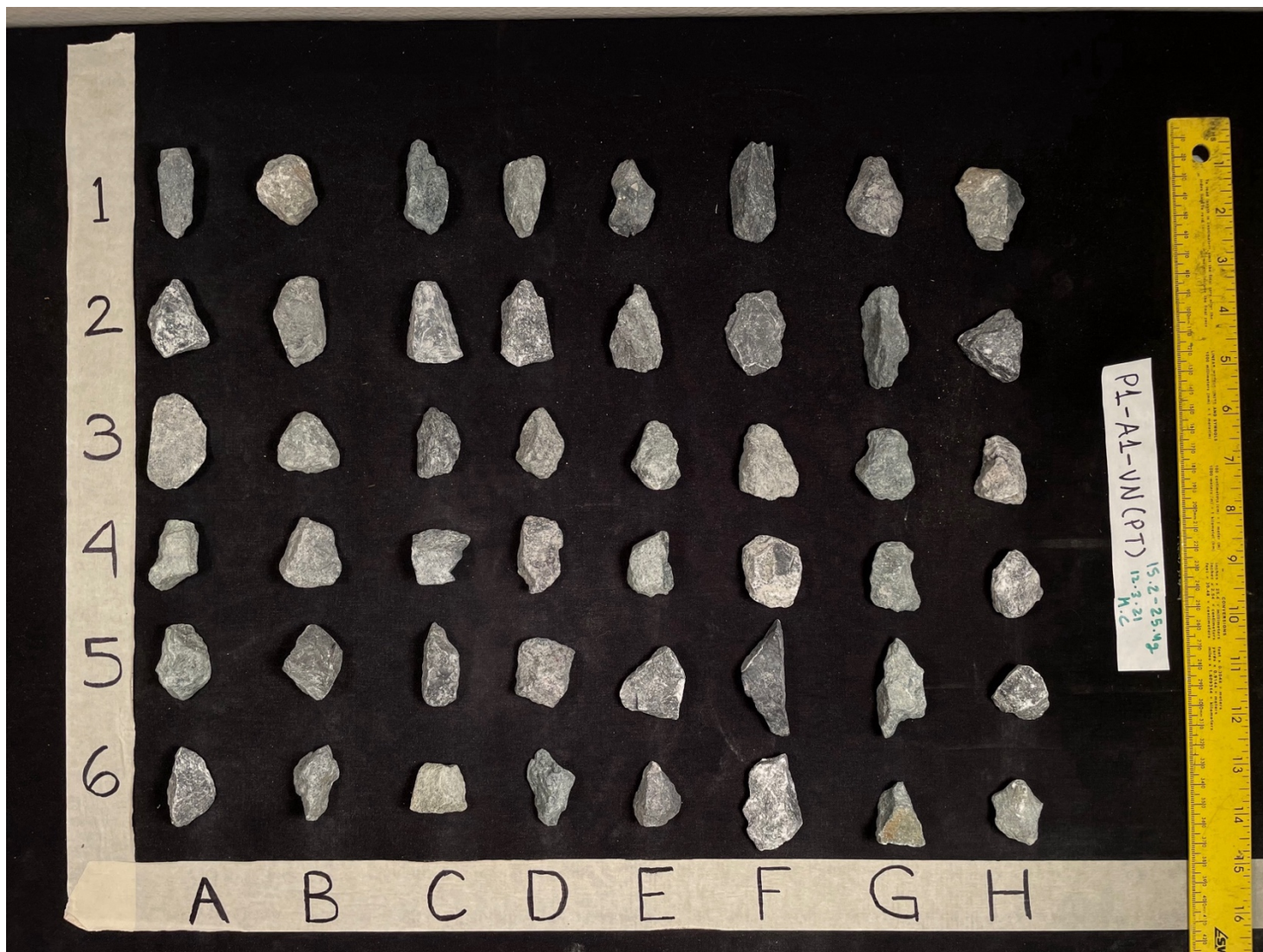


Figure 25. Cropped image with rocks outlined with use of photoshops object detection tool

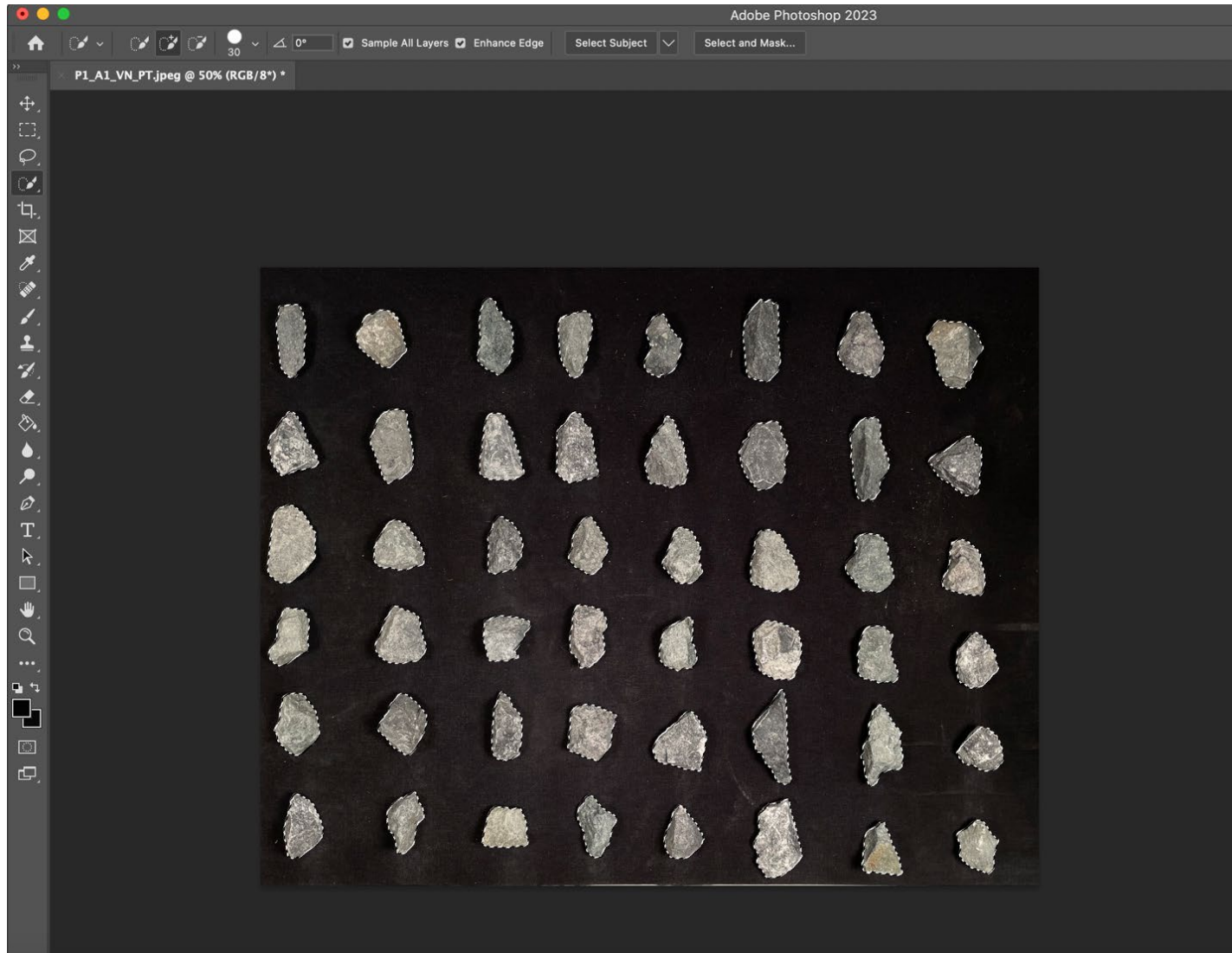


Figure 26. Inverted selection of the object detection tool, showing how everything outside of the rock grain edge is selected preserving edges in future pre processing

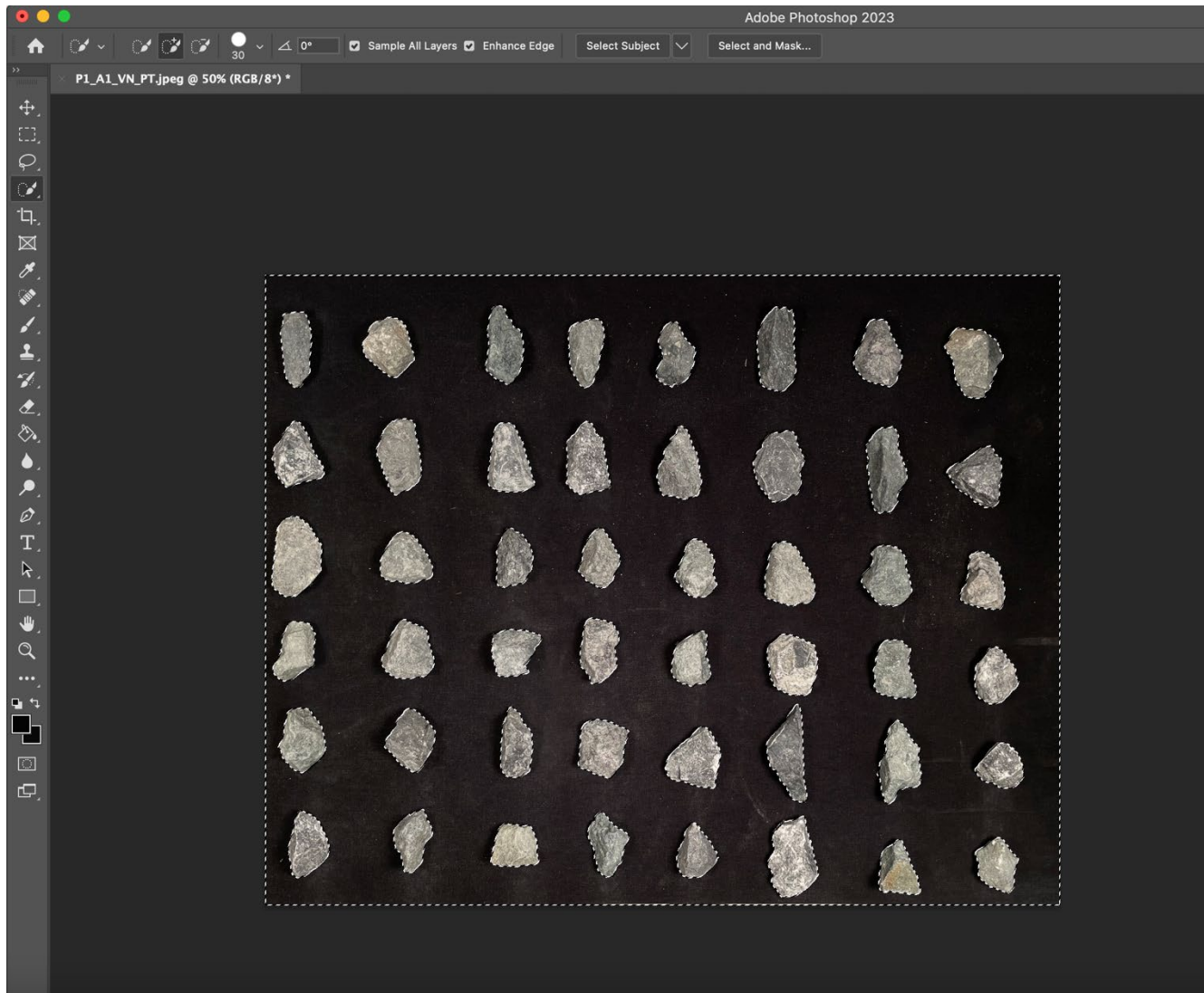


Figure 27. Use of Adobe Photoshop's paintbrush tool to remove background from selected rock grains

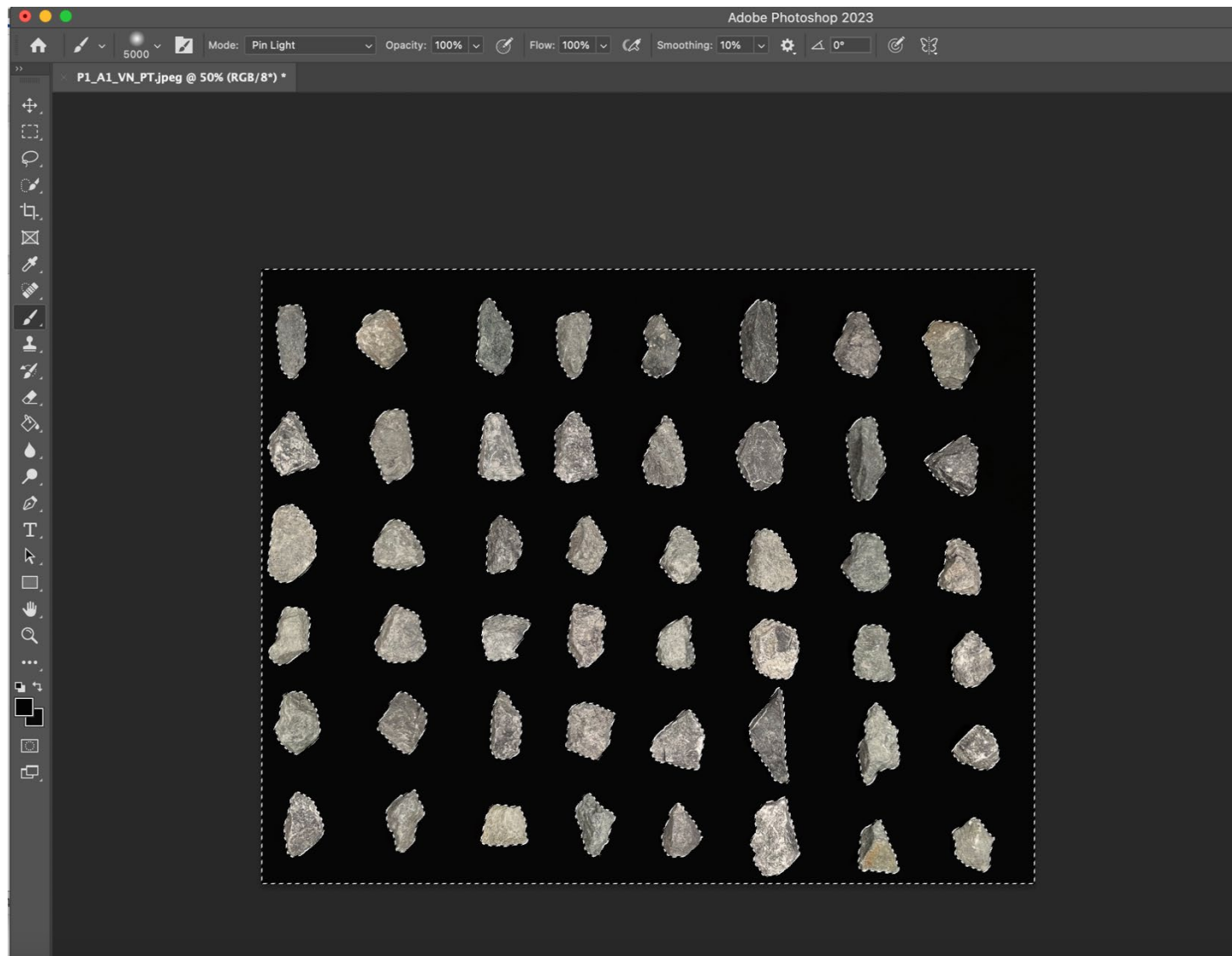


Figure 28. Final high-resolution image exported from Adobe Photoshop

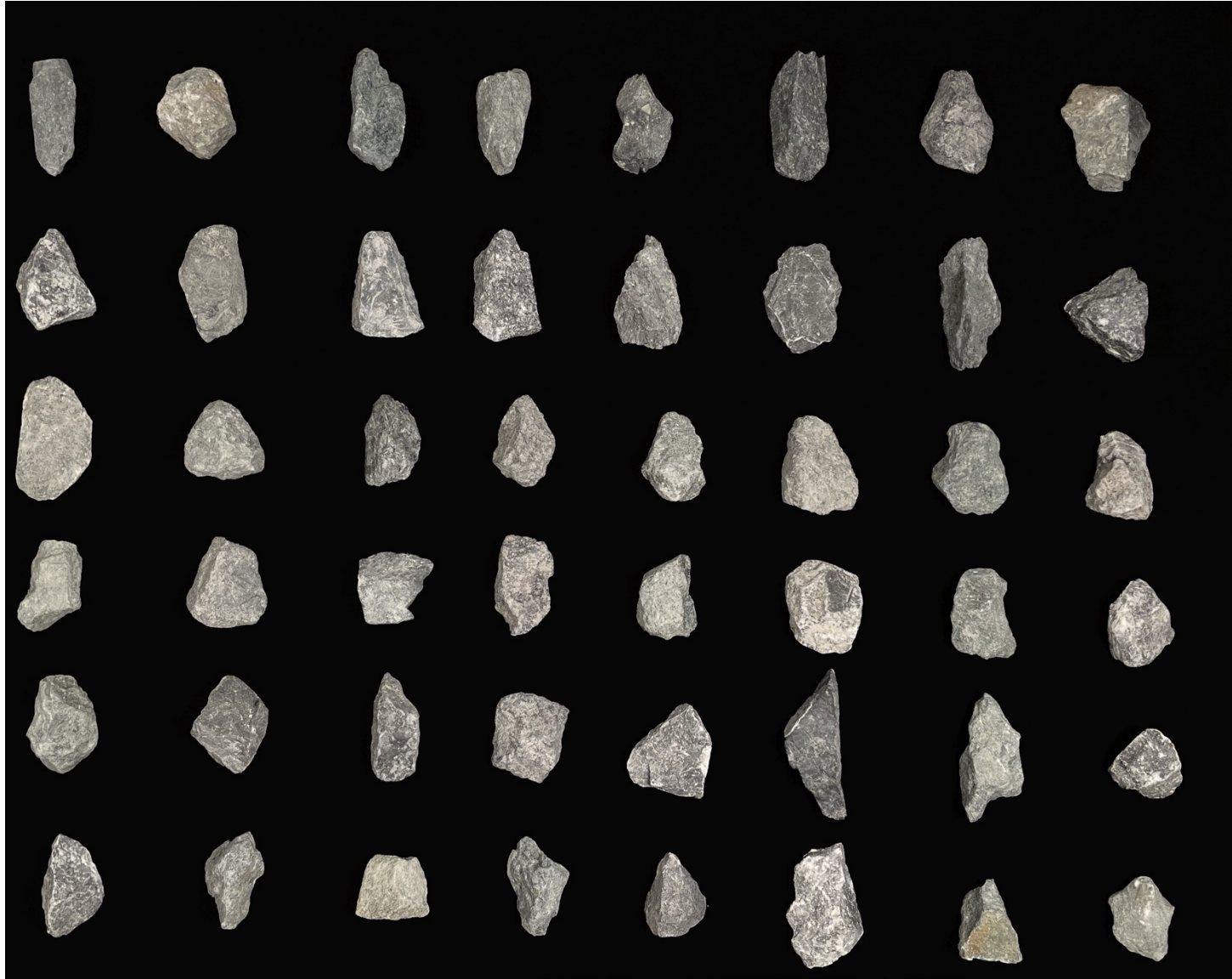


Figure 29. Snapshot of ImageJ's edge detection functionality

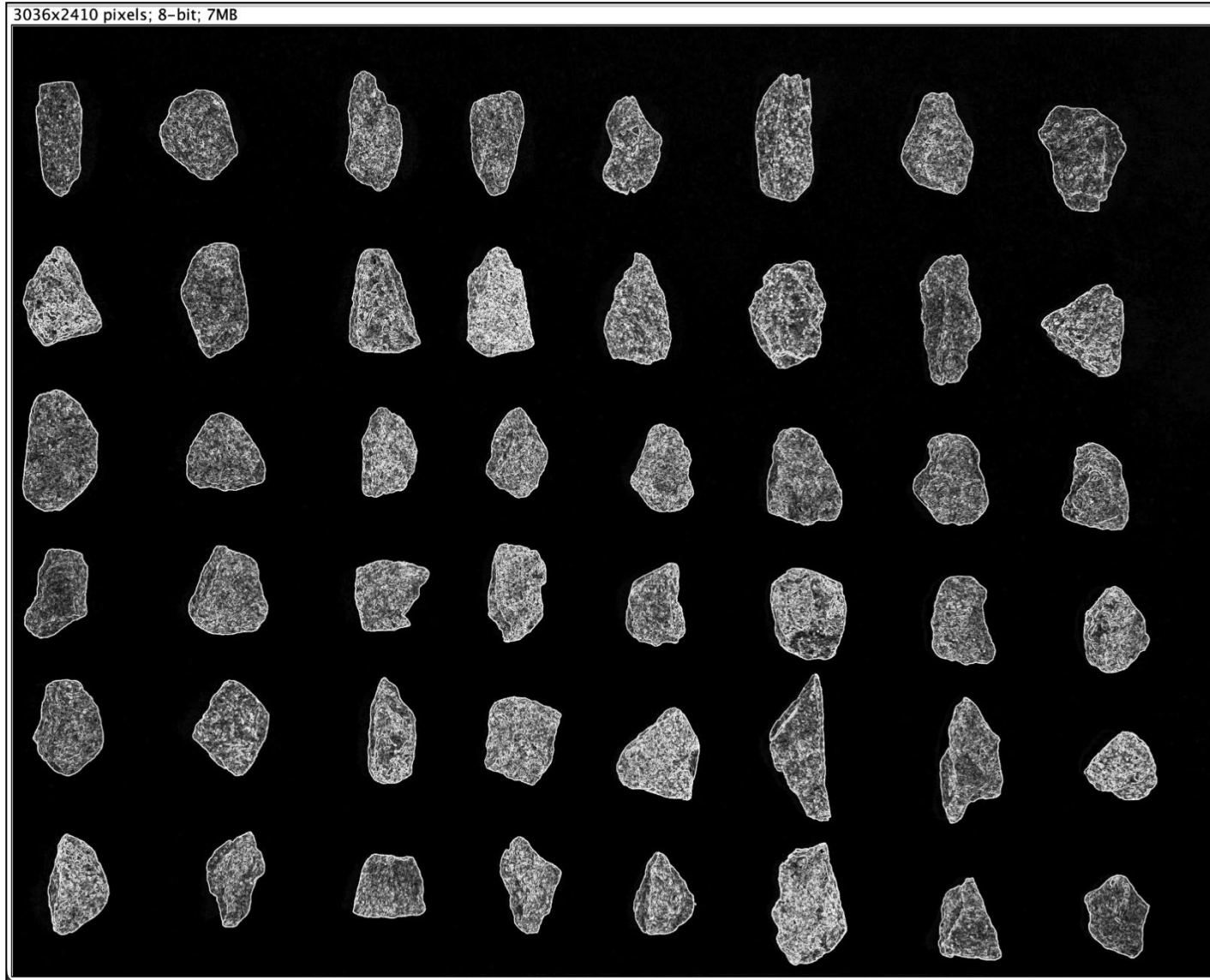


Figure 30. Binary image conversion following use of edge detection tool

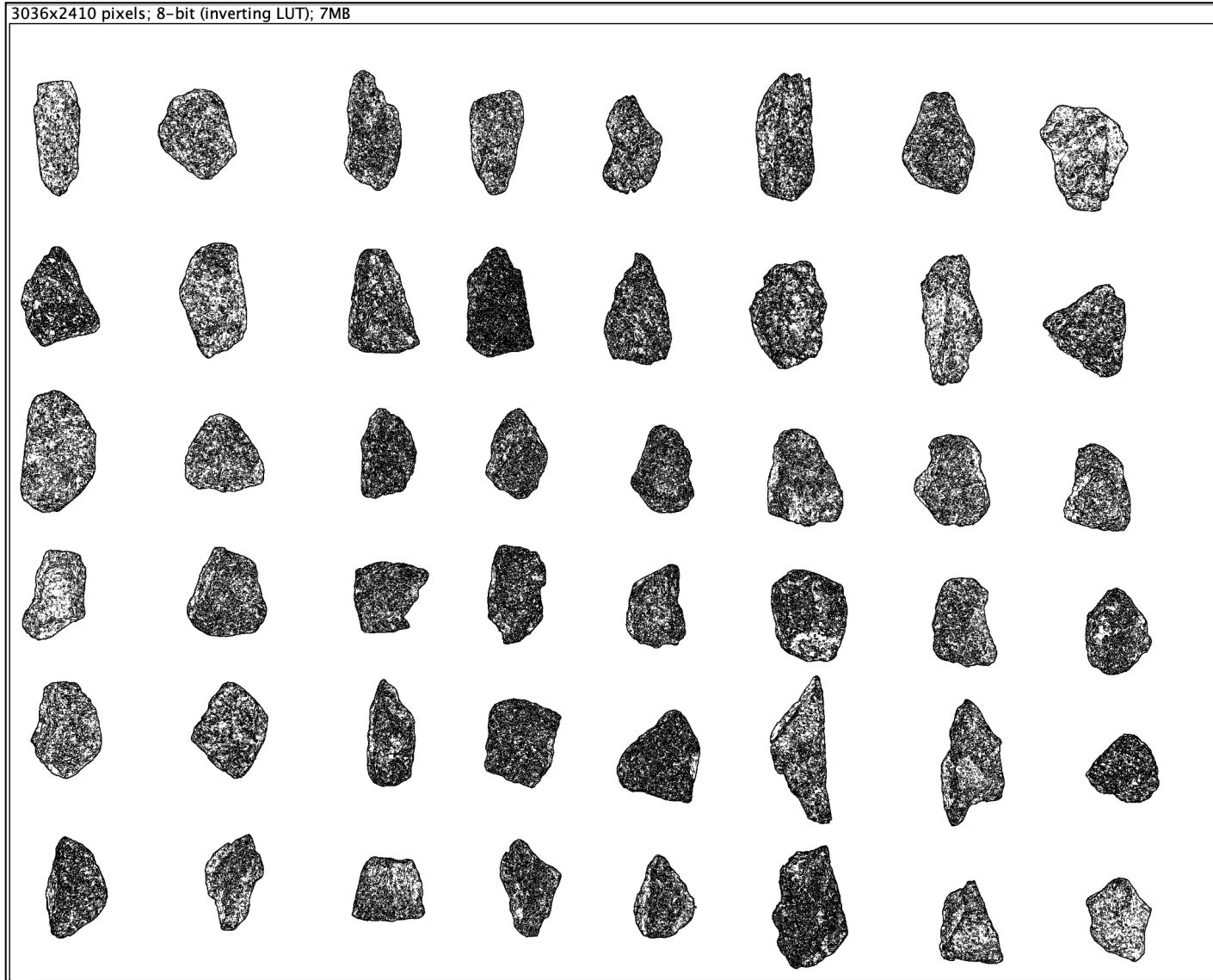


Figure 31. Use of the fill holes function. Note how it maintains crisp edges while filling in particles without the use of thresholding

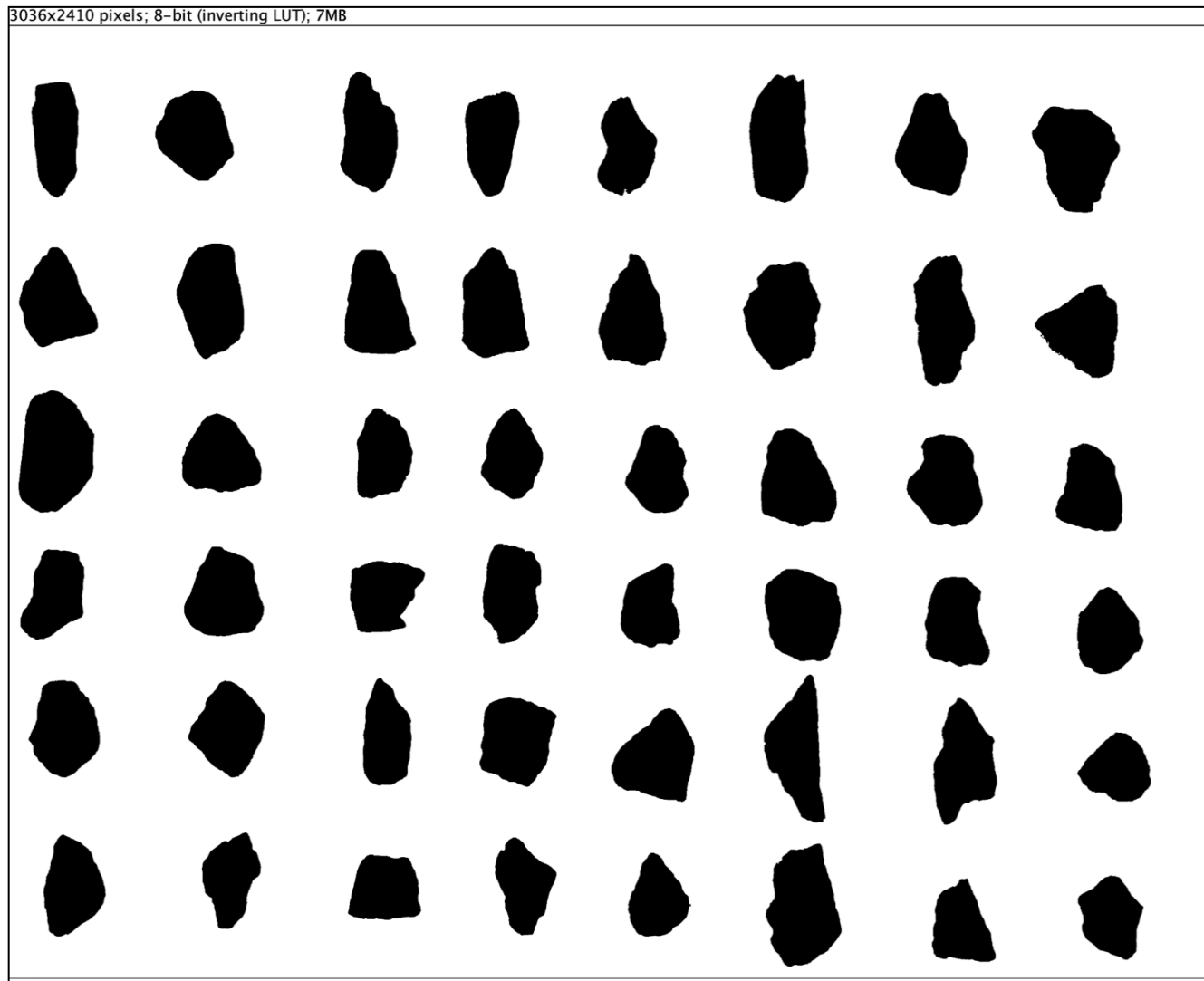


Figure 32. Example of an incomplete filled in rock and use of paint tool for correction

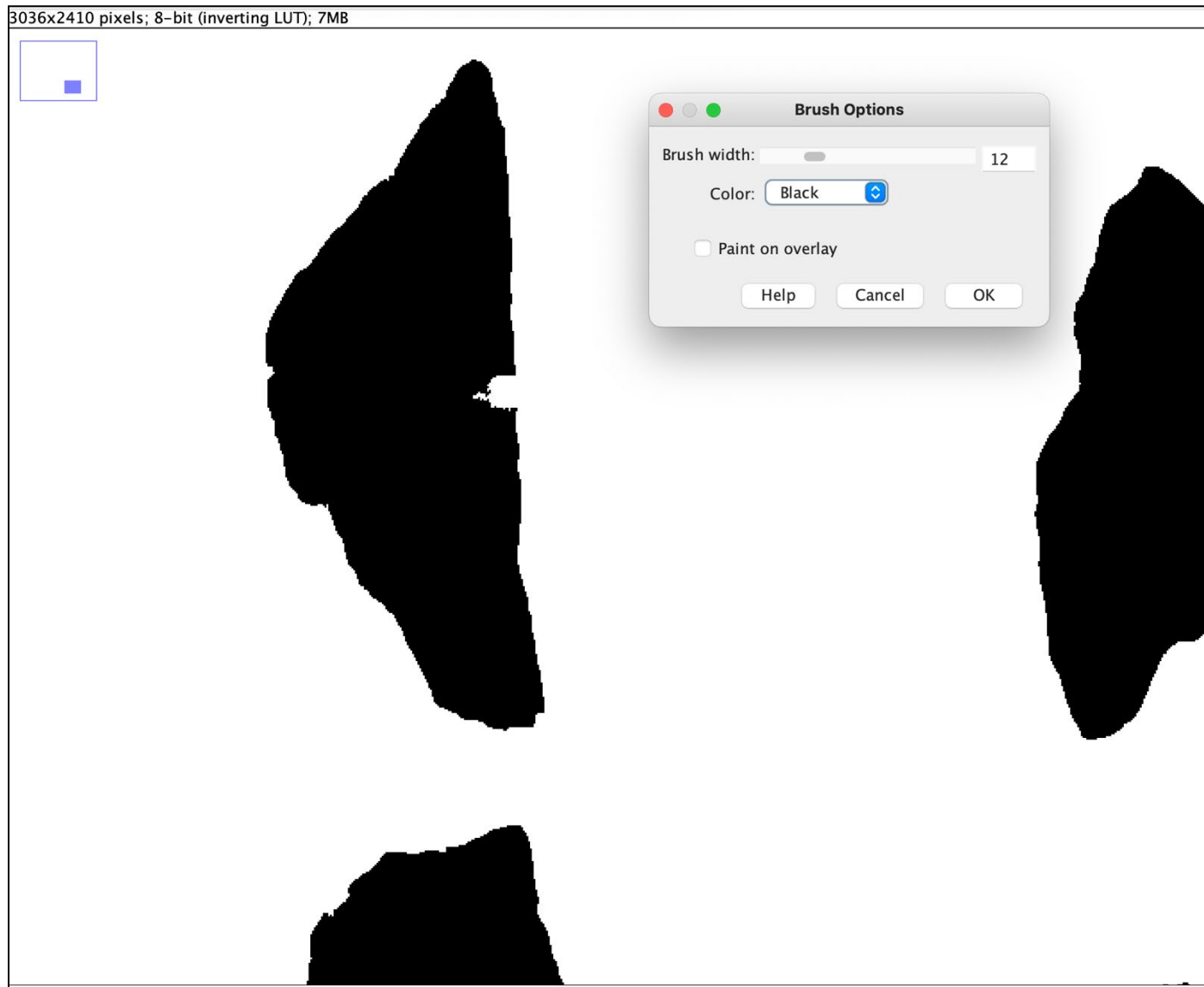


Figure 33. Finalized 8-bit binary image ready for import into the CobbleApp

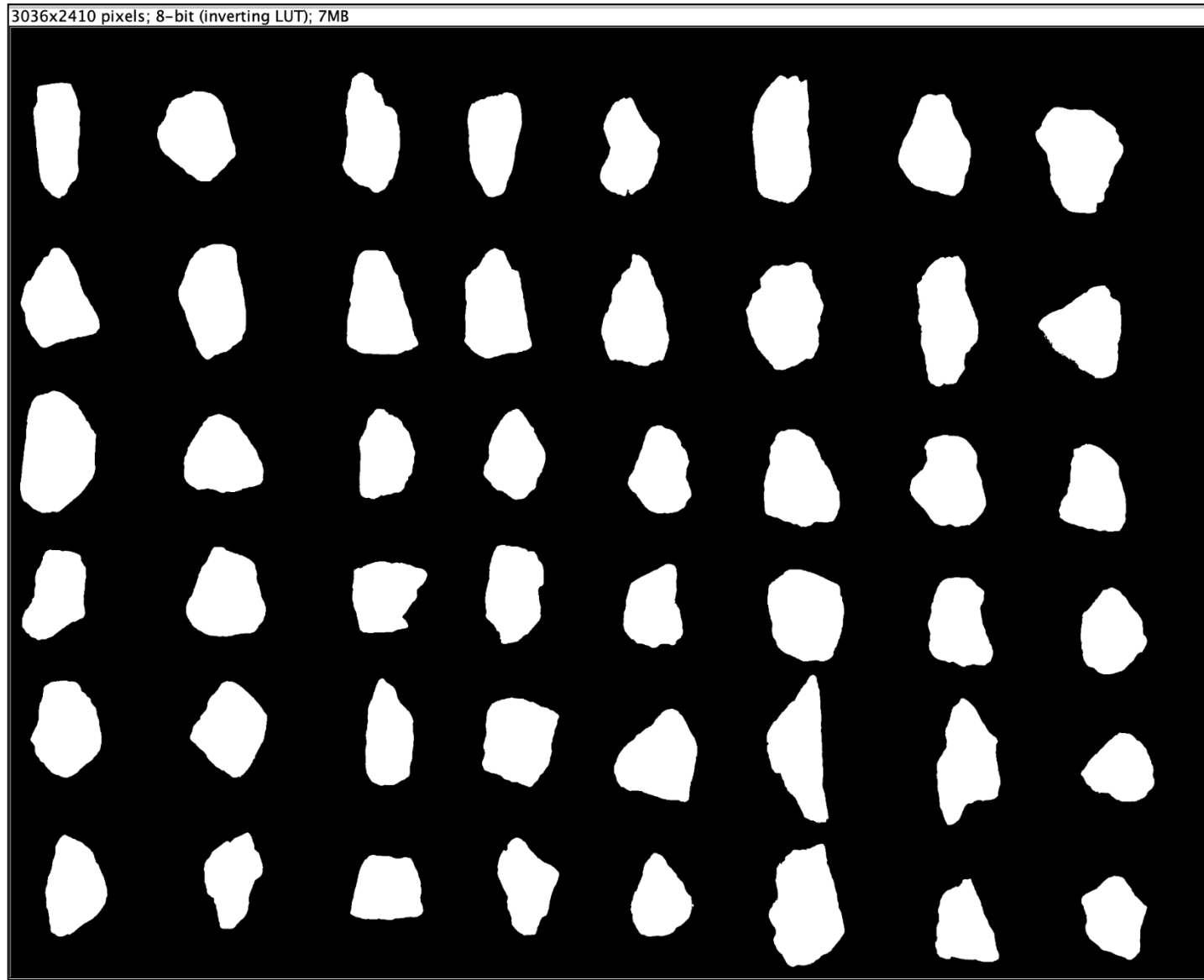


Figure 34. Example of binary photos to the CobbleApp showing use of centroid labelling system and append function

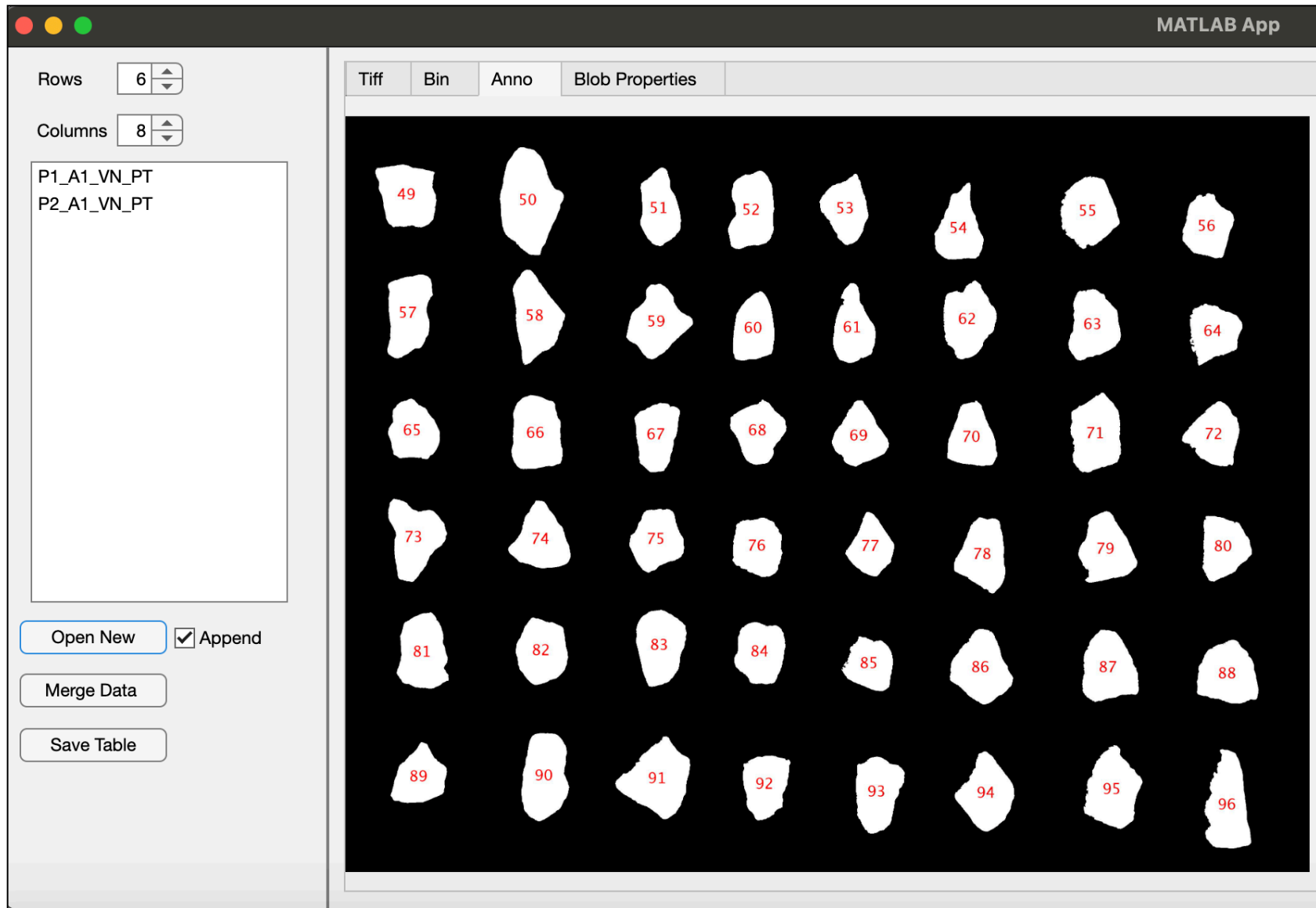


Figure 35. Example of pop-up box for images with less than 48 particles

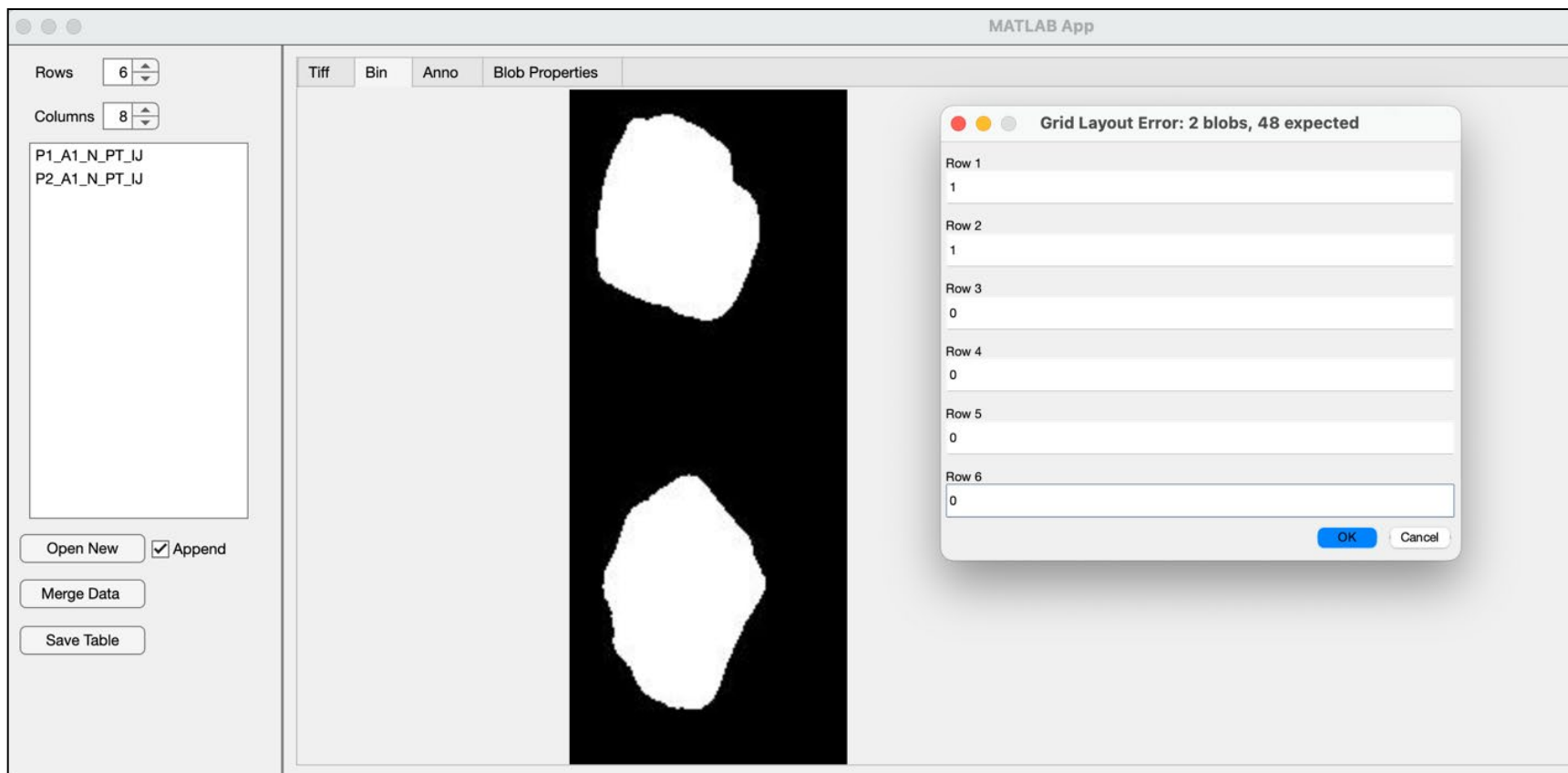


Figure 36. Final database following the use of the merge function via CobbleApp

MATLAB App

Rows: 6
Columns: 8

P1_A1_VN_PT
P2_A1_VN_PT

Open New Append
Merge Data
Save Table

Tiff	Bin	Anno	Blob Properties																
ordinal	grid	gridimage	photo	srange	run	row	col	alphanum	measureID	x	y	Area	MajorAxisLength	MinorAxisLength	Eccentricity	Circularity	Equ		
1	1	P1_A1_VN_PT	P1	VN	PT	1	1	A1	P1_A1_VN_PT	125.5102	249.9633	27843	304.2671	118.2734	0.9214	0.6946			
2	1	P1_A1_VN_PT	P1	VN	PT	1	2	B1	P1_B1_VN_PT	480.2960	247.0294	32004	225.3016	183.2513	0.5818	0.9061			
3	1	P1_A1_VN_PT	P1	VN	PT	1	3	C1	P1_C1_VN_PT	918.6926	249.1585	31767	297.3873	140.5226	0.8813	0.7137			
4	1	P1_A1_VN_PT	P1	VN	PT	1	4	D1	P1_D1_VN_PT	1.2319e+03	259.5662	27566	269.5288	134.6995	0.8662	0.7621			
5	1	P1_A1_VN_PT	P1	VN	PT	1	5	E1	P1_E1_VN_PT	1.5720e+03	283.5064	25927	248.7043	140.1606	0.8261	0.7387			
6	1	P1_A1_VN_PT	P1	VN	PT	1	6	F1	P1_F1_VN_PT	1.9627e+03	259.4196	39621	337.6476	151.8732	0.8931	0.7163			
7	1	P1_A1_VN_PT	P1	VN	PT	1	7	G1	P1_G1_VN_PT	2.3506e+03	279.3267	33335	255.3164	171.8643	0.7395	0.8381			
8	1	P1_A1_VN_PT	P1	VN	PT	1	8	H1	P1_H1_VN_PT	2.7149e+03	299.8239	41147	275.6071	197.3660	0.6980	0.8157			
9	1	P1_A1_VN_PT	P1	VN	PT	2	1	A2	P1_A2_VN_PT	125.7673	671.3787	31992	240.3169	179.7285	0.6638	0.8055			
10	1	P1_A1_VN_PT	P1	VN	PT	2	2	B2	P1_B2_VN_PT	522.5993	664.0674	36794	291.6170	162.7916	0.8297	0.8216			
11	1	P1_A1_VN_PT	P1	VN	PT	2	3	C2	P1_C2_VN_PT	938.7111	686.6809	34676	283.8799	164.7803	0.8143	0.7754			
12	1	P1_A1_VN_PT	P1	VN	PT	2	4	D2	P1_D2_VN_PT	1.2358e+03	686.5730	35229	279.4379	165.9436	0.8046	0.7768			
13	1	P1_A1_VN_PT	P1	VN	PT	2	5	E2	P1_E2_VN_PT	1.5916e+03	710.6032	33364	273.6605	162.6431	0.8042	0.7433			
14	1	P1_A1_VN_PT	P1	VN	PT	2	6	F2	P1_F2_VN_PT	1.9716e+03	703.8298	39428	271.8913	186.3533	0.7282	0.8436			
15	1	P1_A1_VN_PT	P1	VN	PT	2	7	G2	P1_G2_VN_PT	2.3763e+03	715.9930	37335	336.0266	144.5302	0.9028	0.6547			
16	1	P1_A1_VN_PT	P1	VN	PT	2	8	H2	P1_H2_VN_PT	2.7356e+03	744.3298	31841	220.1510	198.6934	0.4306	0.7323			
17	1	P1_A1_VN_PT	P1	VN	PT	3	1	A3	P1_A3_VN_PT	123.1301	1.0534e...	45487	311.6652	189.5081	0.7939	0.8578			
18	1	P1_A1_VN_PT	P1	VN	PT	3	2	B3	P1_B3_VN_PT	543.2145	1.0649e...	29157	203.4365	189.5791	0.3628	0.8880			
19	1	P1_A1_VN_PT	P1	VN	PT	3	3	C3	P1_C3_VN_PT	955.2285	1.0601e...	24718	227.0095	141.8446	0.7808	0.8189			
20	1	P1_A1_VN_PT	P1	VN	PT	3	4	D3	P1_D3_VN_PT	1.2841e+03	1.0619e...	24365	218.6122	144.4029	0.7508	0.8393			
21	1	P1_A1_VN_PT	P1	VN	PT	3	5	E3	P1_E3_VN_PT	1.6560e+03	1.1020e...	25392	225.6531	147.0817	0.7584	0.8334			
22	1	P1_A1_VN_PT	P1	VN	PT	3	6	F3	P1_F3_VN_PT	2.0050e+03	1.1262e...	35418	255.3003	183.2007	0.6965	0.8443			

Figure 37. Comparing mean circularity values of the same photo of raw image. (Left) raw image processed in ImageJ only, (right) raw image preprocessed using photoshop and subsequently imported into ImageJ.

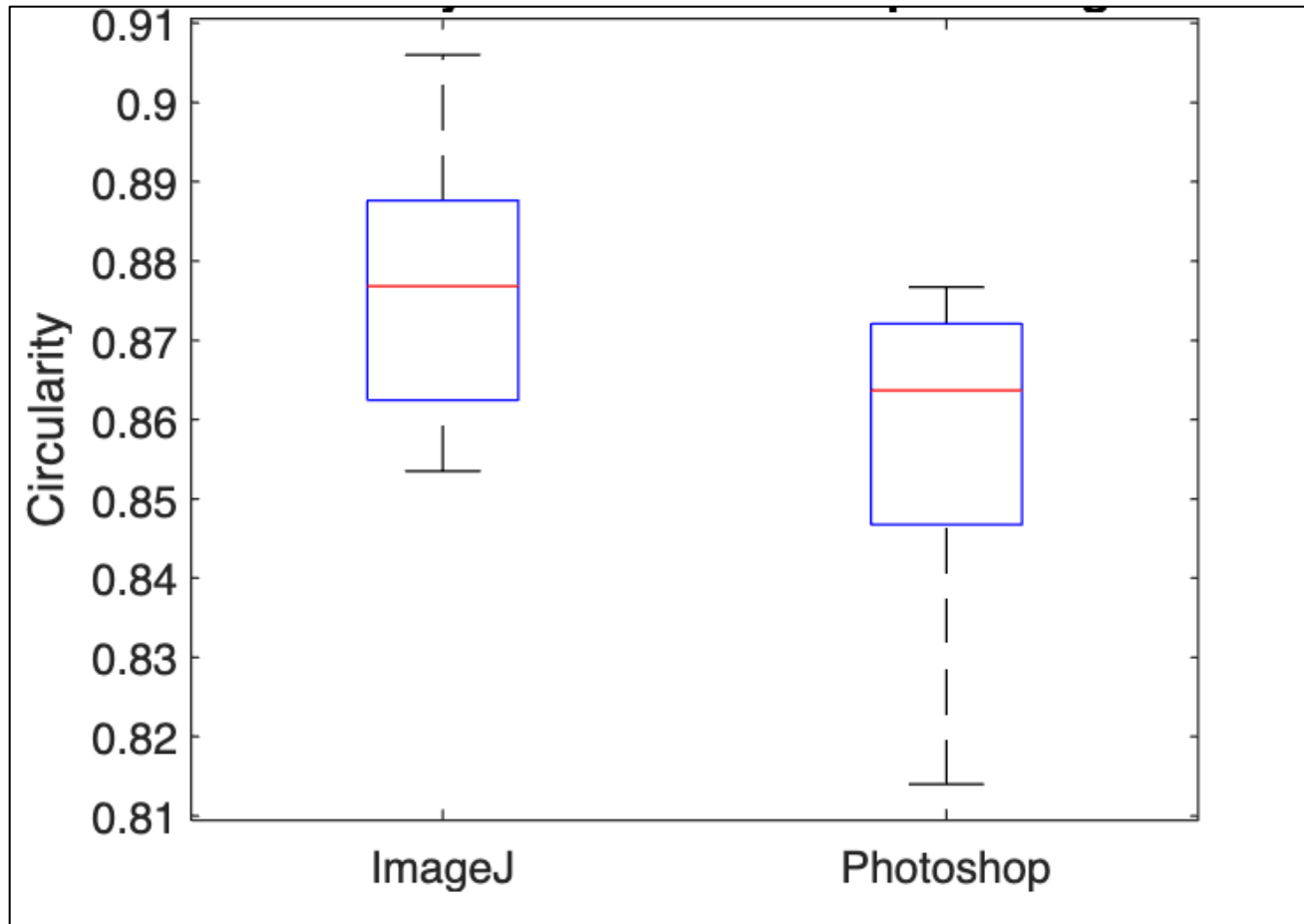


Figure 38. Boxplot of average circularity values from five random test images comparing Method 2 at 100% resolution

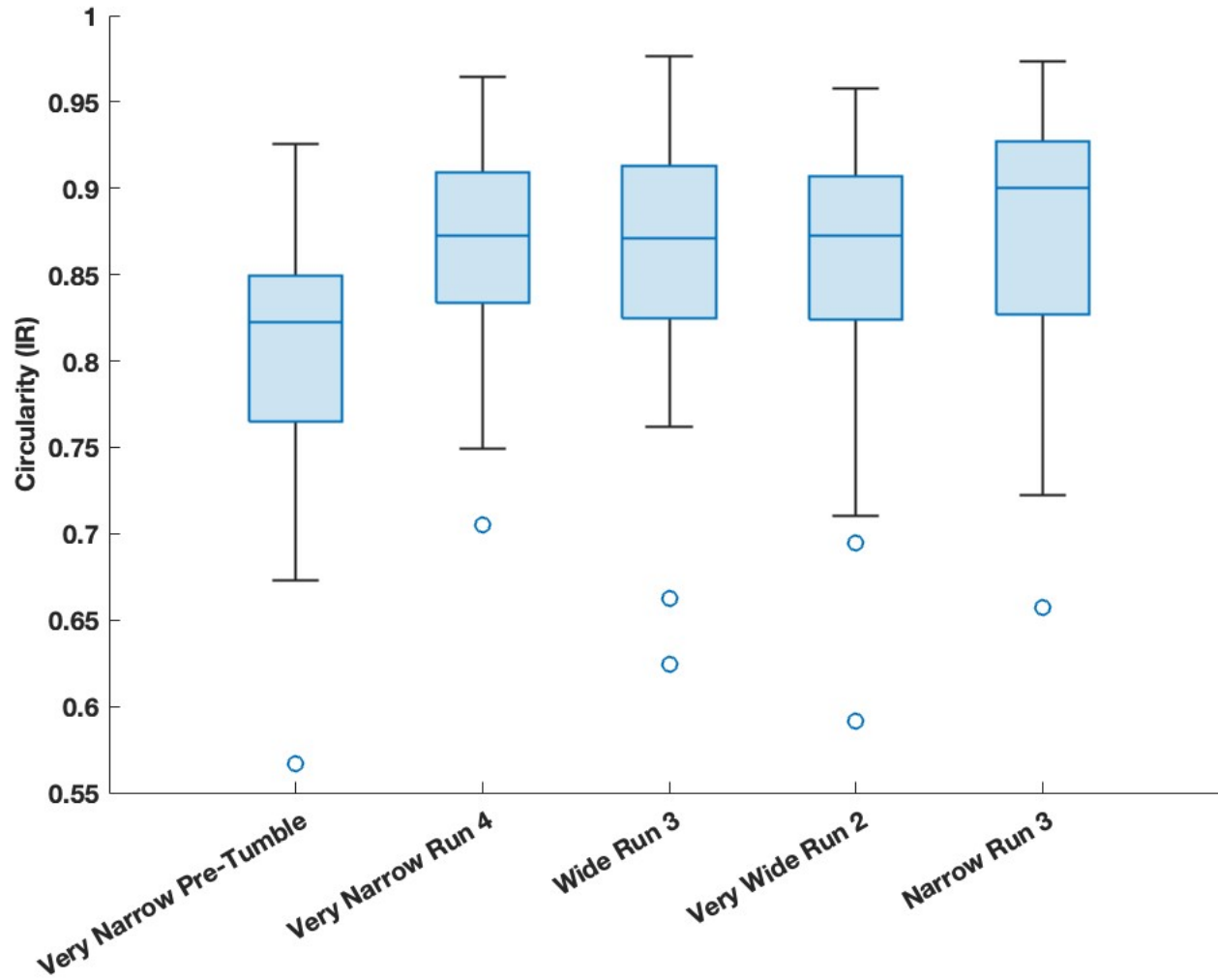


Figure 39. Boxplot of average circularity values from five random test images comparing Method 2 at 75 % resolution

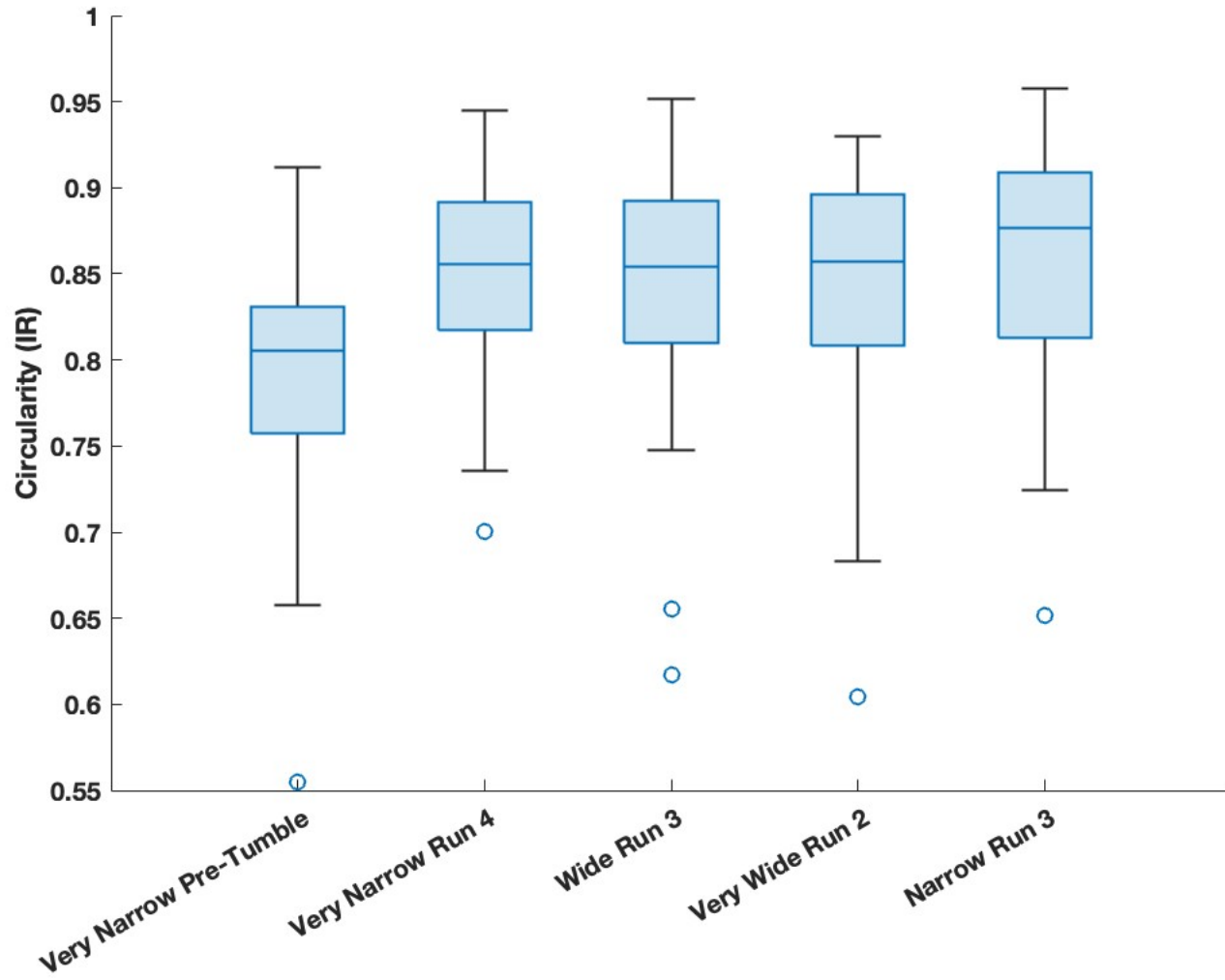


Figure 40. Boxplot of average circularity values from all four grain size distributions in the unsteady stat experiment using Method 2 at 100% resolution

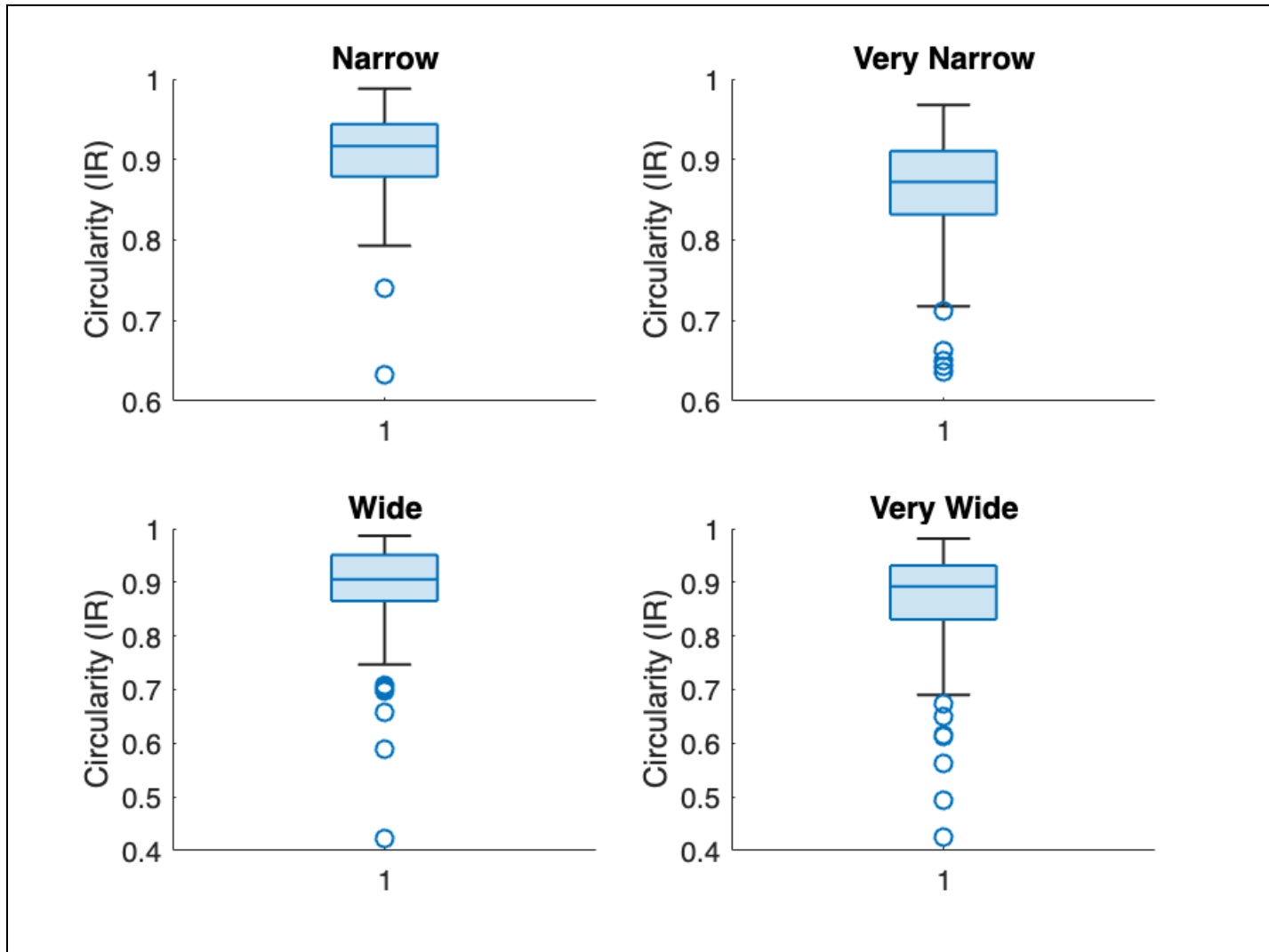
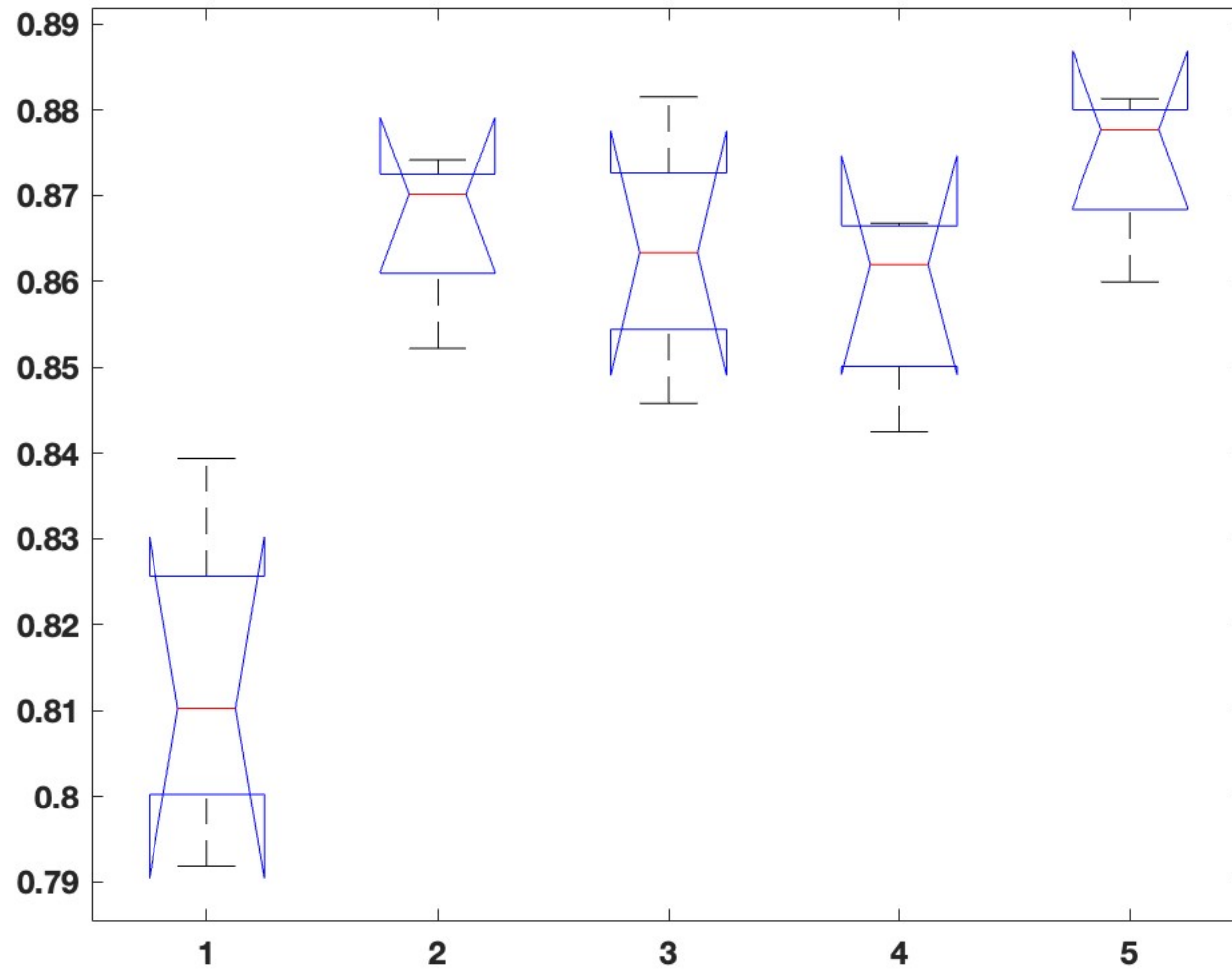
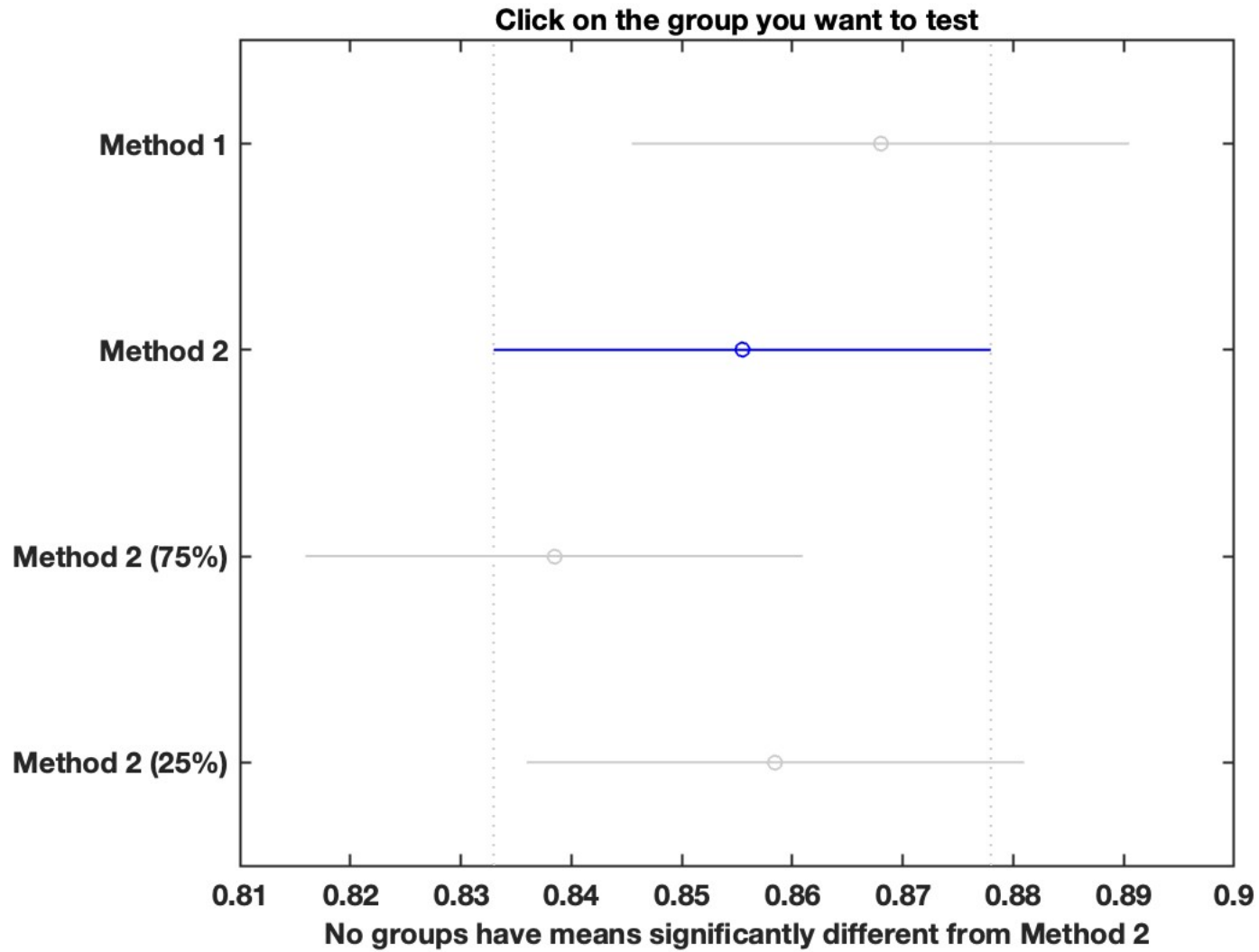


Figure 41. ANOVA Test plot including P-value for statistical analysis of differences between photo processing methods



P-value for ANOVA: 9.8634e-05

Figure 42. Tukey HSD statistical analysis for significant differences in mean circularity across all methods tested



Auxiliary Figures

Figure 43. Unsteady state experiment very narrow GSD

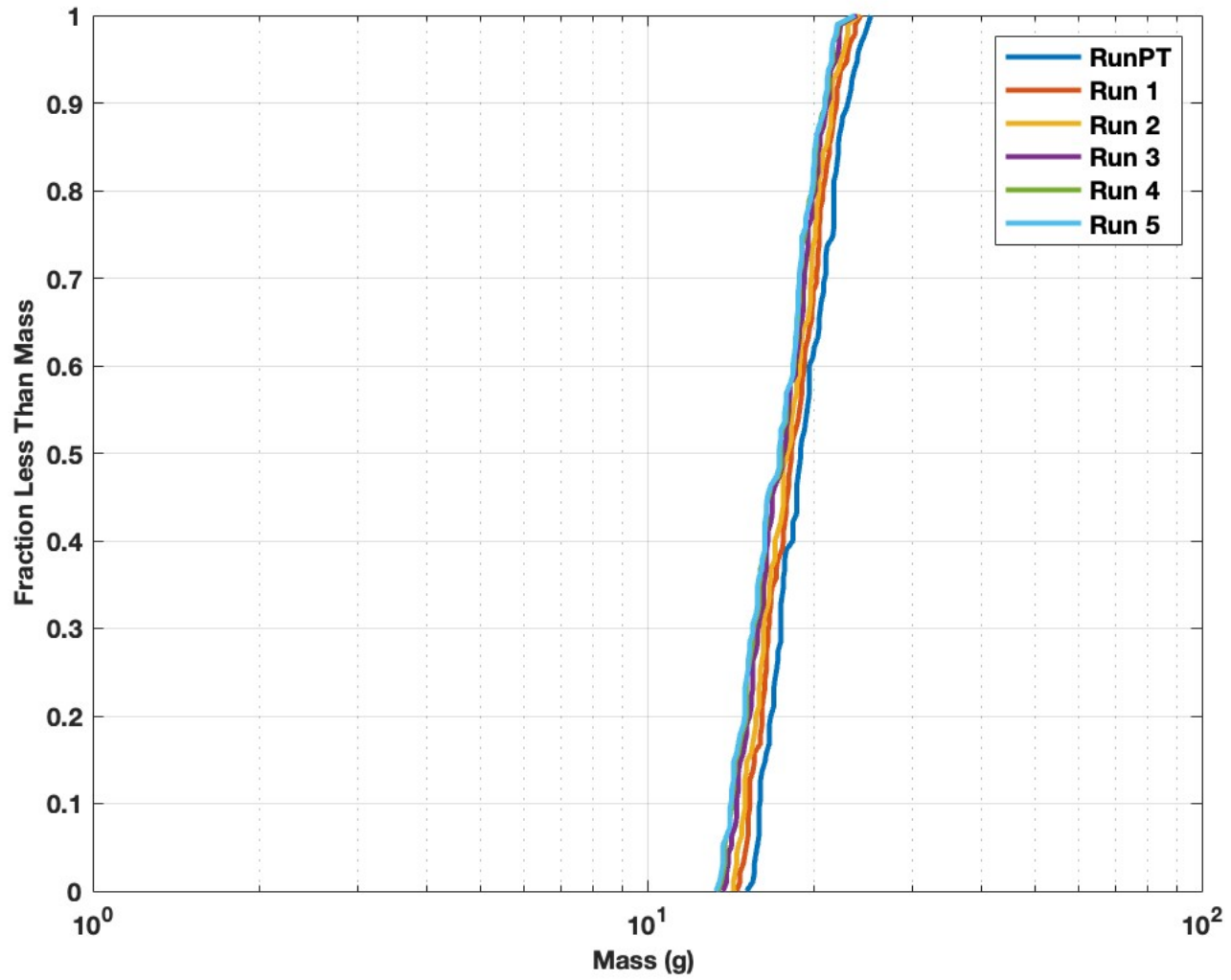


Figure 44. Unsteady state experiment narrow GSD

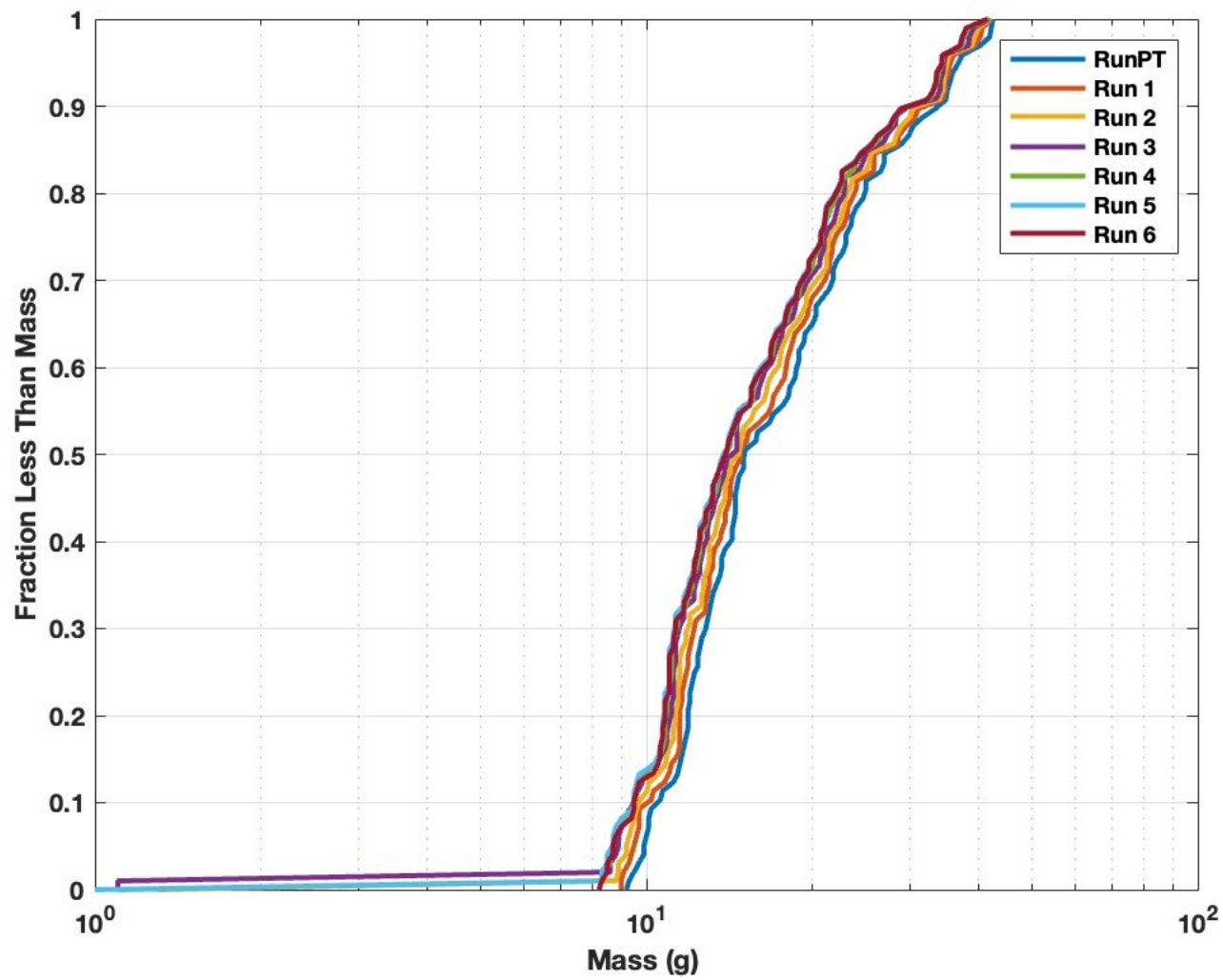


Figure 45. Unsteady state experiment wide GSD

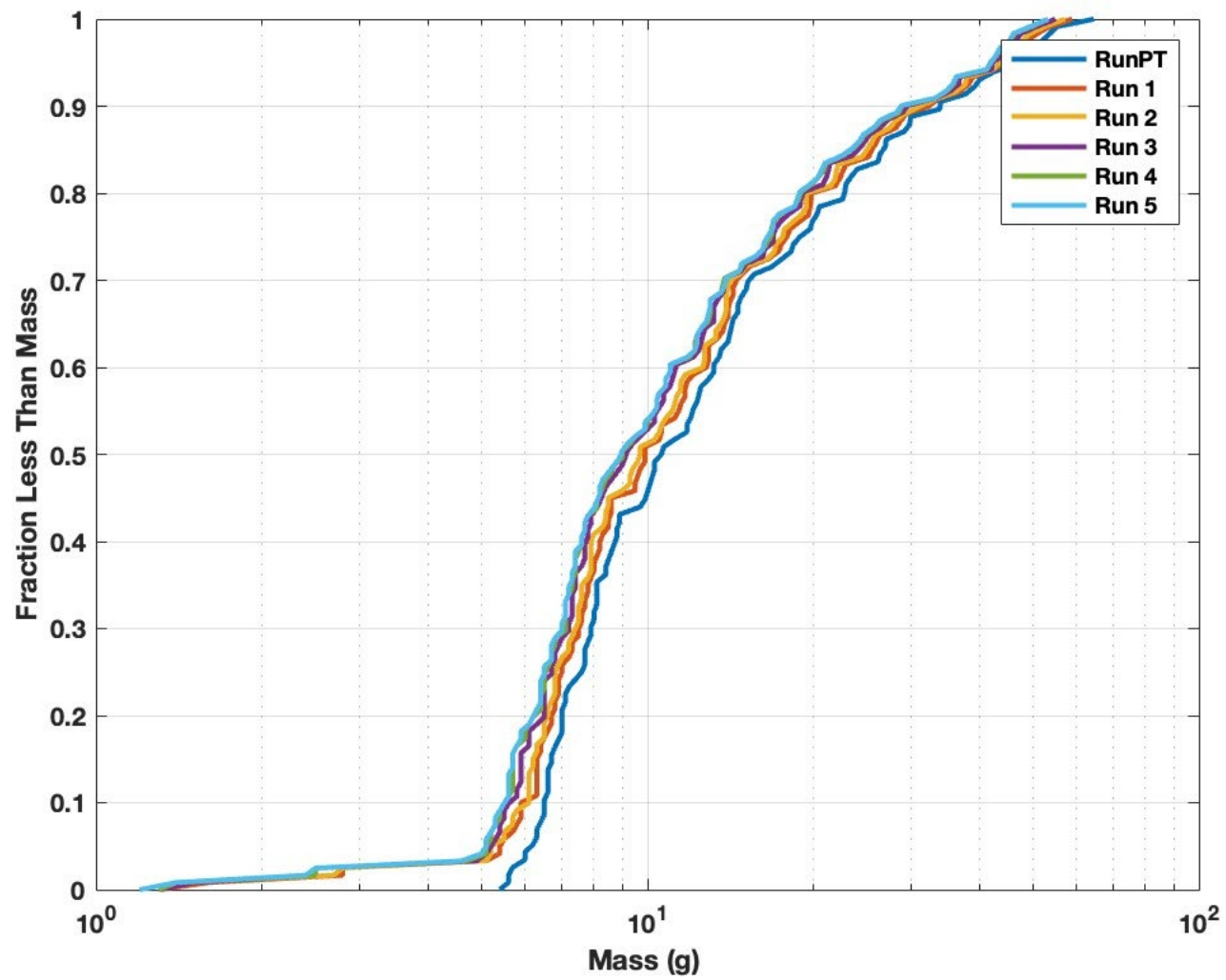


Figure 46. Unsteady state very wide GSD

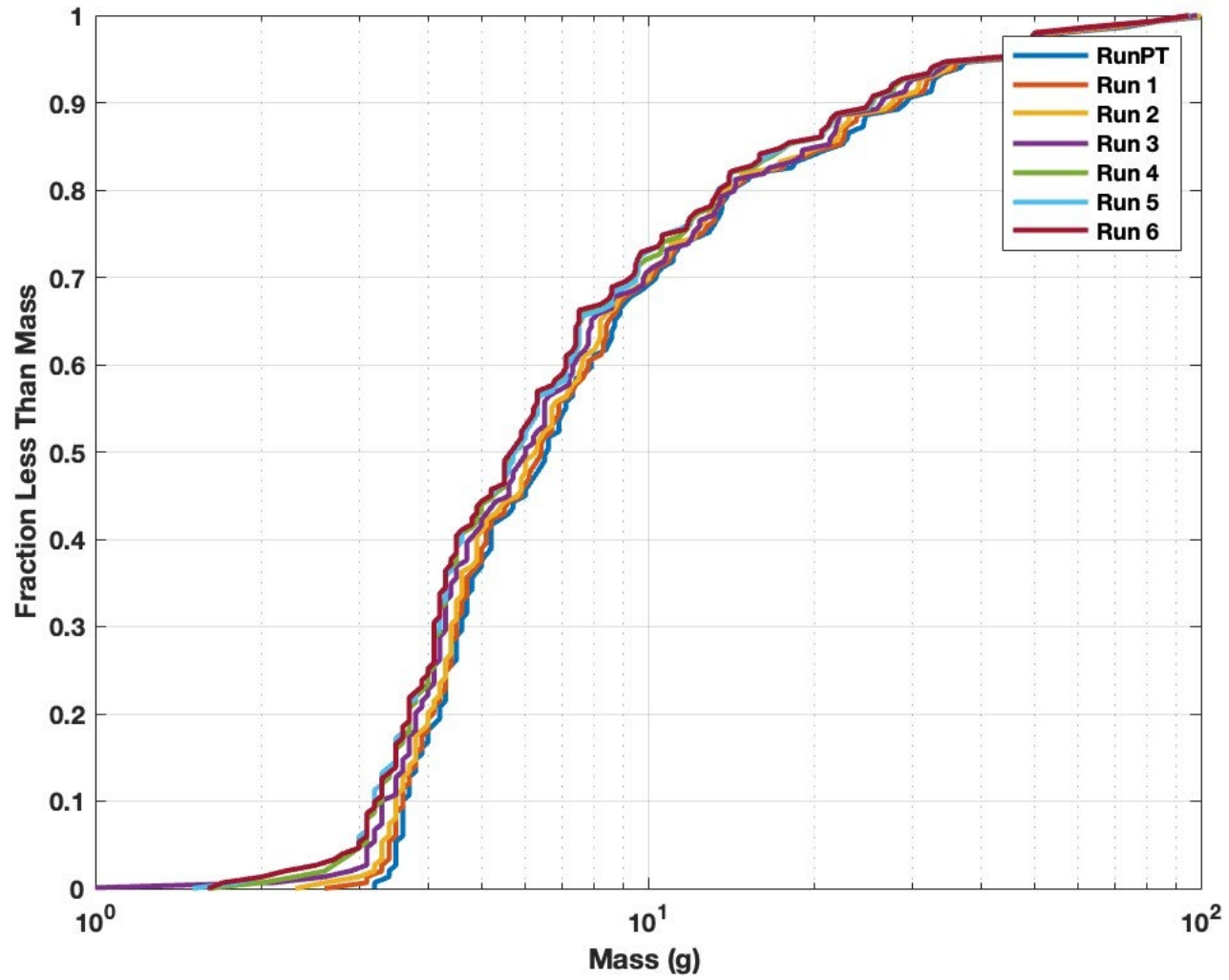
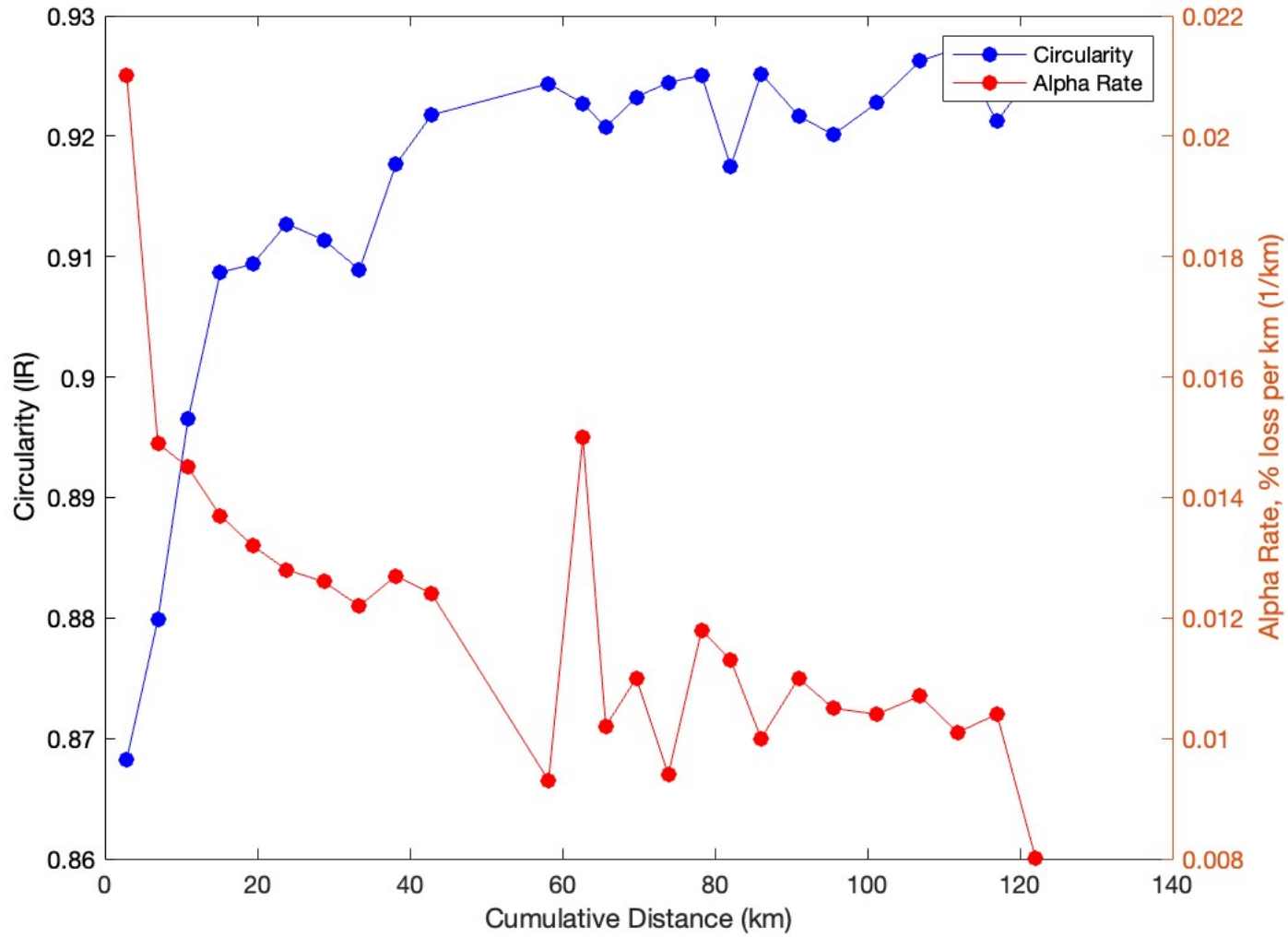


Figure 47. Steady state experiment inverse observed between circularity and alpha values with distance traveled



Tables

Table 1. Spread design of unsteady state experiments

Name	Average Mass (g)	Total Mass	Mass Range (g)	# of Clasts per Bin
Very Narrow	20.3	1850(g)	15.2 – 25.4 (g)	101
Narrow	12.0	1850 (g)	9.0 - 42.8 (g)	98
Wide	7.1	1850 (g)	5.4 – 72.0 (g)	116
Very Wide	4.2	1850 (g)	3.2-121.1 (g)	150

Table 2. Unsteady State laboratory runs conducted

Name	Range of Masses in Size Class (g)	# of Clasts per Bin	Starting Mass (g)	Ending Mass (g)	# of Runs to Reach 10% Mass Lost	# of Buckets of Silt	# of Photos and Names of Photo Files
Narrow	9.0 - 42.8 (g)	98	1850 (g)	1668.3	6	6	P1-A1-N (PT-R6)
Very Narrow	15.2 – 25.4 (g)	96	1850 (g)	1666.1	5	5	P1-A1-VN (PT-R5)
Wide	5.4 – 72.0 (g)	117	1850 (g)	1668.2	5	5	P1-A1-W (PT-R5)
Very Wide	3.2-121.1 (g)	150	1850 (g)	1659.6	6	6	P1-A1-VW (PT-R6)

Table 3. Unsteady state experiment narrow GSD data

Narrow :	Starting Mass (g)	Ending Mass (g)	Duration of Run (min)	% mass lost overall	Mass lost per run (g)	Alpha Rate (1/km)	Fragments Found	Mass of Fragments
Run 1	1850	1789.2	154	3.29	60.8	0.0302	15	1.2
Run 2	1850	1756.8	105	5.04	32.4	0.0244	37	2.2
Run 3	1850	1716.8	130	7.03	36.8	0.0228	36	3.2
Run 4	1850	1678.9	140	9.00	36.5	0.0214	34	4.6
Run 5	1850	1664.6	50	9.75	13.8	0.0232	37	5.1
Run 6	1850	1662.2	11	9.82	1.4	0.0108	40	6.1

Table 4. Unsteady state experiment very narrow GSD data

Very Narrow :	Starting Mass (g)	Ending Mass (g)	Duration of Run (min)	% mass lost overall	Mass lost per run (g)	Alpha Rate (1/km)	Fragments Found	Mass of Fragments
Run 1	1850	1775.9	250	4.01	74.1	0.0227	2	0.3
Run 2	1850	1741.6	156	5.86	32.3	0.0175	9	1.3
Run 3	1850	1679.6	220	8.24	44.0	0.0162	9	1.2
Run 4	1850	1671.8	135	9.63	25.8	0.0159	7	1
Run 5	1850	1666.1	30	9.94	5.7	0.0161	8	1

Table 5. Unsteady state experiment wide GSD data

Wide :	Starting Mass (g)	Ending Mass (g)	Duration of Run (min)	% mass lost overall	Mass lost per run (g)	Alpha Rate (1/km)	Fragments Found	Mass of Fragments
Run 1	1850	1793.3	140	3.06	56.7	0.0310	3	0.3
Run 2	1850	1757.1	130	5.02	36.2	0.0220	9	0.9
Run 3	1850	1706.6	219	7.75	50.5	0.0186	7	0.8
Run 4	1850	1674.1	140	9.51	32.5	0.0192	13	2.4
Run 5	1850	1665.7	30	9.83	5.9	0.0166	17	2.5

Table 6. Steady state experiment very wide GSD data

Very Wide:	Starting Mass (g)	Ending Mass (g)	Duration of Run (min)	% mass lost overall	Mass lost per run (g)	Alpha Rate	Fragments Found	Mass of Fragments
Run 1	1850	1811.6	107	2.08	38.4	0.0274	21	3.1
Run 2	1850	1774.9	129	4.06	36.7	0.0222	27	4.6
Run 3	1850	1728.9	207	6.54	46.0	0.0177	32	4.3
Run 4	1850	1670.8	207	9.69	58.2	0.0230	34	4.5
Run 5	1850	1670.0	14	9.73	0.8	0.0048	26	4.4
Run 6	1850	1659.6	35	10.29	10.4	0.0252	31	4.3

Table 7. Circularity values for all four photo processing methods tested

<u>Photo processing Method Used:</u>	Test 1: Very Narrow Pre-Tumble	Test 2: Very Narrow Run 4	Test 3: Wide Run 3	Test 4: Very Wide Run 2	Test 5: Narrow Run 3
<u>Method 1:</u> Mean Circularity using Image J Only (IR)	0.8394	0.8742	0.8815	0.8661	0.8787
<u>Method 2:</u> Mean Circularity Using PS and IJ (IR)	0.8087	0.8706	0.8636	0.8577	0.8767
<u>Method 2 @ 75% Resolution:</u> Mean Circularity (Using PS Bicubic Sharper Resample) 75% of original (ShapePars*) (IR)	0.7918	0.8522	0.8458	0.8425	0.8599
<u>Method 2 @ 25% Resolution:</u> Mean Circularity Using PS @ Lower Res (Using PS Bicubic Sharper Resample) 25% of original (ShapePars*) (IR)	0.8118	0.8696	0.863	0.8667	0.8813
<u>Separate Perimeter Test 1:</u> Mean Px/Perimeter: Filled in blob @ baseline resolution	687.776	625.3515	670.2698	703.5999	366.2994
<u>Separate Perimeter Test 2:</u> Mean Px/Perimeter: Contour @ baseline resolution. (ShapePars*)	695.1283	633.0316	677.8508	708.1371	380.8973

Table 8. Steady state experiment initial grain size distribution

<i>Mass Range: (g)</i>	<i>Mass (g)</i>	<i>Average Mass (g)</i>	<i>Number of rocks within range</i>
<i>9.0-15.1</i>	<i>909.8</i>	<i>12.3</i>	<i>76</i>
<i>15.2-25.4</i>	<i>605.6</i>	<i>19.1</i>	<i>30</i>
<i>25.5-42.8</i>	<i>334.6</i>	<i>28.5</i>	<i>11</i>

Table 9. Steady State Experiment summary data table

Steady State	Average Mass	Mass Range (g)	Duration of Run (min)	Alpha Rate (1/km)	Average Circularity	Average Diameter	Fragments Found	Mass of Fragments
Pre-Tumble	13.1	9.1 - 41.7	0	0	0.8126	25.4	0	0
Run 1	12.3	8.3 - 37.1	408	0.0210	0.8683	23.61	6	1.1
Run 2	12.15	7.6 - 36.8	575	0.0149	0.8799	22.64	17	2.6
Run 3	11.75	6.9 - 34.5	562	0.0145	0.8965	22.15	13	2.5
Run 4	11	2.4 - 32.2	597	0.0137	0.9087	21.89	11	3.5
Run 5	10.8	1.1 - 30.4	600	0.0132	0.9094	21.47	18	3.1
Run 6	10.75	1.6 - 28.8	630	0.0128	0.9127	21.14	13	3.6
Run 7	10.1	1.4 - 28.3	690	0.0126	0.9114	20.75	14	4
Run 8	9.8	1.1-28.0	660	0.0122	0.9089	20.54	13	4.1
Run 9	9.5	1.0 - 24.2	680	0.0127	0.9177	20.12	21	5.7
Run 10	9	1.3- 23.4	660	0.0124	0.9218	19.81	17	5.7

Table 10. Steady State Experiment Summary data continued

Steady State	Average Mass	Mass Range	Duration of Run (min)	Alpha Rate (1/km)	Average Circularity	Average Diameter	Fragments Found	Mass of Fragments
Run 11	7.8	1.3-39.8	2171	0.0093	0.9244	18.75	27	8
Run 12	7.8	1.3- 40.9	636	0.0150	0.9227	18.75	32	8.2
Run 13	7.8	1.2 - 40.1	424	0.0102	0.9207	18.9	28	7.7
Run 14	7.55	1.1 - 39.0	565	0.0110	0.9232	18.58	26	7.8
Run 15	7.45	1.2 - 38.1	597	0.0094	0.9245	18.62	29	8.3
Run 16	7.2	1.0 - 37.3	617	0.0118	0.9250	18.25	28	7.9
Run 17	7.0	1.0- 36.6	540	0.0113	0.9175	18.05	31	9.1
Run 18	6.8	1.0 - 35.9	563	0.0100	0.9252	17.92	25	9.4
Run 19	6.6	1.0 - 35.1	697	0.0110	0.9217	17.53	41	13.1
Run 20	6.4	1.1 - 34.5	640	0.0105	0.9201	17.22	49	14.2
Run 21	6.0	1.0 - 33.7	810	0.0104	0.9227	16.95	50	13.4
Run 22	5.7	1.1 - 32.8	800	0.0107	0.9262	16.81	55	13.6

Run 23	5.55	1.0 - 32.2	700	0.0101	0.9273	16.68	66	14.8
Run 24	5.3	1.0 - 31.70	730	0.0104	0.9212	16.58	39	14.7
Run 25	5.3	1.0 - 37.23	720	0.008	0.9255	16.78	70	17.2